

**Towards CNO measurement with Borexino: ^{210}Bi
homogeneity in the liquid scintillator**

VON
SALE-ITI KROON

MASTER ARBEIT IN PHYSIK
vorgelegt der
FAKULTÄT FÜR MATHEMATIK, INFORMATIK UND
NATURWISSENSCHAFTEN
der
RWTH AACHEN

im November 2019

angefertigt im
PHYSIKALISCHEN INSTITUT III. B

Erstgutachter und Betreuer
PROF. DR. LIVIA LUDHOVA
Physikalischen Institut III. B
RWTH Aachen

Zweitgutachter
PROF. DR. ACHIM STAHL
Physikalischen Institut III. B
RWTH Aachen

Ich versichere, dass ich die Arbeit selbstständig verfasst und keine anderen als die angegebenen Quellen und Hilfsmittel benutzt sowie Zitate kenntlich gemacht habe.

Aachen, den 29.11 2019

Abstract

Borexino is a liquid scintillator detector located in the Laboratori Nazionali del Gran Sasso, Italy whose main goal is the measurement of low-energy solar neutrinos. The first complete measurement of all the components of the pp-chain was performed with Borexino detector. In contrast, neutrinos from the CNO fusion cycle, expected to contribute less than 1% to the total solar power, have not been observed yet.

The observation of CNO solar neutrinos even in an ultra-pure liquid scintillator detector is challenging because of the similar spectral shapes of the signal due to CNO neutrinos and the ^{210}Bi background. ^{210}Bi from the ^{238}U chain undergoes β -decay to ^{210}Po and ^{210}Po undergoes α -decay into stable ^{206}Pb . As a part of the ^{238}U decay chain, ideally, ^{210}Bi would be in secular equilibrium with its daughter, ^{210}Po . Unfortunately, due to convective motions inside the detector, ^{210}Po can be introduced into the fiducial volume from peripheral sources. To prevent this, in 2015 the detector has been thermally insulated from its surroundings. Moreover, a large effort is dedicated towards linking the “easy-to-determine” ^{210}Po α -decay activity to that of ^{210}Bi . This can be achieved using different α/β discrimination techniques. This study concentrates on testing and evaluation of several pulse-shape discriminators developed in Borexino analysis. Then the discriminators were studied on ^{214}Bi and ^{214}Po data and Monte Carlo (MC) events, to compare the MC ability to simulate these pulse-shape discriminators.

The agreement was found sufficient, to study the time and position dependence of the performance of these discriminators based on the MC data. This was important since radon events during the Water Extraction (WE) period were mostly out of the Fiducial Volume (FV) of the CNO analysis and not homogenous, also of dying PMTs, because discriminators are sensitive to the number of live channels.

To prove the ^{210}Bi homogeneity and stability in the liquid scintillator, the β rate was studied in different energy regions in the *pep* FV and top-bottom dependently with Phase-III data. We are including the Low energy region, where the α/β discrimination is applied. In conclusion the uncertainty on ^{210}Bi is smallest in the Low and Optimized energy regions being 1.506 cpd/100t and 1.497 cpd/100t, respectively, with small enough for ^{210}Bi to be sufficiently homogeneous for the requirements of the CNO measurement.

Contents

1	Introduction	1
2	Neutrinos	3
2.1	Solar neutrinos	3
2.1.1	The proton-proton chain	3
2.1.2	The CNO cycle	6
2.1.3	Standard solar model	7
2.2	Oscillation and mixing	8
2.2.1	Oscillation mechanism	8
3	Borexino detector	12
3.1	The detector design	12
3.2	Calibration	14
3.3	Monte Carlo production	16
3.4	Neutrino detection	17
3.5	Backgrounds	18
3.5.1	External backgrounds	18
3.5.2	Internal backgrounds	18
3.5.3	Cosmogenic backgrounds	23
4	Borexino Solar neutrino analysis	24
4.1	Proton-proton cycle	24
4.2	Towards CNO measurement	27
5	Performance of α/β discriminators	31
5.1	Types of discriminators	31
5.1.1	Gatti parameter	31
5.1.2	Multi-layer perceptron	32
5.1.3	Fully connected network	33
5.2	Threshold optimization	34
5.2.1	Figure of merit calculations	36
5.2.2	Optimized thresholds	40
5.3	^{214}Bi and ^{214}Po data and MC	41
5.3.1	Efficiency and leakage	41
5.3.2	Radial dependency	44
5.4	^{210}Bi and ^{210}Po MC	49
5.4.1	Total efficiency and leakage	49
5.4.2	Time dependency	51
5.4.3	Radial dependency	53
6	^{210}Bi homogeneity and stability	57
6.1	Energy interval definitions	57
6.2	In fiducial volume	59
6.2.1	α events in time	59
6.2.2	β rate in different energy regions	60
6.3	Top-bottom dependency	68
6.3.1	The time dependency of each slice	69

6.3.2	Slice dependency of every year	73
7	Conclusions and outlook	75
	Appendices	77

1 Introduction

Neutrino (ν) is a neutral fermion (an elementary particle) with a very low mass, that interacts weakly. This means, neutrinos usually pass through matter unimpeded and undetected, thus maintaining their directionality and being perfect messenger particles. These properties make neutrinos ideal to study nuclear fusion in the Sun, radiogenic heat production in the Earth, Supernova explosions.

The neutrino flux at Earth is $\sim 10^{10} \text{ cm}^{-2}\text{s}^{-1}$. There are two processes responsible for the stellar energy production known as the proton-proton (pp) fusion chain and the carbon-nitrogen-oxygen (CNO) cycle. The contribution of these processes depends on the mass, temperature, and the age of the star. In case of the Sun, the largest part ($\sim 99\%$) of the energy is produced by the pp-chain, and the CNO cycle gives only a small contribution.

All types of neutrinos produced by the pp-chain (except very rare *hep* neutrinos) have been detected by solar neutrino experiments, but neutrinos from CNO-cycle are still undetected. Due to their very low flux and to their relatively low energy, the detection of CNO neutrino is in fact extremely challenging. Detecting CNO neutrinos would give the last missing information of the energy generation in the Sun, also this would be the first direct evidence of the nuclear process that is believed to fuel massive stars.

The Borexino detector, designed to measure solar neutrinos, is taking data at the Laboratori Nazionali del Gran Sasso (Italy) since May 2007. The key features of Borexino are its graded shielding design and its extreme radiopurity. During the so-called Phase-I (May 2007- May 2010) Borexino has succeeded in measuring the ${}^7\text{Be}$ neutrino fluxes with high precision, together with performing the first observation of *pep* and ${}^8\text{B}$ ν s and with a low threshold to give the best limit of CNO ν . After two years (2010-2011) of purification campaigns, Borexino Phase-II started in the end of 2011 and lasted until May 2016. The reduced background at low energies led to the first direct observation of all solar neutrinos from the pp reaction, the keystone process for energy production in the Sun. After thermal stabilization and a new trigger to the detector the so called Phase-III started in May 2016 and is ongoing, the next step and main goal of this phase is the first measurement of CNO ν .

A complication arises to measure the CNO ν in the Borexino detector. CNO neutrinos have a very similar spectral shape to *pep* neutrinos and to the radioactive ${}^{210}\text{Bi}$ decay. Hence, it is highly important to constrain the ${}^{210}\text{Bi}$ value in the liquid scintillator and the main goal of this thesis is to prove the homogeneity and stability of ${}^{210}\text{Bi}$ decay rate in the Borexino detector. To prove the ${}^{210}\text{Bi}$ homogeneity in the whole fiducial volume is important, because we are finding the ${}^{210}\text{Po}$ minimum rate only in a smaller volume, from which we are getting the ${}^{210}\text{Bi}$ rate.

The layout of the thesis is as follows:

- Chapter 2 presents a review of solar neutrinos, focusing in particular on their production mechanism and the oscillation of neutrinos in vacuum and in matter.
- Chapter 3 summarizes the design of Borexino detector and neutrino detection principle, together with the main backgrounds. The timeline with experiment physical goals and main results are reported.
- Chapter 4 provides a description of solar neutrino analysis done by the Borexino collaboration with the next steps towards measuring the CNO neutrinos.

- Chapter 5 reports my studies on different α/β discriminators, precisely finding their most optimized way of application in distinguishing β events from α events. Then testing the performance of different discriminators on ^{214}Bi and ^{214}Po data and Monte Carlo and ^{210}Bi and ^{210}Po Monte Carlo events. To find time and position dependency of efficiency and leakage.
- Chapter 6 is focused on looking at the β rate in different energy regions in the fiducial volume to prove the ^{210}Bi homogeneity in the liquid scintillator. The β rate will be studied time dependently in the whole fiducial volume and in six equivalent slices.

2 Neutrinos

Neutrinos are special in the particle world. They are neutral with a very low mass and their interaction cross section with standard matter is small, because they only couple through the weak interaction force. Neutrinos penetrate the Universe and are very abundant, since they are produced in many processes, such as radioactive decays or nuclear reactions powering the stars, the latter will be discussed more precisely in the next sections.

In this chapter, the production of neutrinos from the fusion reactions powering the Sun is introduced. Also the oscillation mechanism and MSW effect are described briefly.

2.1 Solar neutrinos

Neutrinos are produced in the Sun in nuclear reactions which take place in its core. This means that the solar neutrinos carry information about the Sun's interior, they reach the Earth almost without interacting with the matter from the production to the detection point. The only delay is due to the time of flight and it is approximately 8 minutes. For example photons reach the Earth approximately in 10^5 years after they are produced in the Sun's core. Studying the Sun through neutrinos gives us information which is not accessible in the photon channel.

The energy in Sun and other stars is produced through the fusion of four protons and two electrons into a ${}^4\text{He}$ nucleus plus two electron neutrinos [3]:



where the energy release (which is usually called the Q-value) is calculated by:

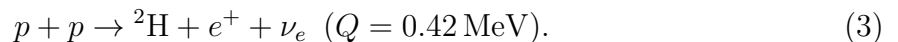
$$Q = 4m_p + 2m_e - m_{{}^4\text{He}} = B(4, 2) + 2m_e - 2(m_n - m_p) = 26.731 \text{ MeV}, \quad (2)$$

where the mass of the proton - $m_p = 938.272 \text{ MeV}$ [1], mass of the electron - $m_e = 0.511 \text{ MeV}$ [1], mass of the neutron - $m_n = 939.565 \text{ MeV}$ [1], and $B(4,2)$ is the binding energy of ${}^4\text{He} = 28.296 \text{ MeV}$ [3].

This happens in a series of reactions called pp-chain in $\sim 99\%$ of the cases in the Sun and other stars equivalent to the Sun and in the CNO cycle, where the remaining part of the energy ($\sim 1\%$) is produced through a subdominant set of reactions. The ratio between pp-chain and CNO cycle contribution depends on the star's mass. The only direct mean of investigation of the reactions happening in the Sun's core are neutrinos. Neutrinos produced by the pp-chain reactions have been observed already, but neutrinos from the CNO cycle have not been detected yet. The CNO cycle is theorized to be the main energy production in massive stars [5].

2.1.1 The proton-proton chain

The first and main process ($\sim 99.6\%$ of the cases) [15], as shown in Figure 1, is the fusion of two protons into deuterium:



The emitted neutrino in this process (known as $pp \nu$), has a continuous spectrum with a maximum energy correspondent to the Q-value in equation 3. Because of the high density

of hydrogen, this is the most probable reaction inside the Sun, hence the associated neutrino flux is high. Another and not so frequent (only $\sim 0.4\%$ of the cases) is the reaction:



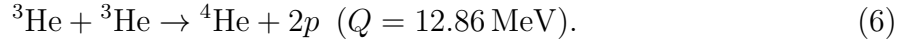
Neutrinos described with equation 4 are called *pep* ν . As soon as ${}^2\text{H}$ is produced, there is only one way to proceed, which consists in the absorption of a proton by the deuteron,



After this reaction, the pp-chain splits into three different terminations, called pp-I, pp-II, and pp-III branches, with different subsequent reactions.

The pp-I branch:

The main determination of this branch ($\sim 85\%$) consists in the reaction:



In this case there is no more neutrino emission.

Another reaction, that can happen ($\sim 15\%$ of the cases) is when ${}^3\text{He}$ undergoes the following reaction:



This reaction brings the two last branches of the pp-chain and the production of the other solar neutrinos.

The pp-II branch:

The ${}^7\text{Be}$ decays into ${}^7\text{Li}$:



In this reaction mono-energetic neutrino, called ${}^7\text{Be}$ neutrino, is produced. The neutrinos emitted in this reaction are monochromatic and in $\sim 90\%$ of the cases they have energy $\sim 862 \text{ keV}$. In the other $\sim 10\%$ of the cases, the lithium is produced in an excited state and thus the neutrino has an energy of $\sim 384 \text{ keV}$. The final reaction leads to the production of ${}^4\text{He}$:



The pp-III branch:

This branch has a low probability ($\sim 0.13\%$ of the cases). The ${}^7\text{Be}$ captures a proton before decaying, thus producing ${}^8\text{B}$:



${}^8\text{B}$ is unstable and decays fast via β -decay:



Neutrinos are produced and called ${}^8\text{B}$ neutrinos. They have a continuous spectrum with energies up to almost 16 MeV. This branch ends with ${}^8\text{B}$ decay:



With a low probability ($\sim 10^{-5}\%$), ${}^3\text{He}$ could react with a proton and create electron neutrino:



This is called *hep* reaction. The neutrinos created in equation 13 have a continuous spectrum which extends up to more than 18 MeV, but because of their very low production rate, they have not been observed yet.

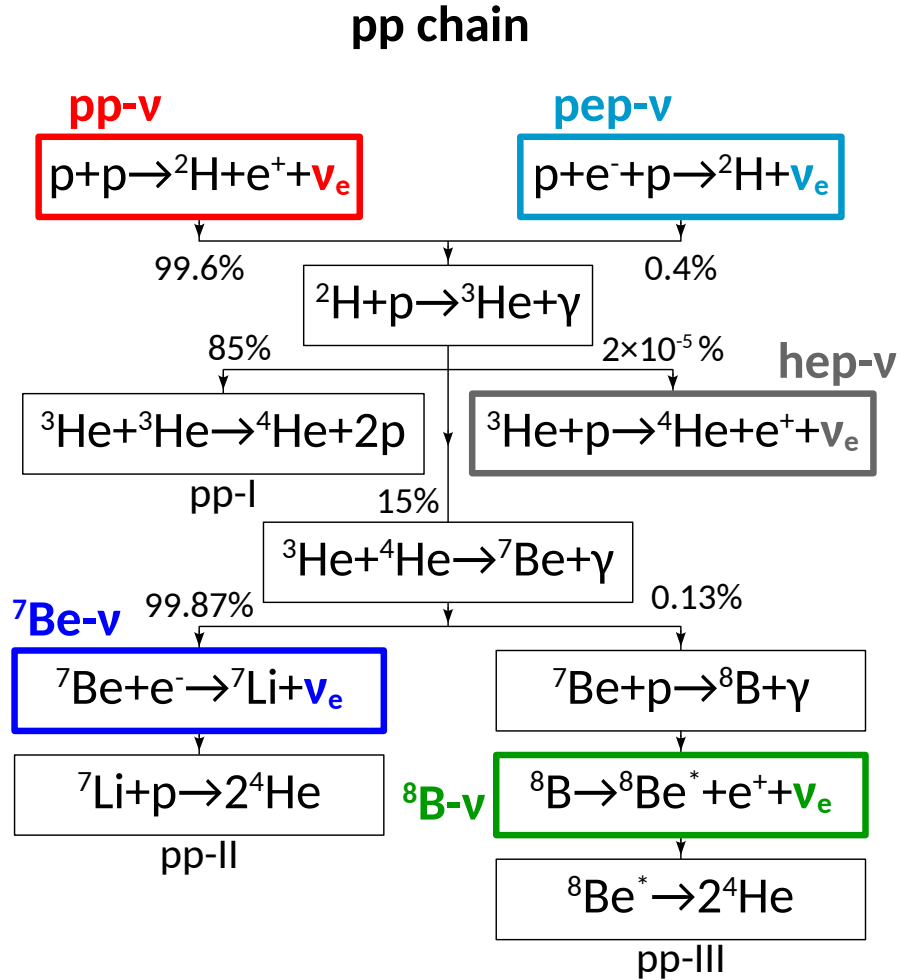


Figure 1: The pp-chain reactions dominating in stars the size of the Sun and smaller. The neutrinos which are produced by these reactions are shown in different colors (same as in Figure 3) with the corresponding names of the reactions.

2.1.2 The CNO cycle

As the pp-chain also the CNO cycle is a set of reactions which results in the fusion of four protons into helium atom, as shown in Figure 2. In the Sun and other equivalent stars, the CNO cycle is subdominant, but in heavier stars, where the temperature increases, the CNO cycle represents the largest way of energy production. The CNO cycle is actually an ensemble of different cycles, which include slightly different reactions but end up in the fusion of protons using carbon, nitrogen and oxygen isotopes as catalysts [5]. The detection of neutrinos from the CNO cycle would be very important for astrophysics.

The reactions happening in the CNO cycle are [15]:

$$^{12}\text{C} + p \rightarrow ^{13}\text{N} + \gamma \quad (Q = 1.95 \text{ MeV}), \quad (14)$$

$$^{13}\text{N} \rightarrow ^{13}\text{C} + e^+ + \nu_e \quad (Q = 1.2 \text{ MeV}), \quad (15)$$

$$^{13}\text{C} + p \rightarrow ^{14}\text{N} + \gamma \quad (Q = 7.54 \text{ MeV}), \quad (16)$$

$$^{14}\text{N} + p \rightarrow ^{15}\text{O} + \gamma \quad (Q = 7.35 \text{ MeV}), \quad (17)$$

$$^{15}\text{O} \rightarrow ^{15}\text{N} + e^+ + \nu_e \quad (Q = 1.73 \text{ MeV}), \quad (18)$$

$$^{15}\text{N} + p \rightarrow ^{12}\text{C} + ^4\text{He} \quad (Q = 4.96 \text{ MeV}). \quad (19)$$

The electron neutrinos produced in this cycle have continuous spectra before 2 MeV.

CNO cycle

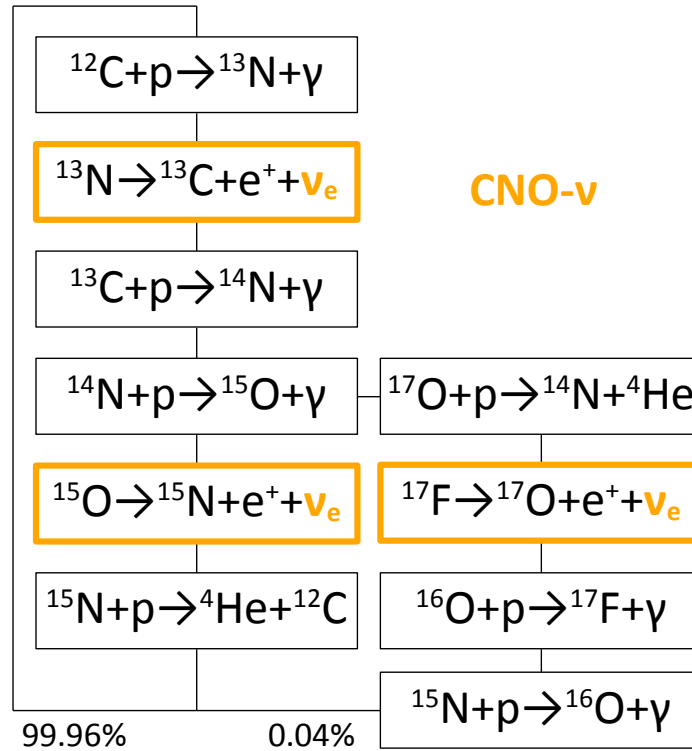


Figure 2: The CNO cycle reactions dominating in stars heavier than the Sun. The neutrinos which are produced are shown in yellow (same as in Figure 3).

2.1.3 Standard solar model

The *Standard Solar Model* (SSM) is a stellar model of stars with $M = M_{\odot}$ (mass of the Sun) about a quantitative description of the Sun and it is calibrated to match present-day, measured properties of the Sun. The calibration of the model is done by adjusting the mixing length parameter and the initial chemical composition in order to reproduce the observed solar luminosity, radius, and current surface composition. Then the SSM determines the mechanical and thermal properties of the Sun. The same reactions described in Chapters 2.1.1 and 2.1.2 also describe the energy production in the Sun that we can see as light (it is delayed by 10^5 years, due to the photon diffusion within the Sun) [6]. One can calculate the neutrino flux on Earth by measuring the solar's luminosity. According to the equation 1, two electron neutrinos are produced every time four protons fuse to produce a ${}^4\text{He}$ atom. The approximate total neutrino flux on Earth calculated with solar luminosity gives [7]:

$$\Phi \simeq \frac{L_{\odot}}{4\pi d^2 \cdot \frac{1}{2} \cdot 26.7 \text{ MeV}} \simeq 6 \cdot 10^{10} \nu \text{ cm}^{-2} \text{ s}^{-1}, \quad (20)$$

where L_{\odot} is the solar luminosity ($L_{\odot} = 4 \cdot 10^{33}$ erg/s), d is the distance between Sun and Earth ($d = 1.5 \cdot 10^{10}$ cm).

The SSM predicts that 99% of the solar energy is produced by pp-chain and the remaining part of the energy is produced by CNO cycle. As shown in Figure 3, most of the neutrinos ($\sim 90\%$) emitted by the Sun come from the pp reaction, as shown in equation 3. Most of the remaining $\sim 10\%$ of the neutrino flux is emitted in the electron capture reaction on ${}^7\text{Be}$, smaller contribution comes from proton-electron-proton fusion and from ${}^8\text{B}$ decays.

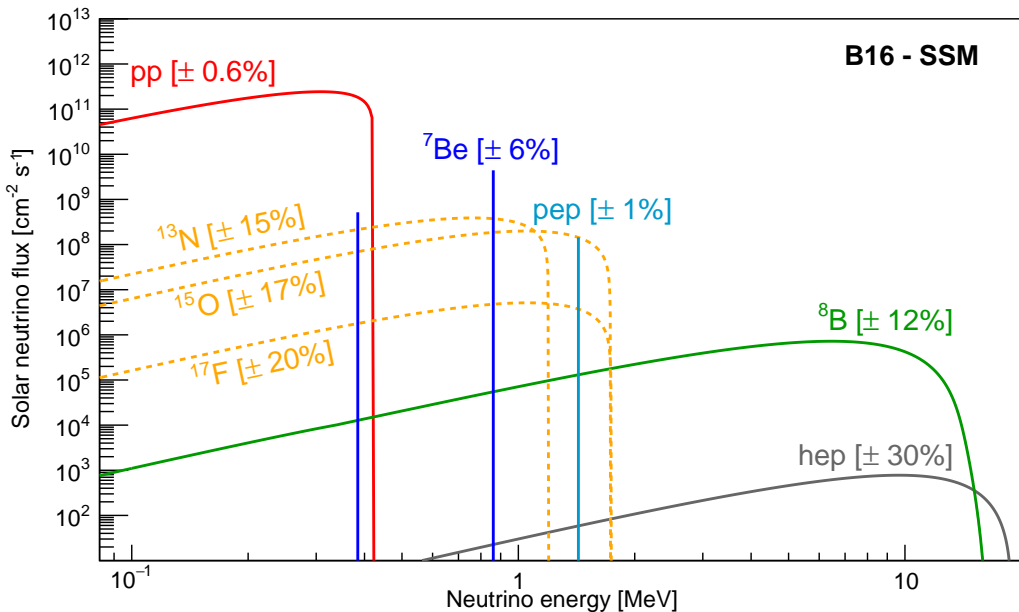


Figure 3: Predicted solar neutrino energy spectrum [9]. The flux is given in $\text{cm}^{-2} \text{ s}^{-1} \text{ MeV}^{-1}$ for continuous spectra and in $\text{cm}^{-2} \text{ s}^{-1}$ for mono-energetic ones. B16 is a new generation of *Standard Solar Models* (SSMs) [8].

For a long time, there was so called "solar neutrino problem", which means that all experiments observed fewer neutrinos than were expected by the predictions of the SSM

(predicted neutrino fluxes can be seen in Table 1), with high (HZ) and low (LZ) metallicity (solar metallicity means the abundance of elements heavier than He). This problem was solved when oscillation of solar neutrinos was experimentally proven by SNO experiment in 2001, by measuring neutrinos of all flavours via neutral current interactions.

Source	Flux - SSM predictions ($\text{cm}^{-2}\text{s}^{-1}$)	
	HZ	LZ
pp	$5.98(1.\pm 0.006)\cdot 10^{10}$	$6.03(1.\pm 0.005)\cdot 10^{10}$
${}^7\text{Be}$	$4.93(1.\pm 0.006)\cdot 10^9$	$4.50(1.\pm 0.006)\cdot 10^9$
pep (HZ)	$1.44(1.\pm 0.009)\cdot 10^8$	$1.46(1.\pm 0.009)\cdot 10^8$
pep (LZ)	$1.44(1.\pm 0.009)\cdot 10^8$	$1.46(1.\pm 0.009)\cdot 10^8$
${}^8\text{B}_{\text{HER-I}}$	$5.46(1.\pm 0.12)\cdot 10^6$	$4.50(1.\pm 0.12)\cdot 10^6$
${}^8\text{B}_{\text{HER-I}}$	$5.46(1.\pm 0.12)\cdot 10^6$	$4.50(1.\pm 0.12)\cdot 10^6$
${}^8\text{B}_{\text{HE}}$	$5.46(1.\pm 0.12)\cdot 10^6$	$4.50(1.\pm 0.12)\cdot 10^6$
CNO	$4.92(1.\pm 0.11)\cdot 10^8$	$3.52(1.\pm 0.10)\cdot 10^8$
hep	$7.98(1.\pm 0.30)\cdot 10^3$	$8.25(1.\pm 0.12)\cdot 10^3$

Table 1: Neutrino fluxes predicted by the SSM in the HZ or LZ hypotheses [8].

2.2 Oscillation and mixing

2.2.1 Oscillation mechanism

While neutrinos are created as flavour eigenstates, they propagate through space as mass eigenstates. A particular neutrino flavour eigenstate ν_α ($\alpha = e, \mu, \tau$) can be expressed as a linear superposition of mass eigenstates ν_i ($i = 1, 2, 3$), which propagate through space with slightly different frequencies due to their different masses, and between which different phases develop with distance traversed, corresponding to a change or oscillation in the neutrino flavour. Thus a neutrino, created with a unique flavour, after traversing some distance in space will become a superposition of different flavours, as evidenced by any subsequent interaction with matter. The probability of measuring a specific flavour for a neutrino varies periodically as it propagates through space [4].

The neutrino flavour eigenstates ν_α are a linear superposition of the mass eigenstates ν_i :

$$|\nu_\alpha\rangle = \sum_{i=1}^3 U_{\alpha i}^* |\nu_i\rangle, \quad (21)$$

where ν_i is the mass eigenstate and U is a 3×3 unitary matrix called neutrino mixing matrix or Pontecorvo-Maki-Nakagawa-Sakata (PMNS) matrix. The U can be parametrized as:

$$U = \begin{bmatrix} 1 & 0 & 0 \\ 0 & c_{23} & s_{23} \\ 0 & -s_{23} & c_{23} \end{bmatrix} \begin{bmatrix} c_{13} & 0 & s_{23}e^{-i\delta} \\ 0 & 1 & 0 \\ -s_{23}e^{i\delta} & 0 & c_{13} \end{bmatrix} \begin{bmatrix} c_{12} & s_{12} & 0 \\ -s_{12} & c_{12} & 0 \\ 0 & 0 & 1 \end{bmatrix} \begin{bmatrix} e^{i\rho} & 0 & 0 \\ 0 & e^{i\sigma} & 0 \\ 0 & 0 & 1 \end{bmatrix} \quad (22)$$

$$= \begin{bmatrix} c_{12}c_{13} & s_{12}s_{13} & s_{13}e^{-i\delta} \\ -s_{12}c_{23} - c_{12}s_{13}s_{23}e^{i\delta} & c_{12}c_{23} - s_{12}s_{13}s_{23}e^{i\delta} & c_{13}s_{23} \\ s_{12}s_{23} - c_{12}s_{13}s_{23}e^{i\delta} & c_{12}s_{23} - s_{12}s_{13}c_{23}e^{i\delta} & c_{13}c_{23} \end{bmatrix} \begin{bmatrix} e^{i\rho} & 0 & 0 \\ 0 & e^{i\sigma} & 0 \\ 0 & 0 & 1 \end{bmatrix},$$

where $c_{ij} = \cos \theta_{ij}$ and $s_{ij} = \sin \theta_{ij}$, $\theta_{12}, \theta_{23}, \theta_{13} \in [0, \frac{\pi}{2}]$ are the three mixing angles, $\delta = \delta_{CP} \in [0, 2\pi)$ is the Dirac CP-violating phase, ρ, σ are the Majorana CP-violating phases (if neutrinos are Majorana particles).

To express the main characteristics of the oscillation, two flavour approximation (ν_e and ν_μ) in terms of ν_1 and ν_2 is sufficient with just a single mixing angle θ and no CP violation:

$$\begin{pmatrix} \nu_e \\ \nu_\mu \end{pmatrix} = \begin{pmatrix} \cos \theta & \sin \theta \\ -\sin \theta & \cos \theta \end{pmatrix} \begin{pmatrix} \nu_1 \\ \nu_2 \end{pmatrix}, \quad (23)$$

where θ denotes some arbitrary mixing angle. The wave amplitudes are orthonormal states:

$$\nu_e = \nu_1 \cos \theta + \nu_2 \sin \theta, \quad (24)$$

$$\nu_\mu = -\nu_1 \sin \theta + \nu_2 \cos \theta. \quad (25)$$

If E indicates the energy of neutrino, the amplitudes of mass eigenstates as a function of time will be:

$$\nu_1(t) = \nu_1(0) \exp(-iE_1 t), \quad (26)$$

$$\nu_2(t) = \nu_2(0) \exp(-iE_2 t), \quad (27)$$

where the units of reduced Plank constant \hbar , and speed of light c are $\hbar = c = 1$, so the angular frequency $\omega = E$. The mass eigenstates will have a fixed momentum p , if the masses are $m_i \ll E_i$ ($i = 1, 2$),

$$E_i = p + \frac{m_i^2}{2p}. \quad (28)$$

Using equation 28 and writing the difference of the squares of the masses as $\delta m^2 = m_2^2 - m_1^2$, and assuming $m_2 > m_1$, the probability of finding one or other flavour after a time $t = \frac{L}{c}$, where L is the distance travelled, is

$$P(\nu_e \rightarrow \nu_e) = 1 - \sin^2 2\theta \cdot \sin^2 \left(1.27 \frac{\Delta m^2 L}{E} \right) \quad (29)$$

$$P(\nu_e \rightarrow \nu_\mu) = 1 - P(\nu_e \rightarrow \nu_e) \quad (30)$$

where the numerical coefficient is $\frac{1}{4\hbar c}$, when L is expressed in km, Δm^2 in $(\text{eV}/c^2)^2$, and E in GeV [4].

When neutrino penetrates dense matter, the interactions with the medium affect their oscillation mechanism [23]. This happens because ordinary matter has electrons but not muons or taus, hence when a ν_e beam goes through matter, it can undergo charged and neutral current interactions with electrons. ν_μ and ν_τ interact with electrons only via neutral current, so they have a lower cross-section than ν_e . Then it was discovered, that under particular conditions, the matter effect can lead to a resonant flavor transition, this effect is also known as Mikheyev-Smirnov-Wolfenstein (MSW) effect.

When neutrinos are travelling through a dense medium (Sun or Earth), their propagation can be significantly modified by the coherent forward scattering from particles they encounter along the way. As a result, the oscillation probability can be different than in vacuum. It is important to look at the evolution of ν_e in a medium with electrons, protons and neutrons, with corresponding N_e, N_p and N_n number densities.

The effective potential of *charged current* (CC) interaction is:

$$V_{CC} = \pm \sqrt{2} G_F N_e, \quad (31)$$

where G_F is the Fermi coupling constant and N_e is the electron number density [24]. Every flavour of neutrinos can interact with protons, neutrons, and electrons of the medium through *neutral current* (NC) interactions:

$$V_{NC} = \mp\sqrt{2}G_F N_e, \quad (32)$$

because $n_e = n_p$, so the contribution from electrons and protons cancel each other. Therefore $V_{\nu_e} = V_{CC} + V_{NC}$ and $V_{\nu_\mu} = V_{\nu_\tau} = V_{NC}$. Then the effective Hamiltonian, which governs the propagation of neutrinos in matter can be written as:

$$H_M = \left(\frac{\Delta m^2}{4E}\right) \begin{pmatrix} -\cos 2\theta & \sin 2\theta \\ \sin 2\theta & \cos 2\theta \end{pmatrix} + \begin{pmatrix} V_e & 0 \\ 0 & V_\mu \end{pmatrix} \quad (33)$$

$$= \left(\frac{\Delta m^2}{4E}\right) \begin{pmatrix} -\cos 2\theta & \sin 2\theta \\ \sin 2\theta & \cos 2\theta \end{pmatrix} + \begin{pmatrix} V_{CC} & 0 \\ 0 & 0 \end{pmatrix}. \quad (34)$$

This leads to the usual dependence of the oscillation probability:

$$P(\nu_e \rightarrow \nu_\mu) = \sin^2 2\theta_m \cdot \sin^2\left(\frac{\Delta m_m^2 L}{4E}\right). \quad (35)$$

With the effective mixing parameters in matter:

$$\Delta m_m^2 = \Delta m^2 \sqrt{\left(\frac{V_{CC}}{\Delta m^2} - \cos 2\theta\right)^2 + \sin^2 2\theta} \quad (36)$$

$$\tan 2\theta_m = \frac{\tan 2\theta}{1 - \frac{V_{CC}}{\Delta m^2 \cos 2\theta}}. \quad (37)$$

These parameters highlight important consequences of the MSW effect:

- For the possibility of oscillation happening in the matter, there has to be oscillation in vacuum (if $\tan 2\theta = 0$, then $\tan 2\theta_m = 0$),
- Oscillation cannot happen in a very dense matter via matter effects (if $V_{CC} \rightarrow \infty$, then $\tan 2\theta_m \rightarrow 0$),
- the mixing angle θ_m is maximal under some conditions, irrespectively of the value of θ , therefore even if the vacuum oscillation probability is very small. In particular, when the electron density matches the value:

$$\frac{V_{CC}}{\Delta m_m^2} = \cos 2\theta \rightarrow N_e = \frac{\Delta m_m^2 \cos 2\theta}{2\sqrt{2}G_F E}, \quad (38)$$

the effective mixing angle reaches the value $\frac{\pi}{4}$ and then it is possible to have a total flavor transition.

- the resonant condition occurs if $\Delta m_m^2 > 0$. This dependence can be used to determine the neutrino mass hierarchy. The fact that the MSW effect has been observed in solar neutrino experiments means that we do know that the sign of Δm_{12}^2 is positive.

In case of solar neutrinos, when electron neutrino is created in the core of the Sun with very high density. According to previous results it cannot oscillate there, so when propagating outwards from the core, towards the surface, it crosses a region of the Sun with electron number density that fulfills the resonance condition. In that region the probability to oscillate from ν_e to ν_{μ} is maximal. Once out of this region, the matter density is too small to support matter oscillation. Also, the MSW effect importance changes with the neutrino energy, as shown in Figure 4. In particular, the transition between the low energy regime (the MSW effect is negligible) and the high energy regime (the oscillation probability is determined by matter effects) lies in the region of about 2 MeV for the solar neutrinos. For high energy solar neutrinos the matter effects are important and, assuming a slowly varying solar density. For the low-energy solar neutrinos, on the other hand, the matter effect is negligible, and the formalism of oscillations in vacuum is valid [25].

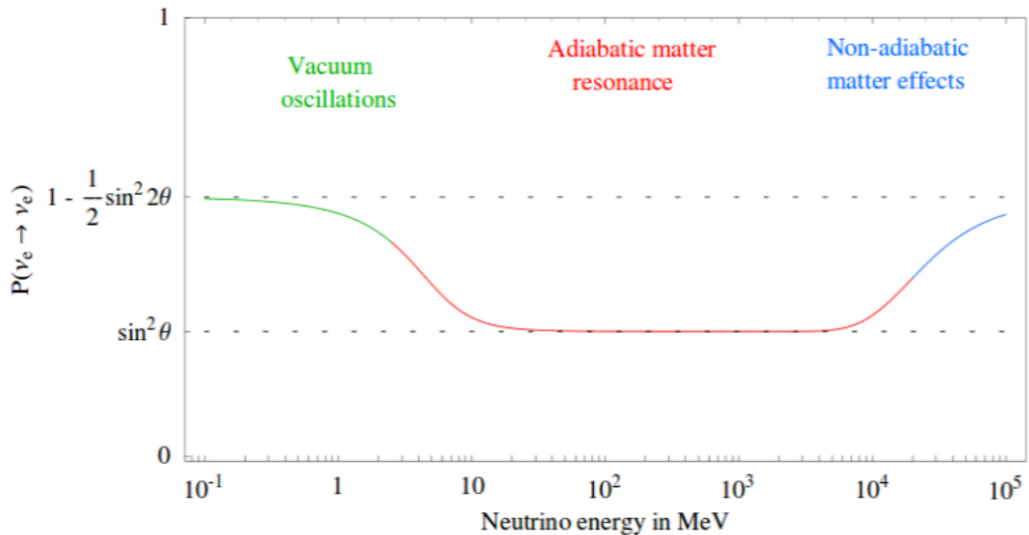


Figure 4: The survival probability of ν_e in matter as a function of energy [25]. For low neutrino energies, the matter effect is negligible; at intermediate energies, above the minimum resonant energy ~ 2 MeV, matter oscillation are dominant and the suppression can be seen; at higher energies, the MSW resonance is no longer adiabatic and the matter effect becomes negligible.

3 Borexino detector

In this chapter Borexino detector is described (see Section 3.1), specifically its design and calibration processes (see Section 3.2) are explained and the production of Monte Carlo (see Section 3.3). The detection of neutrinos (see Section 3.4) and the different backgrounds (see Section 3.5) in the detector are specified.

3.1 The detector design

The Gran Sasso National Laboratories are built under the Gran Sasso Mountain in Italy and Borexino is one of several experiments, which gets at least 1400 meters of shielding in any direction (or 3800 m.w.e) from cosmic ray particles due to the carbonate rocks.

Borexino is a liquid scintillator (LS) calorimetric detector with an onion-like arrangement, where volumes are located concentrically to one another. This strategy reduces the background levels in the innermost sections [2].

The layout of the detector is shown in Figure 5. The Inner Detector (ID) is inside of a Stainless Steel Sphere (SSS). The Outer Detector (OD), surrounding the ID, is a domed cylindrical steel tank filled with pure water, called as Water Tank (WT), the maximum height of WT is 17 meters, diameter is 18 meters, and it acts as a Cherenkov detector.

Inside the SSS, with radius 6.85 meters, two spherical nylon spheres divide the ID into two volumes, one as the active volume called Inner Vessel (IV) with radius 4.25 meters and other as the Outer Vessel (OV) with radius 6.85 meters. The spherical shell between the IV and SSS is known as the Buffer Volume (BV). The light produced in the ID and OD is collected by photomultiplier tubes (PMTs) placed on the walls of the SSS, shown in Figure 5 as Internal PMTs.

The IV contains around 280 tons of the liquid scintillator, which is composed of PC (pseudocumene, 1,2,4-trimethylbenzene $C_6H_3(CH_3)_3$) as a solvent and the fluor PPO (2,5-diphenyloxazole, $C_{15}H_{11}NO$) as a solute at a concentration of 1.5 g/l. The shift in wavelength improves the time response and matches better the photomultiplier quantum efficiency window. To the pseudocumene in the BV it is added 5 g/l of dimethylphthalate ($C_6H_4(COOCH_3)_2$), a light quencher. This means a particle moving through BV produces much smaller amount of scintillation light compared to a particle moving through IV, by this the external background from PMTs is being reduced significantly [10].

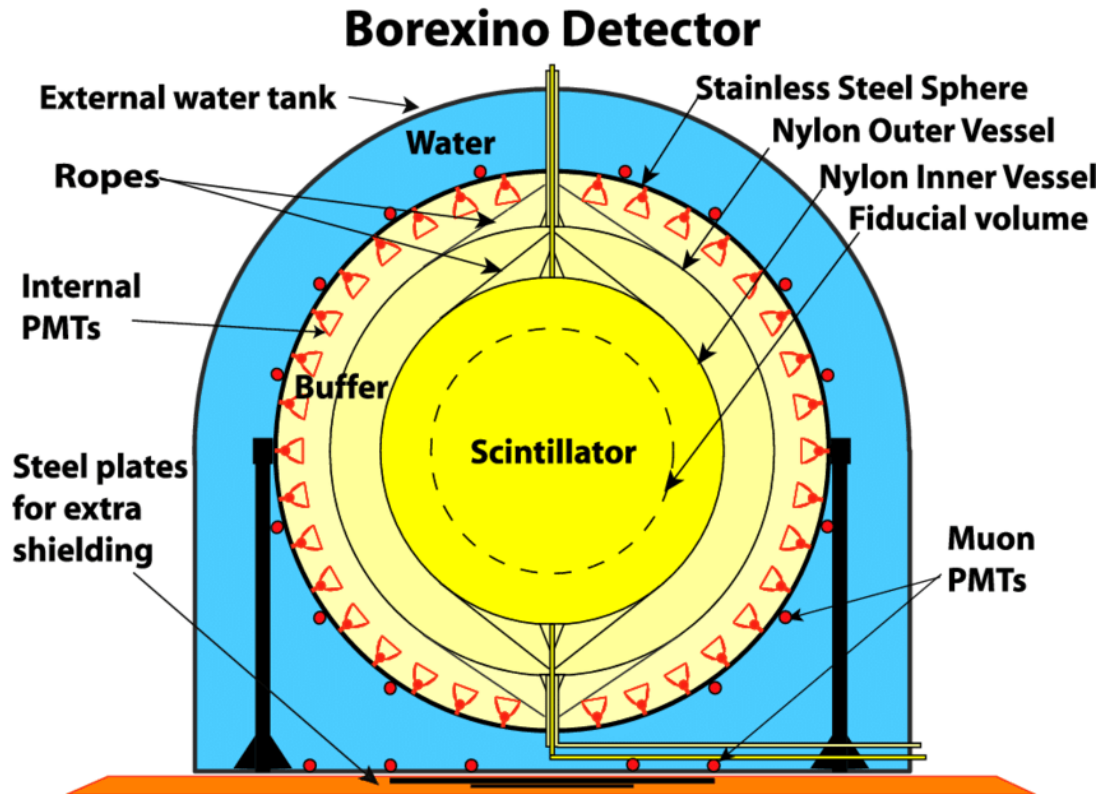


Figure 5: Schematic drawing of the internal structure of Borexino detector [10]. The innermost solid line is the Inner Vessel, containing the active scintillator volume. Together with its surrounding Buffer Volume, they constitute the Inner Detector, enclosed by the Stainless Steel Sphere. The sphere is surrounded by the Water Tank Outer Detector which acts as a muon veto.

Timeline of the Borexino experiment:

As shown in the Figure 6, there have been three phases in the Borexino experiment and between the first two phases there was a purification processes.

Until 2007 there were preparations to take measurements and in May 2007 Borexino started data taking and terminated its Phase-I in May 2010. The measurements during Phase-I allowed for the first observation and precise measurement of ${}^7\text{Be } \nu$ [16], the first observation of $pp \nu$ [17], ${}^8\text{B } \nu$ with low threshold [18] and to give the best limit of $\text{CNO } \nu$ [9].

Between May 2010 and the end of 2011, purification campaigns took place, leading to a further reduction of the radioactive contaminants, this purification period is called Water Extraction (WE) period.

Phase-II started at the end of 2011 and lasted until May 2016, during this time the $pp \nu$ s were measured [19] and frist complete study of all the components of the pp-chain were performed [9], for more information look into Chapter 4.1.

The period, from May 2016 until today, is called Phase-III, and in this duration the detector has been added thermal stabilisation and a new trigger and an attempt is ongoing to search for CNO neutrinos, for more information look into Chapter 4.2.

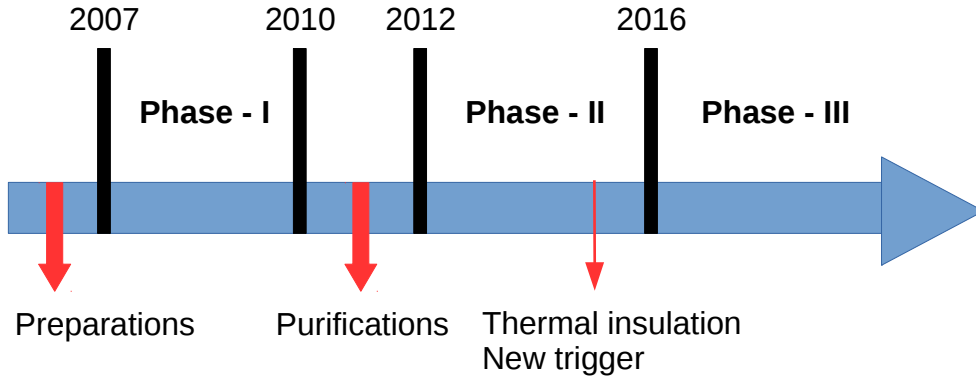


Figure 6: Timeline of Borexino experiment.

Energy reconstruction:

Several variables are defined to estimate the energy of the event. Information used to reconstruct energy estimators are the hits arriving at the PMTs and the charge collected by the PMTs in those hits. To estimate the energy based on hits, one could count the number of hits arriving at PMTs within the length of the reconstructed cluster. If we count all the hits, including multiple hits on single PMTs, we are getting the energy variable n_{hits} . If instead, we count only the number of PMTs hit, regardless of how many times each PMT was hit, we are computing the variable $npmts$. The second possible way of estimating the energy of an event is by summing up the charge recorded for every hit arriving within the cluster duration. We call that variable N_{pe} , or simply $charge$. The number of PMTs available for photon detection decreases with time. This implies that the previous estimators can return different results considering two events generated in different times but with the same energy, as the number of hits detected decreases with time. One way to account for this variation is to normalize event-by-event the energy estimators, by multiplying them by a factor equal to 2000 divided by the number of working PMTs. Such variables are said to be normalized. To take into account the total number of photo electrons collected in the PMTs after applying geometrical correction that accounts for the different number of PMTs in the northern and southern part of the detector. These variables are said to be geonormalized. The $npmts_dt1$ includes PMTs hit within 230 ns after the beginning of each cluster. [21]

3.2 Calibration

The internal calibration of Borexino detector consists of two sub-systems. One is the calibration source deployment system used to deploy radioactive sources into the desired location within the scintillator. Another sub-system is the source location system used to determine the source reference position with a precision better than 1 cm [12].

Source Insertion System

Because of the detector's design, the only access to the scintillator volume is through a 4" diameter pipe connecting the IV to a gate valve on top of the WT. The system itself is made up of a series of interconnecting hollow rods, assembled into an arm that can be bent up to 90° once inside the detector. All operations are performed through a glovebox installed in a Class 100 cleanroom atop the detector. An automated process-control system monitors gas (pure N₂) pressure and flow rates inside the connecting equipment [12].

In order to cover the energy region of interest for Borexino and to investigate the scintillator response to different ionizing particle types different types of sources were added, which can be seen in Table 2.

Main calibration points were obtained with a compound ¹⁴C-²²²Rn sources which provide α, β, γ radiation across a large energy region. The calibration results obtained thanks to α and β radiation were among the most important in the whole campaign, especially for position reconstruction studies, because the confinement of α and β events to within the vial gives a good handle on this behavior, provided the source is very well located thanks to the source location system hardware [11]. ¹⁴C and ²²²Rn were simultaneously present in the scintillator.

In order to use γ sources for energy calibrations in Borexino, the sources had to be mono-energetic and the scintillation light induced by associated α or β radiation had to be suppressed. This was achieved by depositing the radioisotope of interest in a non-scintillating medium within a source vial that absorbs the α and β particles.

In order to study ⁸B ν s, geo-neutrinos or place limits on solar and other unknown antineutrino fluxes, search for solar axions, it is important to energy calibration points up to 10 MeV. This was achieved by adding ~ 10 Bq ²⁴¹Am ⁹Be neutron source into the detector [12].

Source	Type	E (MeV)	Position	Motivations	Campaign
⁵⁷ Co	γ	0.122	in IV volume	E	IV
¹³⁹ Ce	γ	0.165	in IV volume	E	IV
²⁰³ Hg	γ	0.279	in IV volume	E	III
⁸⁵ Sr	γ	0.514	in z-axis + R=3 m	E + FV	III,IV
⁵⁴ Mn	γ	0.834	along z-axis	E	III
⁶⁵ Zn	γ	1.115	along z-axis	E	III
⁶⁰ Co	γ	1.173, 1.332	along z-axis	E	III
⁴⁰ K	γ	1.460	along z-axis	E	III
²²² Rn+ ¹⁴ C	β, γ	0-3.20	in IV volume	FV+uni	I-IV
	α	5.5, 6.0, 7.4	in IV volume	FV+uni	
²⁴¹ Am ⁹ Be	n	0-9	sphere R=4m	E + FV	II-IV

Table 2: Radioactive sources, which were used during the internal calibration campaigns in the Borexino detector. The radionuclides, emitted particle types and energies are shown in the first three columns. In the Position column we have, where the sources were deployed within the scintillator. In the fifth column we have the main purpose for each source, where E and uni stand for Energy scale and uniformity respectively. The last column indicates when each sources have been deployed: I (Oct 2008), II(Jan 2009), III(Jun 2009), IV(Jul 2009) [12].

Source Location System

A prior task in Borexino analyses is the definition of the FV, which is related to the determination of the event position. Therefore, one purpose of the calibration campaigns was to study the performance of the software algorithm used to estimate the position of data events by comparing the source locations determined using the reconstruction software with the true source locations. This method is limited by the uncertainty on the true position of the source. To achieve an uncertainty on the FV determination at the 1% level it requires a precision of ~ 1 cm on the source position determination [12].

3.3 Monte Carlo production

Particles depositing energy in the IV or in the buffer regions produce scintillation and Cherenkov photons, which propagate inside the detector and possibly reach the PMTs, yielding a detectable signal. The agreement between measured observables (energy estimators and PMT pulse times) and the physical quantities (deposited energy, position, type of particles generating the signal) depends on the knowledge and understanding of all the physical processes governing the particle energy loss in the various materials, the scintillator light production, propagation, and detection. Also, it depends on the characteristics of the electronics and of the triggering system. The Borexino MC simulation was designed and optimized to fully model and reproduce all these processes up to the signal detection [13].

The MC simulation chain consists of a set of numerical codes that:

1. provides a wide range of event generators, from solar neutrino interactions, to radioactive decays, geoneutrinos, and calibration source events.
2. simulates the energy loss of each specific particle in every material present in the detector, either active (the scintillator, buffer liquid, and water in the muon detector) or passive.
3. generates a number of scintillation or Cherenkov photons considering the particle energy loss in the media and the properties of the scintillator and/or the buffer.
4. tracks each single optical photon including its interactions with the scintillator and with the materials, until a PMT is reached or the photon is absorbed.
5. generates the PMT response for photons absorbed at the PMT cathode, considering the quantum efficiency of each individual PMT.
6. generates the PMT pulse signal taking into account the specific design of the front end and of the digital electronics chain of Borexino.
7. simulates the trigger generation and save the final output for triggering events.
8. produces a raw data file with the same structure as the one produced by the Borexino data acquisition system.

In detail, the code is structured in three separate programs, which have to be chained:

- the event generation and light tracking, accomplishing the tasks 1 to 5.

- the simulation of the electronics response, realizing the items 6 to 8.
- the event reconstruction, that converts the binary data generated by the DAQ into physical observables, such as number of photoelectrons, event position, pulse shape variables. This code is the same for both real and MC data.

The code developments were driven by the constant comparison of simulations with calibration and real data [13].

To simulate the events happening in the LS, the MC code needs a large amount of parameters to be fixed and set as an input. These parameters involve attenuation lengths of all detector materials, for α and β events the time profile of light emitted and the energy scale. The MC based fit method requires a generation of energy spectra of solar neutrinos and all background components. The Monte Carlo shapes are generated with uniform spatial distribution in the inner vessel and each run (run is a time window of data acquisition up to 6 hours, during data acquisition the data is stored, every run starts with precalibration of PMTs) is simulated individually, with its true experimental conditions. The correct number of working channels is taken into account, in order to weight the distribution of the working channels in the MC the same way as in real data. For every species the number of events is about 100 times higher than in real data, for neglecting the statistical fluctuations of MC spectra. ^{14}C and ^{210}Po are the only exception, because there is already a lot of events. The fit is then performed by means of the simulated energy spectra for all species [21].

All PMTs in Borexino detector have a slightly different light detection efficiencies, because of different intrinsic properties of the photocathodes. In order to evaluate the effective quantum efficiencies, real events in the center of the detector with radius $R = 2$ m are selected. The ^{14}C events are selected to compute the effective quantum efficiency, because there are a lot of ^{14}C events and their distribution is uniform and rate is steady [15].

3.4 Neutrino detection

Solar neutrinos reach the Earth as a mixture of all neutrino flavors (electron, muon, and tau) due to the flavor conversion mechanism enhanced by the MSW effect, for more details see Chapter 2.2.1. In Borexino, the low energy neutrinos are detected by means of their elastic scattering on electrons:

$$\nu_x + e \rightarrow \nu_x + e. \quad (39)$$

The charged current interactions, mediated by W^\pm bosons, is possible only for electron neutrinos, the neutral current interactions, mediated by the Z^0 boson, is sensitive to all neutrinos. Hence the cross section for electron neutrinos is $\sigma \sim 10^{-44} - 10^{-45} \text{ cm}^2$ [9] and at 1 MeV the cross section for other species is about five times smaller [20].

As shown in Feynman diagrams in Figure 7, a fraction of the incoming neutrino energy E_ν is transferred to one electron, which deposits it in the LS. The scintillator light is detected by ~ 2000 PMTs, which ensures high detection efficiency of photoelectrons (p.e.) produced by incident optical photons at their photocathodes. For ^7Be ($E_\nu = 0.384$ and 0.862 MeV) and pep ($E_\nu = 1.44$ MeV) neutrinos, the induced electron recoil endpoints are 0.230 MeV, 0.665 MeV, and 1.22 MeV, respectively. For the continuous pp and ^8B spectra, they are 0.261 MeV and 15.2 MeV, respectively.

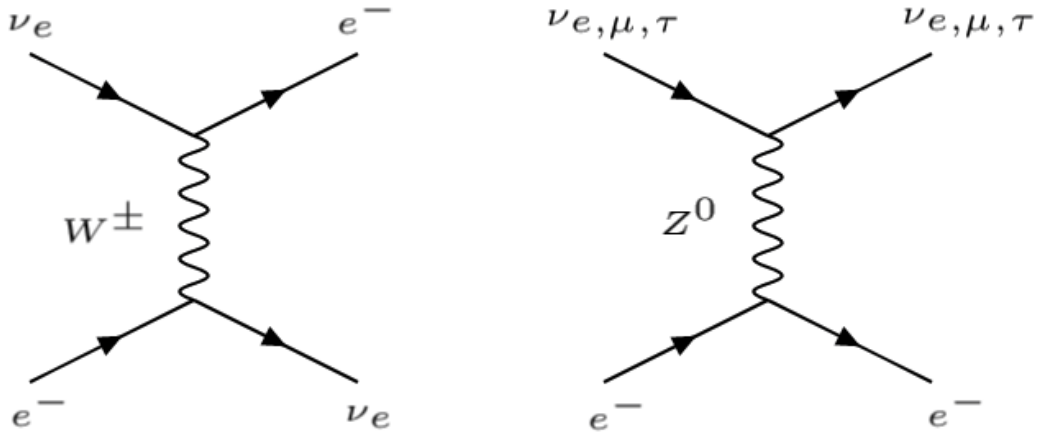


Figure 7: Feynman diagrams of the possible weak interactions between neutrinos and electrons. Left: charged current (CC) interaction, exclusively between ν_e and electron, where a charged W^\pm boson is exchanged. Right: neutral current (NC) interaction between a neutrino and an electron via the exchange of a Z^0 boson.

3.5 Backgrounds

In order to obtain solar neutrino results, it was important to achieve extremely low background levels in Borexino detector, this was accomplished after several purifications. The different background components can be classified as external backgrounds (coming from outside the scintillator, i.e. from the SSS, PMTs, and nylon vessel), internal backgrounds (due to radioactive decays of nuclei contaminating the liquid), and cosmogenic backgrounds (associated with the cosmic muon and their unstable products).

3.5.1 External backgrounds

The external background in Borexino is defined as events generated outside the scintillator and the main source of external background is the radioactivity of the materials that contain and surround the scintillator (the vessel and its support structure, PMTs, and other hardware mounted on the stainless steel sphere). Hence the radioactive decays occur outside the scintillator, the only background that can reach the inner volume are γ -rays. The leading backgrounds are the γ -rays from ^{208}Tl , ^{214}Bi , which comes from ^{238}U and ^{232}Th chains, and ^{40}K contaminants in the PMTs. The rate of the external background is not very important for ^7Be , pep , and CNO ν measurement after the FV cut, but it is crucial for the determination of ^8B ν . If one wants to reduce the contribution of external γ s, it is possible to reduce the FV for that or insert the radial distributions of the events in the fit procedure with a multivariate approach, for more information see Chapter 4.1.

3.5.2 Internal backgrounds

The internal backgrounds in Borexino detector are defined as events generated by the decay of radioactive isotopes contaminating the scintillator. In the following the main internal backgrounds are being discussed, their sources, rates, and life-times.

^{238}U and ^{232}Th chains

Internal background in the detector can potentially be due to radioactive isotopes belonging to the natural ^{238}U and ^{232}Th decay chains.

^{238}U is a primordial radioactive isotope with a mean-life of 4.468 billion years, as shown in decay chain in Figure 8. The concentration of contaminants of the ^{238}U chain in secular equilibrium can be measured in detector by identifying the fast sequence ^{214}Bi - ^{214}Po that offers a delayed coincidence tag. These two isotopes are ^{222}Rn daughters and the hypothesis of secular equilibrium is sometimes invalid due to radon diffusion through surfaces or a possible contamination of the scintillator with radon coming from the air. The number of ^{214}Bi - ^{214}Po coincidences has been monitored continuously during the data taking. The ^{238}U concentration ($< 9.4 \times 10^{-20}$ g/g (95% C.L.)) in Phase-II in the scintillator has been inferred from the ^{214}Bi - ^{214}Po rate in the FV in absence of operations.

The primordial isotope ^{232}Th has a mean-life of 14.1 billion years. As can be seen from Figure 9, the main decay branches of the ^{232}Th include six α and four β decays. The fast decay sequence of ^{212}Bi - ^{212}Po allows to estimate the ^{220}Rn content of the scintillator and to infer the ^{232}Th contamination. The intrinsic contamination of ^{232}Th has been measured from these coincidences and corresponds to $< 5.7 \times 10^{-19}$ g/g (95% C.L.) in Phase-II.

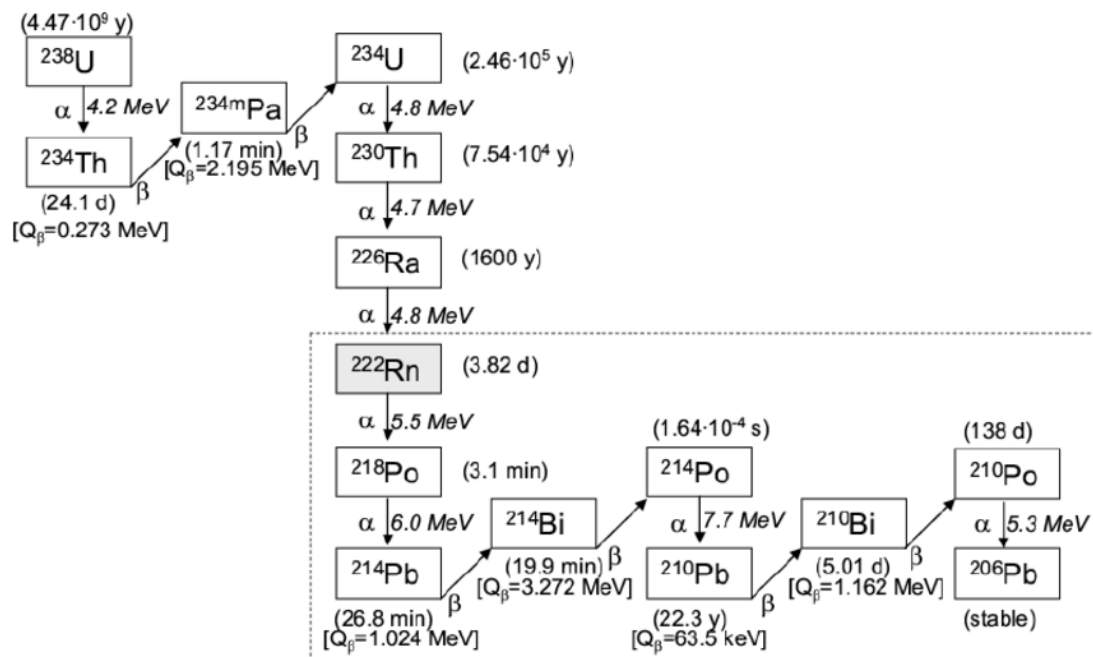


Figure 8: The ^{238}U decay chain showing isotopes, life-times, maximum released energies and type of decays.

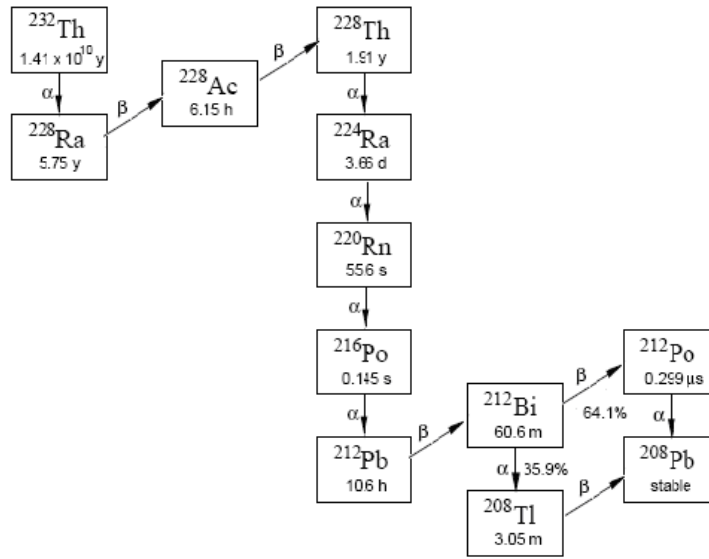


Figure 9: The ^{232}Th decay chain showing isotopes, life-times, maximum released energies and type of decays

^{222}Rn

In period from 2010 - 2011, so called *Water Extraction* (WE) period, there was a large amount of ^{214}Bi - ^{214}Po events in the Borexino detector, as shown in Figure 10. ^{214}Bi is a daughter of ^{222}Rn coming from air and itself β decays into ^{214}Po , which quickly α decays. Both of the ^{214}Bi and ^{214}Po events are distributed in the northern part of the detector between radius of 3 and 4 m. These events allows us to study and work out methods to distinguish between α and β events in order to be able to prove ^{210}Bi homogeneity and stability in the detector.

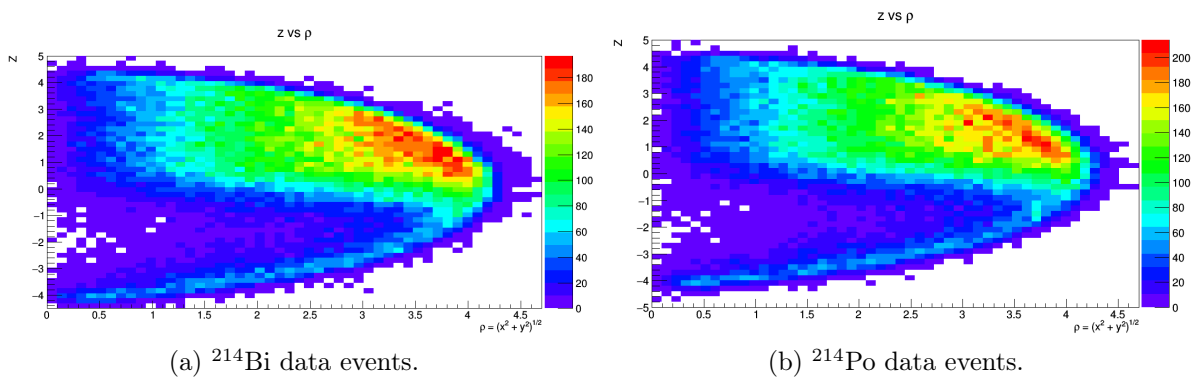


Figure 10: Distribution of ^{214}Bi - ^{214}Po events in the detector during *Water Extraction* (WE) period. It can be seen how most of the events are distributed in the northern part of the detector between radius of 3 and 4 m.

The MC simulations of ^{214}Bi and ^{214}Po was performed for 2148 runs, starting from June 16, 2010 and ending on August 11, 2011. The ^{214}Bi events were simulated by MC according to the spatial distribution observed in data. The ^{214}Po events were simulated

similarly, but uniformly in the vessel.

In Figure 11 one can see the distribution of ^{214}Bi MC events in the IV of the detector with its total number of events and also separately for north (blue line) and south (red line) of the detector. Northern part represents, when having horizontal "cut" at z -axis $z > 0$ m in the detector and southern part is respectively where $z < 0$ m.

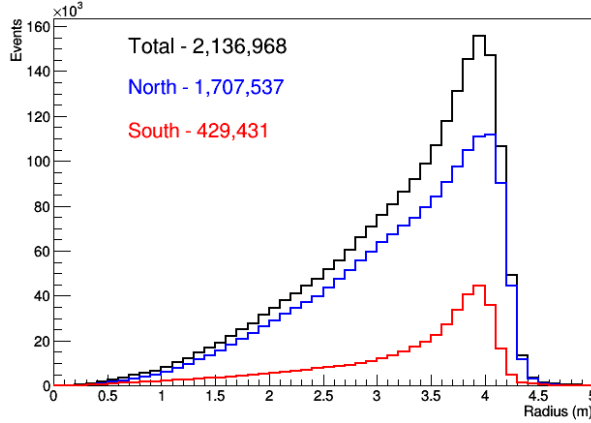


Figure 11: Radial distribution of ^{214}Bi MC events in the IV. Black line represent total number of events, blue and red lines are for events in north ($z > 0$) and south ($z < 0$) part of the detector respectively.

^{210}Pb

^{210}Pb is a β -emitter in the ^{238}U -decay chain. Due to its long mean-life (32 years) and its tendency to absorb on to surfaces, it is often found out of secular equilibrium with the rest of the chain. While ^{210}Pb itself is not a problem, since its end-point at 63.5 keV is well below the energy region of interest for solar neutrinos, its daughters, ^{210}Bi and ^{210}Po , are a major source of background in Borexino and will be discussed below.

^{210}Bi and ^{210}Po

^{210}Bi is a β -emitting daughter of ^{210}Pb with 5.01 days mean-life and a Q-value of 1160 keV. To identify exact rate of ^{210}Bi is very crucial for the current analysis of measuring the CNO ν s because their spectras are very similar and the determination of the contribution of both species through the fit with both components free is thus impossible. An independent measurement of the ^{210}Bi with a comparatively good accuracy is needed to have an handle to single out the CNO contribution.

^{210}Po is after ^{14}C the most abundant component of the detected spectrum. It is a monoenergetic 5300 keV α -emitter with 138 days mean-life. However the ^{210}Po spectrum appears as a clear peak at around 420 keV, within the ^7Be energy region, due to the strong quenching of α s in the LS. Even though it is a direct daughter of the ^{210}Bi , the rate of ^{210}Po has been always largely out of equilibrium with respect to its precursors in the ^{238}U chain, as well as with ^{210}Pb . This contamination is probably originating from the pipes used to fill the detector. This polonium excess is unsupported and therefore decays with its lifetime of 138 days: after several years from the last massive detector operation (the 2010-2011 purifications), we are now approaching a condition in which the unsupported ^{210}Po is very low. This is crucial point for the possibility to measure

the ^{210}Bi contribution. The identification of ^{210}Po events is quite easy since it α decays, which can be efficiently separated from β via pulse-shape discrimination techniques, more information in Chapter 5.

The ^{210}Bi and ^{210}Po MC events were simulated in 3.75 m radius with an enhancement factor 1000. The simulations were produced for 7137 runs, starting from December 11, 2011 and ending on August 20, 2017. ^{210}Bi MC is produced homogenously in the detector, when ^{210}Po MC follows the realistic distance.

In Figure 12a one can see the distribution of ^{210}Bi MC events in the IV of the detector with its total number of events and also separately for north ($z > 0$) (blue line) and south ($z < 0$) (red line) of the detector. In Figure 12b the ^{210}Po MC events can be seen.

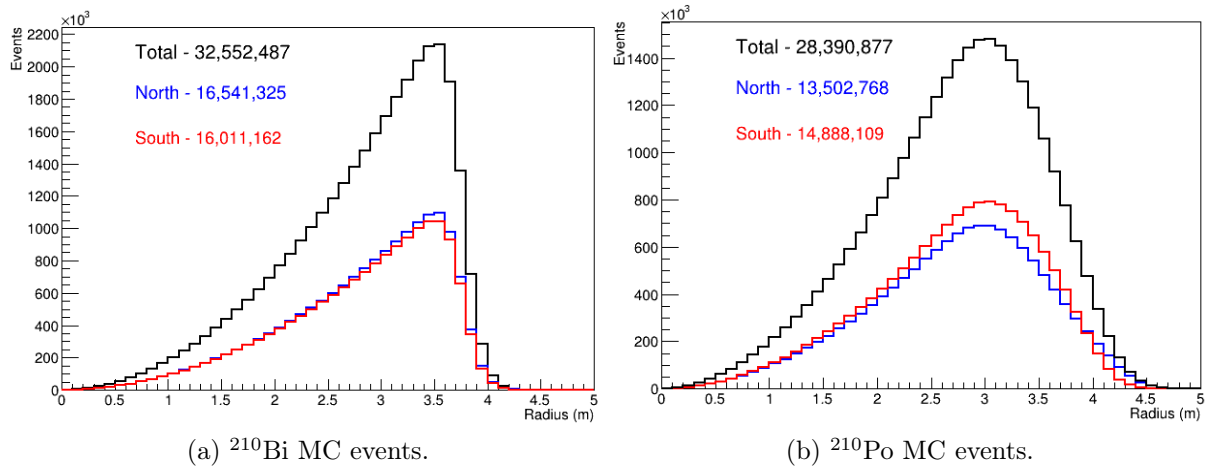


Figure 12: Radial distribution of ^{210}Bi - ^{210}Po MC events in the IV. Black line represent total number of events, blue and red lines are for events in north ($z > 0$) and south ($z < 0$) part of the detector respectively.

^{85}Kr

The ^{85}Kr is a β emitter with 687 keV end-point and 10.756 years mean-life. Its spectral shape is very similar to the electron recoil spectrum due to the $^7\text{Be}-\nu$ and therefore it was one of the most important background in the ^7Be analysis. It is present in the air mostly because of human-caused nuclear explosions. Hence, even extremely small air exposures during the detector-filling operations would yield significant contamination, avoiding air exposure of fluids is extremely important in order to limit the increasing of ^{85}Kr related background level.

^{14}C and pile-up

^{14}C is a β -emitter that occurs as a natural isotope of carbon with an end-point of 156 keV, produced by cosmic rays interacting with ^{14}N in atmosphere. Borexino detector was filled with pseudocumene obtained from underground sources in which the relative abundance of ^{14}C is low, because ^{14}C has a geologically short mean-life ($\tau = 8270$ years). However, ^{14}C is still the most abundant source of background in detector with decay rate approximately 40 Hz/100 t, in comparison, this is almost five orders of magnitude larger than the measured ^7Be rate (~ 48 cpd/100 t).

In some cases, two physical events can take place in a short time window, then these two events will be registered as a single event, and are called pile-up. Because of the high rate of ^{14}C events, this is the component that generates the most of pile-up. Nevertheless, all species can, in principle, create pile-up.

3.5.3 Cosmogenic backgrounds

The muons coming from cosmic ray interactions in the atmosphere are reduced in the Borexino detector thanks to the Gran Sasso mountain. Still about $1.2 \text{ muons m}^{-2}\text{h}^{-1}$ [22] are able to penetrate the shielding rock, this means about 4300 muons entering the inner part of the detector a day. The events due to muons must be identified. Because of the water Cherenkov detector veto the muon events with immense amount of energy are easily rejected when crossing the scintillator.

^{11}C is one of the most dominant muon-induced cosmogenic backgrounds in the liquid scintillator, which represents the biggest challenge for the measurement of *pep* ν and CNO ν . It has a quite constant concentration in the scintillator ($\sim 30 \text{ cpd}/100\text{t}$) [9] determined by the equilibrium between its production and decay rate and cannot be reduced by any purification procedure. In 95% of the cases, ^{11}C is produced together with at least one neutron:



Then the ^{11}C decays with mean-life $\tau = 29.4$ minutes via positron emission:



The mean-life of ^{11}C is too long to apply a veto on the whole detector after every muon, hence the ^{11}C contamination has to be removed with a more complicated approach. The *Three-Fold Coincidence* (TFC) method vetoes space-time regions of the detector after coincidences between the neutron capture and the parent muon, in order to exclude the subsequent of ^{11}C decay.

4 Borexino Solar neutrino analysis

4.1 Proton-proton cycle

This chapter is an introductory chapter into the work done by Borexino collaboration, which concluded with paper "Comprehensive measurement of pp-chain solar neutrinos", and was published by Nature in October 2018 [9].

The first complete study of all the components of the proton-proton-chain neutrinos was performed by Borexino. This means the interaction rates of pp , ${}^7\text{Be}$, pep neutrinos with the highest precision to date were measured, and of ${}^8\text{B}$ neutrinos with the lowest-threshold. Also a limit was set on the hep neutrino flux, for more details about different solar neutrino components see Chapter 2.1.1. These measurements provide a direct determination of the pp-II/pp-I branching ratio and a first indication that the metal content in the Sun's core is more compatible with solar models assuming high surface metallicity. Also the survival probability P_{ee} of solar electron neutrinos at different energies was determined, studying simultaneously and with high precision the MSW-LMA (see Chapter 2.2.1) flavor conversion paradigm in the vacuum and in the matter dominated regions.

The analysis has been divided into two energy ranges that are affected by different backgrounds. A Low Energy Region (LER) (0.19 - 2.93 MeV), for measuring the pp , ${}^7\text{Be}$, and pep ν interaction rates and giving an upper limit on CNO ν . And a High Energy Region (HER) (3.2 - 16 MeV), for measuring ${}^8\text{B}$ - ν s and giving an upper limit on the hep ν rate. The HER is also divided into two sub-regions, below and above 5.7 MeV (HER-I and HER-II). The measurement of ${}^8\text{B}$ ν s cannot be extended below 3.2 MeV because of the 2.614 MeV γ -ray background from ${}^{208}\text{Tl}$ decays, originating from trace ${}^{232}\text{Th}$ contamination of the thin nylon LS-containment vessel.

LER

Borexino Phase-II data was used in the LER analysis (for more details about different phases in Borexino detector, see Chapter 3) collected between December 2011 and May 2016, in which the internal ${}^{85}\text{Kr}$ and ${}^{210}\text{Bi}$ contamination was reduced with respect to Borexino Phase-I. The total LER exposure was 1291.51 days x 71.3 t.

To get only neutrino-like events a software selection is used, which means every event in the dataset will be analyzed and specific conditions are applied to select ν -like events from unwanted events. The conditions used are following: muon, multi-cluster, and ${}^{214}\text{Bi}$ - ${}^{214}\text{Po}$ coincidence pair events are removed; also all events that have a mismatch with start time, charge reconstruction, or crate noise are excluded. A FV cut has been used in LER analysis, to remove events far from the center of the ID. The FV consists of 71.3 t of scintillator, selected by applying a radial cut with $R < 2.8$ m and a cut along the z-axis with $-1.8 < z < 2.2$ m, this FV is called ***pep* FV**. Separately from these conditions, a special Three-Fold coincidence (TFC) method is used, this does not remove any events, but it divides the sample into two categories: with all and low rate of ${}^{11}\text{C}$ events.

The multivariate fit method was used to get results (precise measurement or an upper limit for each neutrino species), this means a reference samples of all the contributing components were fitted to the energy spectrum of the Borexino events from the data sample (after the cuts were applied), CNO ν s were constrained to SSM LZ or HZ values. The produced values of neutrino and background events are expressed in counts per day per 100 tons (cpd/100t) of the scintillator.

In Figure 13 the multivariate fit energy spectras are showed, in left hand side we have *TFC-tagged* and on right hand side *TFC-subtracted*. Also the radial distribution of the selected neutrino events are fitted to separate the internal and external event contribution, as shown in Figure 14a. The pulse-shape variable distribution was made to distinguish electron and positron events, it is used to disentangle the remaining ^{11}C events in the *TFC-subtracted* spectrum.

An indirect constrain is applied on *pep* ν s using the values predicted by HZ-SSM(LZ-SSM) (for more details see Chapter 2.1.3) and including the effect of MSW-LMA oscillations, the ratio of *pp* and *pep* neutrino interaction rates can be given as $R(pp/pep) = (47.8 \pm 0.8)$ ($R(pp/pep) = (47.5 \pm 0.8)$), respectively and yields identical results. Then an upper limit of the CNO ν interaction rate is obtained.

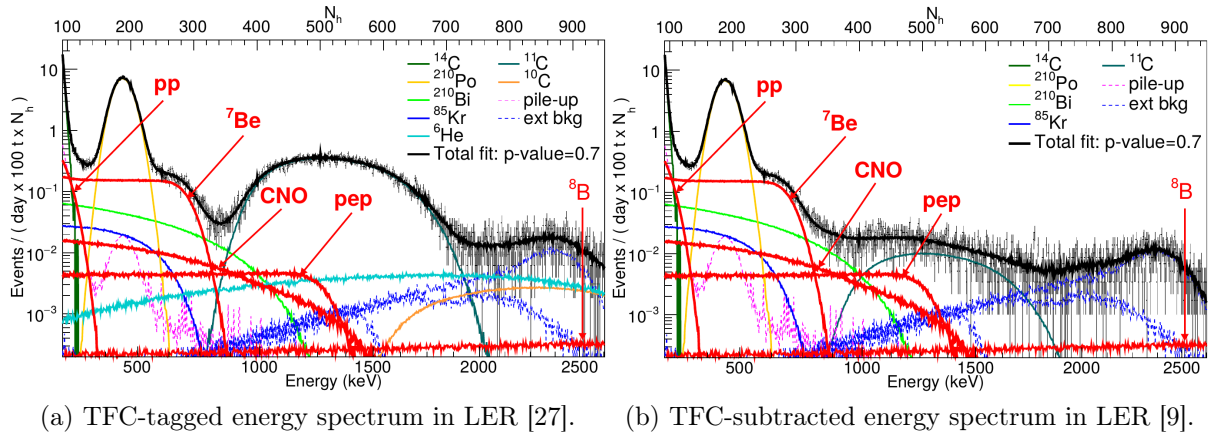


Figure 13: Results of the multivariate fit. Distribution of events after selection cuts and corresponding fits with neutrino and background components.

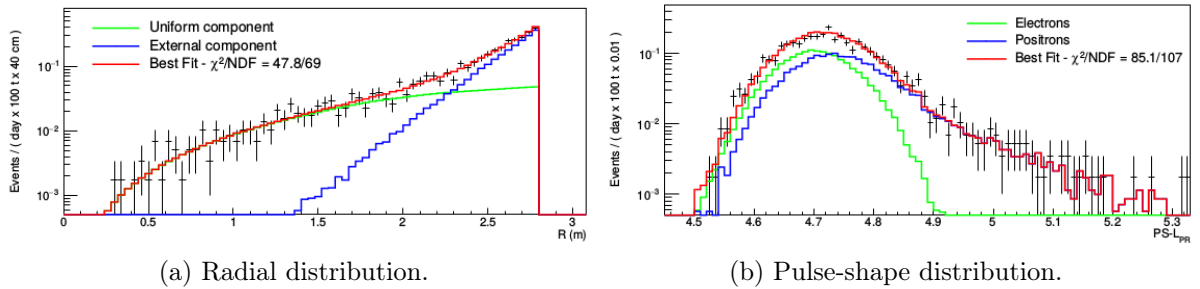


Figure 14: Multivariate fit of the radial and the pulse-shape distributions of the events with black crosses in low energy region [27].

HER

In HER analysis a larger data set was used, because it is not so sensitive to internal background, collected between January 2008 and December 2016, for a total exposure of 2062.4 days x 266.0 (227.8) t for HER-I(II), respectively.

The selection of data is similar to that in LER described above, the difference comes from that the energy regions are affected by different types of background events. The

conditions used in HER are following: the neutrons, ^{10}C , ^{214}Bi - ^{214}Po coincidence pairs, and muons with cosmogenic isotopes after internal muons are being removed. In addition a FV cut is being used in HER-I analysis, because it is important to suppress background events related to a small pin hole in the nylon vessel that causes scintillating fluid to the leak into the region surrounding it, hence the HER-I analysis uses only $z < 2.5$ m cut and it consists of 227.8 t of scintillator. HER-II analysis uses the entire scintillator with 266 t in volume.

In the HER-I/II, the analysis is based on a fit to the radial distribution of the events to separate the ^8B νs signal from the external background components, as shown in Figure 15.

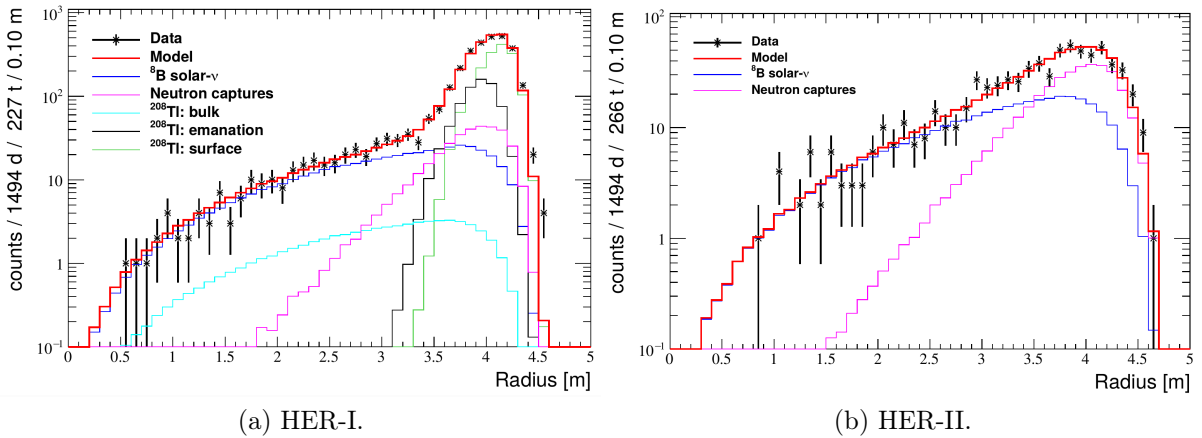


Figure 15: Fit of the radial distribution of events in the High Energy Region [28].

Results:

The high precision solar neutrino results obtained by LER and HER analyses are summarized in Table 3. Assuming the low metallicity (LZ) or high metallicity (HZ) models (for CNO ν constrain) affected only the pep νs and these results are presented separately. The second column shows the measured rates of corresponding neutrinos, quoted for zero threshold. In the third column, the measurements were translated into the corresponding solar neutrino fluxes using the known electron and μ/τ neutrino cross sections and the flavor composition calculated according to the MSW-LMA paradigm. The fourth column presents the theoretical fluxes predicted by the Standard Solar Model under the high and low metallicity assumptions.

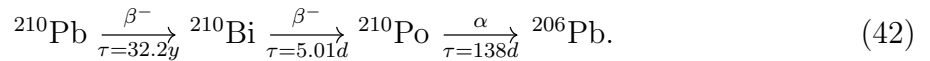
Solar ν	Rate [cpd/100 t]	Flux [$\text{cm}^{-2}\text{s}^{-1}$]	Flux - SSM predictions [$\text{cm}^{-2}\text{s}^{-1}$]
pp	$134 \pm 10_{-10}^{+6}$	$(6.1 \pm 0.5_{-0.5}^{+0.3}) \cdot 10^{10}$	$5.98(1. \pm 0.006) \cdot 10^{10}$ (HZ) $6.03(1. \pm 0.005) \cdot 10^{10}$ (LZ)
${}^7\text{Be}$	$48.3 \pm 1.1_{-0.7}^{+0.4}$	$(6.1 \pm 0.5_{-0.5}^{+0.3}) \cdot 10^{10}$	$4.93(1. \pm 0.006) \cdot 10^9$ (HZ) $4.50(1. \pm 0.006) \cdot 10^9$ (LZ)
pep (HZ)	$2.43 \pm 0.36_{-0.22}^{+0.15}$	$(6.1 \pm 0.5_{-0.5}^{+0.3}) \cdot 10^{10}$	$1.44(1. \pm 0.009) \cdot 10^8$ (HZ) $1.46(1. \pm 0.009) \cdot 10^8$ (LZ)
pep (LZ)	$2.65 \pm 0.36_{-0.24}^{+0.15}$	$(6.1 \pm 0.5_{-0.5}^{+0.3}) \cdot 10^{10}$	$1.44(1. \pm 0.009) \cdot 10^8$ (HZ) $1.46(1. \pm 0.009) \cdot 10^8$ (LZ)
${}^8\text{B}_{\text{HER-I}}$	$0.136_{-0.013}^{+0.013} \quad {}_{-0.003}^{+0.003}$	$(6.1 \pm 0.5_{-0.5}^{+0.3}) \cdot 10^{10}$	$5.46(1. \pm 0.12) \cdot 10^6$ (HZ) $4.50(1. \pm 0.12) \cdot 10^6$ (LZ)
${}^8\text{B}_{\text{HER-I}}$	$0.0876_{-0.010}^{+0.080} \quad {}_{-0.005}^{+0.005}$	$(6.1 \pm 0.5_{-0.5}^{+0.3}) \cdot 10^{10}$	$5.46(1. \pm 0.12) \cdot 10^6$ (HZ) $4.50(1. \pm 0.12) \cdot 10^6$ (LZ)
${}^8\text{B}_{\text{HE}}$	$0.223_{-0.016}^{+0.015} \quad {}_{-0.006}^{+0.006}$	$(6.1 \pm 0.5_{-0.5}^{+0.3}) \cdot 10^{10}$	$5.46(1. \pm 0.12) \cdot 10^6$ (HZ) $4.50(1. \pm 0.12) \cdot 10^6$ (LZ)
CNO	< 8.1 (95 %C.L.)	$(6.1 \pm 0.5_{-0.5}^{+0.3}) \cdot 10^{10}$	$4.92(1. \pm 0.11) \cdot 10^8$ (HZ) $3.52(1. \pm 0.10) \cdot 10^8$ (LZ)
hep	< 0.002 (90 %C.L.)	$(6.1 \pm 0.5_{-0.5}^{+0.3}) \cdot 10^{10}$	$7.98(1. \pm 0.30) \cdot 10^3$ (HZ) $8.25(1. \pm 0.12) \cdot 10^3$ (LZ)

Table 3: Borexino solar neutrino results. The rates and fluxes are integral values without any threshold. [9]

4.2 Towards CNO measurement

After the first complete study of all the components of the pp -chain performed by Borexino, the next step is to detect CNO solar neutrinos. The main complication to detect CNO solar neutrinos arises due to its spectral shape, which is similar to the radioactive ${}^{210}\text{Bi}$ decay in the liquid scintillator and the pep -neutrinos, as it can be seen in Figure 16. Therefore, the precise measurement of CNO neutrinos directly depends on constraining the ${}^{210}\text{Bi}$ and pep -neutrinos rate to a precise value. The pep ν s can be constrained by exploiting the theoretically known pp and pep flux ratio, or directly by constrain of the pep absolute rate.

One method to tag the ${}^{210}\text{Bi}$ rate is by its daughter particle ${}^{210}\text{Po}$.



The ${}^{210}\text{Bi}$ and ${}^{210}\text{Po}$ are coming from the ${}^{210}\text{Pb}$ decay chain, as shown in equation 42, ${}^{210}\text{Pb}$ is out of equilibrium in the liquid scintillator, which makes it more complicated to constrain ${}^{210}\text{Bi}$ decay events. Under some assumptions, by tagging the ${}^{210}\text{Po}$ events with the pulse-shape discrimination, it might be possible to infer the ${}^{210}\text{Bi}$ rate in the liquid scintillator. One could expect that ${}^{210}\text{Bi}$ and ${}^{210}\text{Po}$ are decaying in the secular equilibrium within the ${}^{238}\text{U}$ chain. But, this is not the case in Borexino, where the observed ${}^{210}\text{Po}$ rate is much higher than the ${}^{210}\text{Bi}$ rate. The out of equilibrium ${}^{210}\text{Po}$ might be due to ${}^{210}\text{Po}$ coming from the surface of the scintillator storage tanks, pipes, and IV surface.

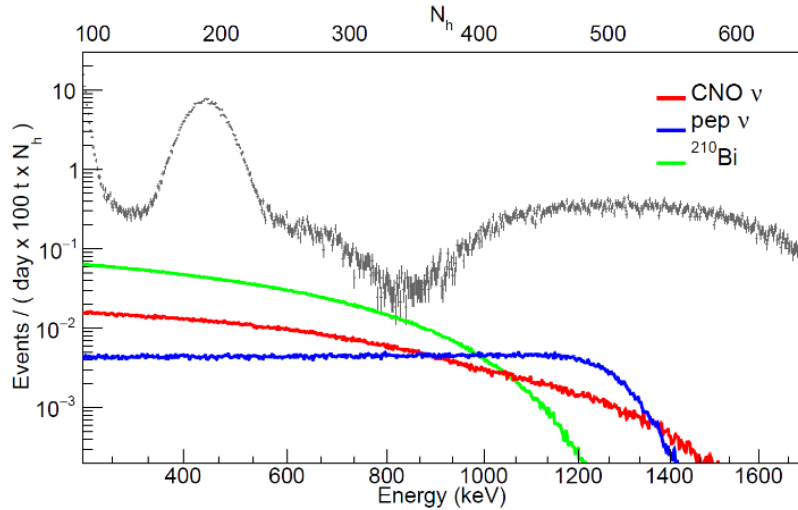


Figure 16: Fit of the distribution of CNO- ν s, pep - ν s, and internal ^{210}Bi events in Low Energy Region.

Thanks to the pulse-shape discrimination techniques, it was very efficient to tag ^{210}Po events and to study their time and space evolution. The temperature variations could trigger convection motions able to bring ^{210}Po from the outermost shells to the fiducial volume. The scintillator in contact with the vessel or its endcaps is moved inside, bringing in the contaminant. These motions are slow, with a time constant of months, and the only solution to prevent them is to assure a very stable temperature around the detector. The only way in order to thermally decouple Borexino from the environment is to insulate it. For these reasons, in 2015 the Borexino detector was covered with two layers of 10 cm thick mineral wool, as can be seen in Figure 17.



Figure 17: Pictures of the Borexino detector water tank covered with the insulation layer, in the left picture it is covered partially, and in the right one totally covered.

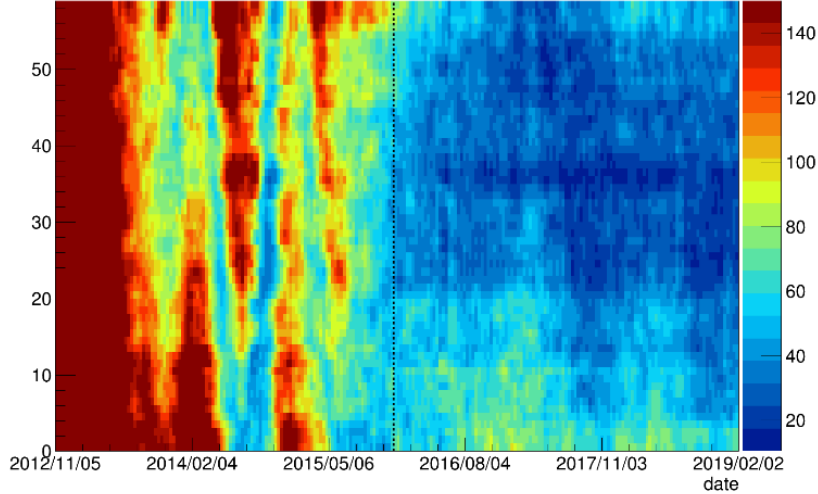


Figure 18: ^{210}Po rate in the 59 cubes from 2012 until 2019 in Borexino detector. The cube numbers go from 0 to 58, 0 being at the bottom and 58 at the top. The color scale refers to the cpd/100 t of ^{210}Po observed in each cube. The dashed vertical line indicates the end of the insulation installation.

To study the ^{210}Po spatial distribution in Borexino as a function of time on a weekly basis, the innermost FV is divided in 59 cubes of 1.5 m^3 each, as can be seen in Figure 18. During the winter, ^{210}Po is brought in the FV from the bottom and in the summer it falls down from the top. The convective motions and the ^{210}Po net flux from the outer shells towards the FV observed before the summer 2015 made it impossible to establish ^{210}Bi through the ^{210}Po tagging. The Figure 18 shows that the insulation, besides stabilizing the temperatures, worked very effectively in reducing the convective motions inside the scintillator. After the completion of the insulation installation, in fact, the ^{210}Po distribution looks more uniform. This seems very promising in order to try to extract a ^{210}Bi constraint through ^{210}Po .

At a secular equilibrium, the rate of ^{210}Bi is equal to the rate of ^{210}Po , this could make it possible to measure the ^{210}Bi rate from the ^{210}Po rate.

After improving the thermal stability of the detector, we can find a volume large enough, where the contamination of ^{210}Po is equal or bigger than the contamination ^{210}Bi decay, as shown in the ideal case in Figure 19. In order to claim the CNO solar neutrino evidence it is important to do fit with ^{210}Bi constrained. An upper limit of ^{210}Bi decay rate is needed in order to get an lower limit on CNO discovery. In order to get the upper limit of ^{210}Bi rate from ^{210}Po decay rate, and the main goal of this work is to use the counting analysis to prove the the major background ^{210}Bi rate is stable and homogenous in the liquid scintillator. This request is even more important, if the ^{210}Po supported term, and thus the intrinsic ^{210}Bi contamination of the LS, is determined in a volume that is different and significantly smaller than the FV for spectral fit.

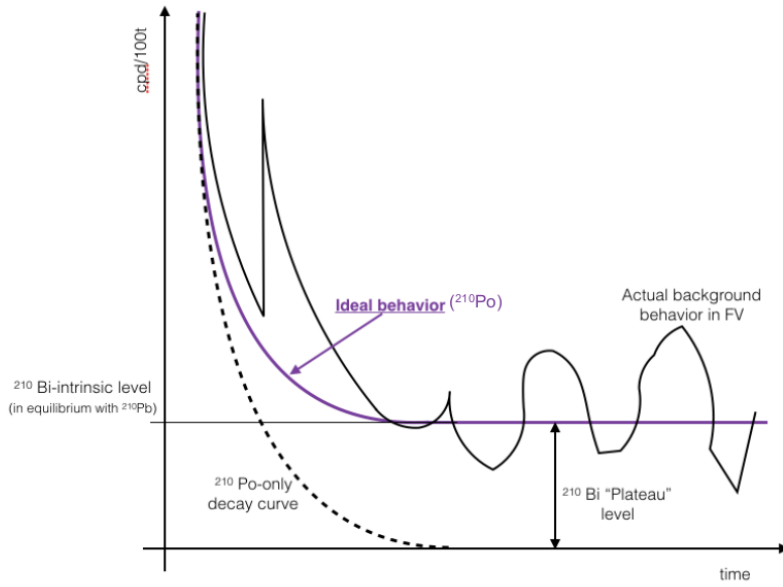


Figure 19: ²¹⁰Po and ²¹⁰Bi expected rates in time.

5 Performance of α/β discriminators

5.1 Types of discriminators

In the next section different types of pulse-shape discriminators used in this work are introduced and in the conclusion the best choice for the next analysis is selected.

The α/β discrimination in Borexino is based on that α pulses have a longer tail with respect to β pulses. The reference shapes of α and β are from ^{214}Po (red) and ^{214}Bi (black) (from WE data, shown in Figure 10), are shown in Figure 20 [14]. The discrimination is based on that the time distribution of scintillation photons depends on the details of energy loss and it is different for α and β particles. Since α particles have higher charge and mass they have higher energy loss in the liquid scintillator. The mean time of the hit times in the cluster are different for the two particles, as shown in the Figure 20.

In the next sections the Gatti parameter, *Multi-Layer Perceptron* (MLP), and *Fully Connected Network* (FCN) discriminators are being described.

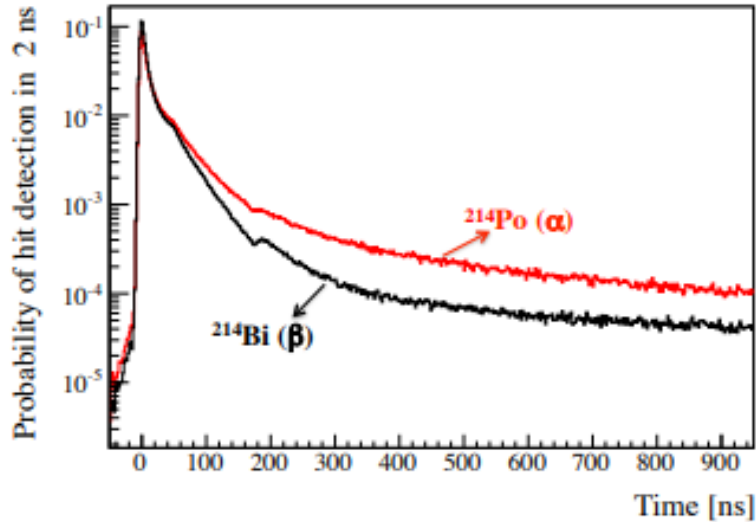


Figure 20: The reference pulse shapes obtained by tagging the radon correlated ^{214}Bi (black line) - ^{214}Po (red line) coincidences, from WE data. [14]

5.1.1 Gatti parameter

The Gatti filter is a linear discrimination technique which allows to separate two classes of events with different but known time distributions of the detected light. The Gatti parameter G is defined as [14]:

$$G = \sum_n e(t_n)w(t_n), \text{ where } w(t_n) = \frac{P_\alpha(t_n) - P_\beta(t_n)}{P_\alpha(t_n) + P_\beta(t_n)}, \quad (43)$$

where $P_\alpha(t)$ and $P_\beta(t)$ are the probabilities, that a photoelectron is detected at a time between t and $t + dt$ for α and β events. In Borexino, this technique was developed using the ^{214}Bi - ^{214}Po coincidence sample from WE as typical β and α samples used to define the weights $w(t_n)$ in the equation 43.

The distribution of the corresponding G parameter is shown in Figure 21.

Selection criteria previously used for particle identification with respect to their Pulse-Shape Discriminator (PSD) parameter value is:

- α -like events > 0
- β -like events < 0

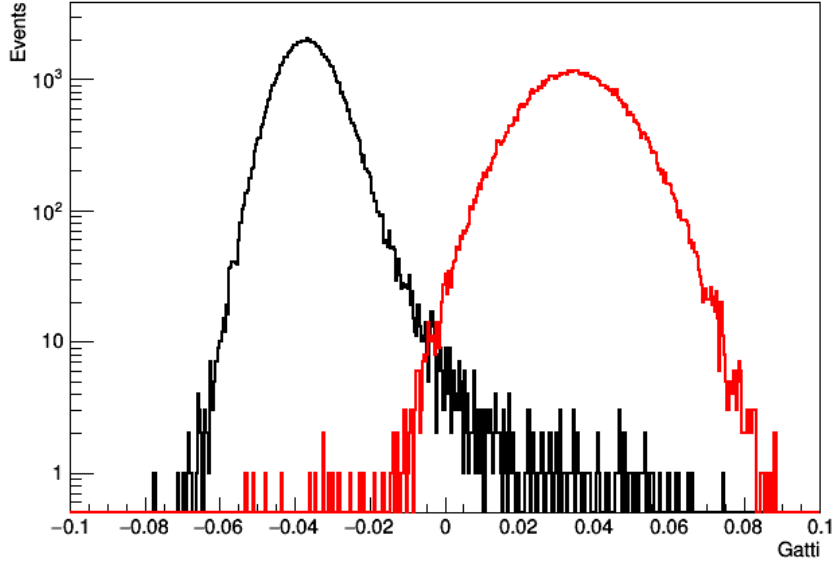


Figure 21: Gatti distribution with ^{214}Bi data events with black line and ^{214}Po data events with red line, from WE data.

5.1.2 Multi-layer perceptron

The *Multi-Layer Perceptron* (MLP) is a neural network based on an algorithm for supervised learning of binary classifiers, this means functions that can decide which class an input belongs to. This method uses many variables as inputs like different tails to totals, mean time of the hits in the cluster, kurtosis, variance and so on. The MLP is tuned on ^{214}Bi - ^{214}Po samples from WE data. It can select events through non-linear discrimination technique [11]. There are different versions of MLP (all different versions used in this work can be seen in Figure 22), which take input from different variables.

Selection criteria previously used for particle identification with respect to their MLP PSD parameter value is:

- α -like events < 0.05
- β -like events > 0.95

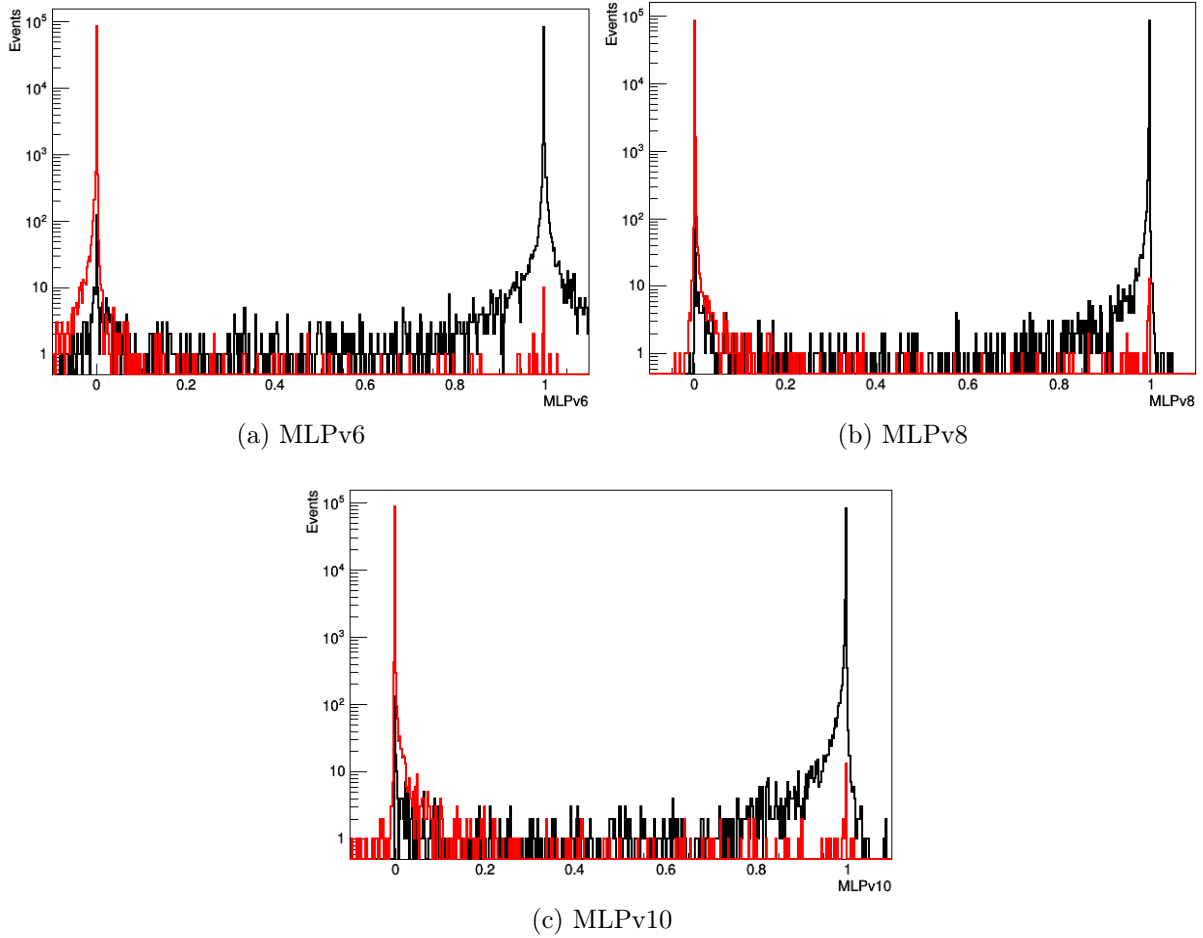


Figure 22: *Multi-layer perceptron* (MLP) distributions with ^{214}Bi (β -like events) data events with black line and ^{214}Po (α -like events) data events with red line, from WE data.

In Figures 22a, 22b, and 22c one can see the MLP distribution, with red line we have α -like ^{214}Po data events with different MLP variables and one can see how they are mostly distributed near 0 on the x-axis. With black line we have β -like ^{214}Bi data events with different MLP variables and one can see how they are mostly distributed near 1 on the x-axis.

5.1.3 Fully connected network

The *Fully Connected Network* (FCN) is also based on neural network which is a series of algorithms that endeavors to recognize underlying relationship in a set of data through a process that mimics the way the human brain operates. The FCN variable takes input hit times after time of flight subtraction. There are two FCN variables, one is called FCN214, which is tuned on ^{214}Bi - ^{214}Po samples (see Chapter 3.5) and the other FCN210 is tuned on ^{210}Bi and ^{210}Po MC events (see Chapter 3.5).

FCN distributions can be seen in Figure 23, where with red line we have α -like ^{214}Po data events, one can see how they are mostly distributed near 0 on the x-axis, with black line we have β -like ^{214}Bi data events and one can see how they are mostly distributed near 1 on the x-axis.

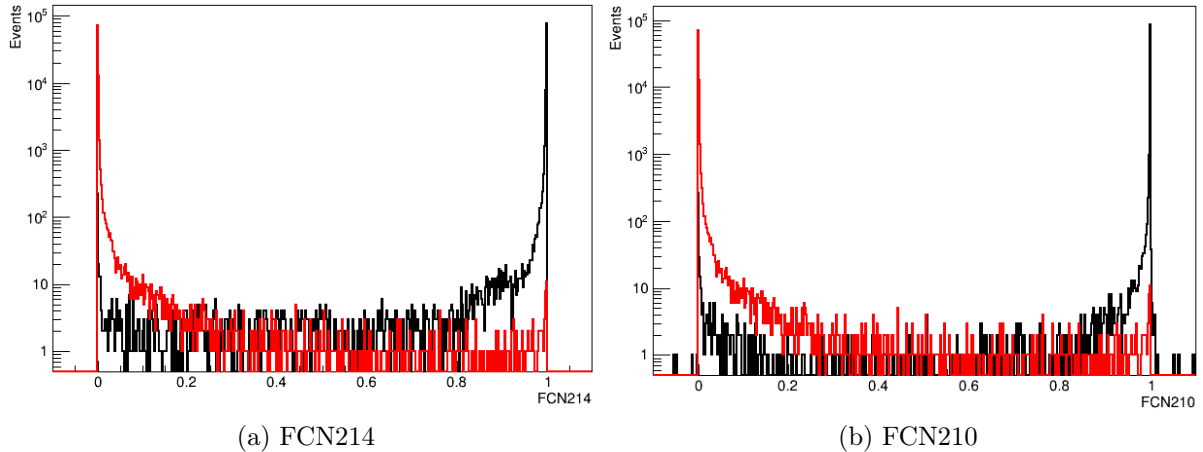


Figure 23: *Fully connected network* (FCN) distributions with ^{214}Bi data events with black line and ^{214}Po data events with red line, from WE data.

5.2 Threshold optimization

To look for pure α -events (^{214}Po and ^{210}Po) or β -events (^{214}Bi and ^{210}Bi) with selected discriminator, it is important to optimize the threshold cut (the threshold cut for different pulse-shape discriminators shown in Figures 21, 22, and 23 is defined as a separator between α -like events and β -like events). In order to optimize the threshold cut, one has to define efficiency (as true events), leakage (as misidentified events), and *Figure of Merit* (FOM).

Firstly, the **efficiency** ε :

$$\varepsilon = \frac{E_1}{E_{tot}}, \quad (44)$$

where E_1 is the number of true events within a selected threshold cut, E_{tot} is total number of this type of events.

In this work two efficiencies are being specified: α -efficiency, which is plotted in Figure 24a and β -efficiency, which is plotted in Figure 24b as a function of threshold for different discriminators.

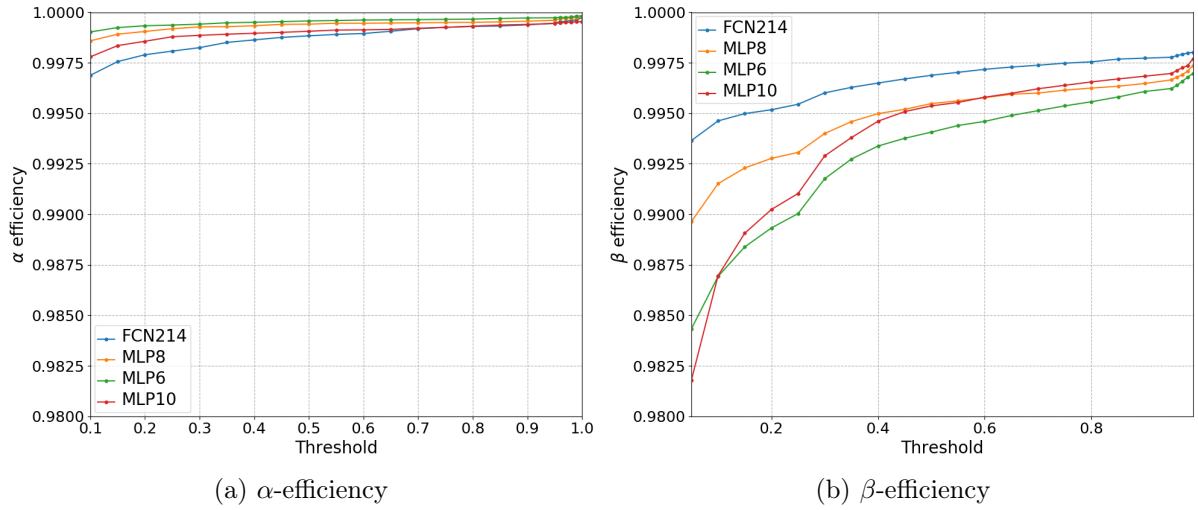


Figure 24: Efficiency dependency on a threshold cut for different pulse-shape discriminators obtained by ^{214}Po and ^{214}Bi WE data events.

Secondly, it is relevant to define **leakage** L :

$$L = \frac{L_1}{L_{tot}}, \quad (45)$$

where L_1 is number of misidentified events within a selected threshold, L_{tot} is total number of one type of events.

In this work, two leakages are being specified: α -leakage, which is plotted in Figure 25a, and β -leakage, which is plotted in Figure 25b as a function of threshold for different discriminators.

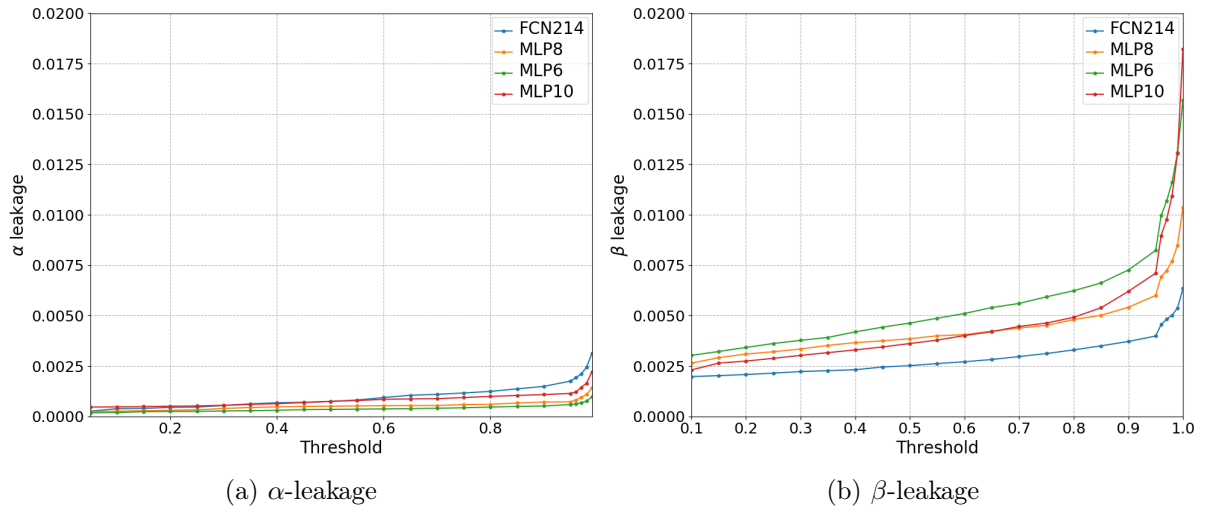


Figure 25: Leakage dependency as a threshold cut for different pulse-shape discriminators obtained by ^{214}Po and ^{214}Bi WE data events.

5.2.1 Figure of merit calculations

Two FOM were defined to optimize the best threshold cut for each discriminator for studies of homogeneity of ^{210}Bi .

When looking at β -events it is important that the β -efficiency is high, while α -leakage is low. Hence the first FOM_1 was calculated by:

$$FOM_1 = \varepsilon_\beta(1 - L_\alpha)^2, \quad (46)$$

where, ε_β is the β -efficiency and L_α is the α -leakage.

The results of equation 46, can be seen in Figure 26, and separately for every discriminator in Figures 28a, 29a, 30a, 31a.

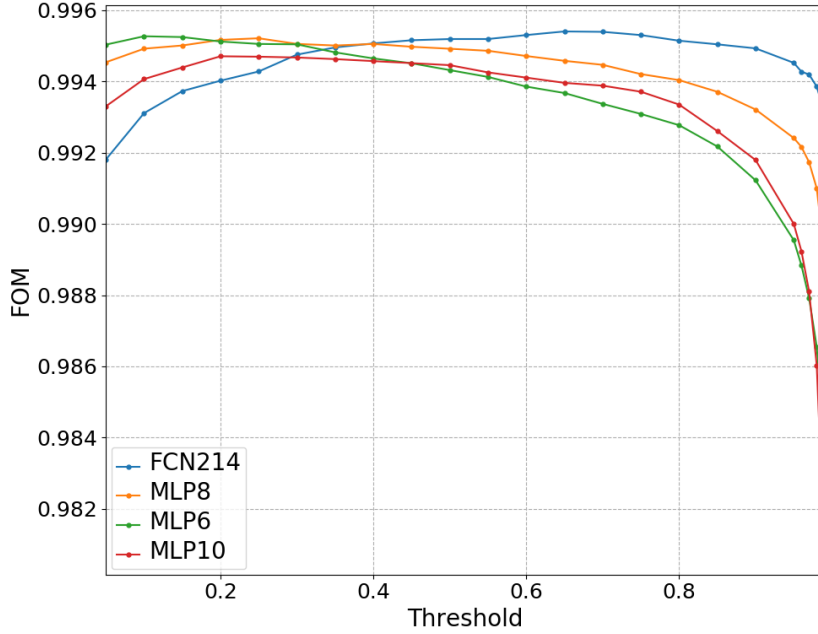


Figure 26: FOM_1 calculated for ^{214}Bi data events. Different colors represent different pulse-shape discriminators.

Secondly, another FOM was suggested. In this case, the energy range $110-240 N_{PMTs}$ is used. As shown in Figure 27, in this energy range α -events have a very distinguishable peak and β -events are calculated by subtracting α -events from the total number of events. The second FOM_2 was calculated by:

$$FOM_2 = \frac{S}{\sqrt{S+B}}, \quad (47)$$

where, S is the signal, which means (β -like) e^- events and B is background, which means (α -like) events, calculated separately for each year from 2013 until 2018, based on a fit. The signal and background events used in FOM_2 calculations are showed more precisely and time dependently in Table 4.

Year	Total	α -like events	β -like events
2012	96442.1	91973.9	4468.2
2013	21121.3	17544.6	3576.7
2014	19621.2	14955.6	4665.6
2015	15105.9	10589.9	4516.0
2016	9279.2	5750.6	3528.6
2017	10348.4	5850.5	4497.9
2018	9196.3	5009.1	4187.2

Table 4: Events in $110\text{-}240 N_{PMTs}$ energy range from 2012 until 2018. Second column shows the total number of events in this energy range, third column shows the α -like ^{210}Po events from distinguishable peak and the last column shows all β -like events.

In the next paragraphs the FOM is calculated for each discriminator separately with equations 46 and 47. The optimized threshold is selected based on the FOM_1 and FOM_2 calculations where the maximal value was chosen in the region which showed stability.

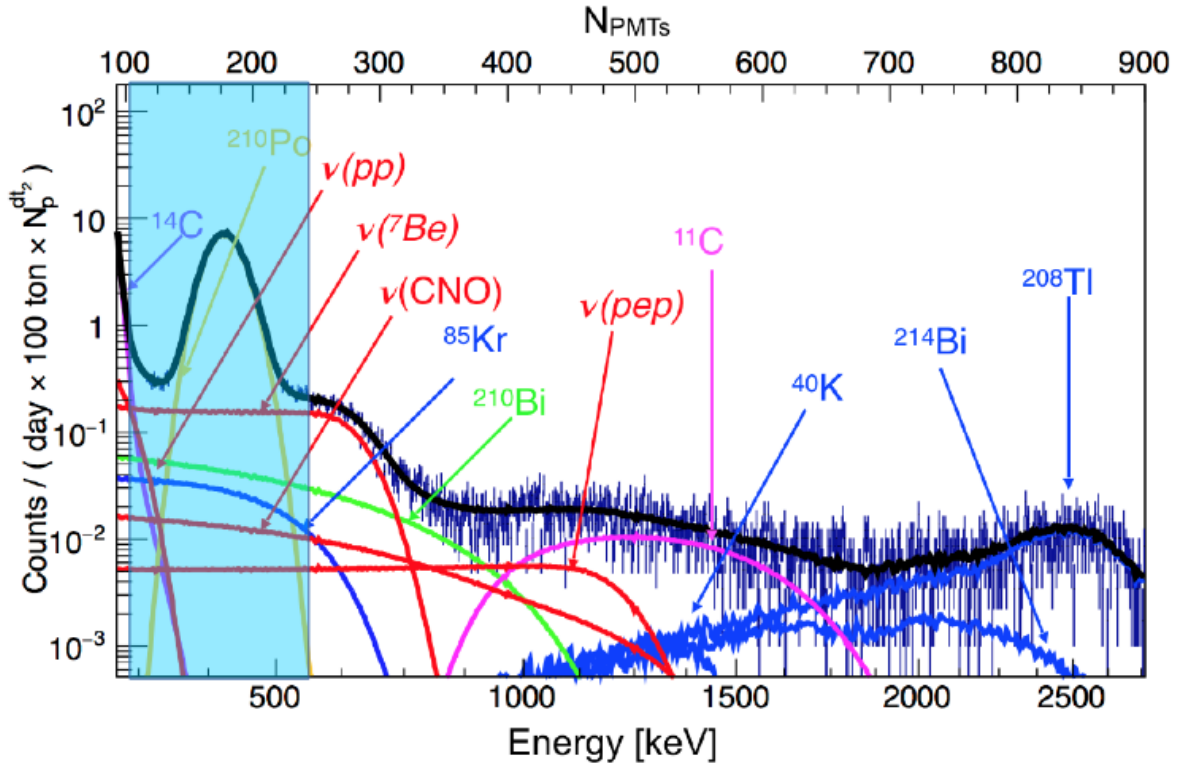
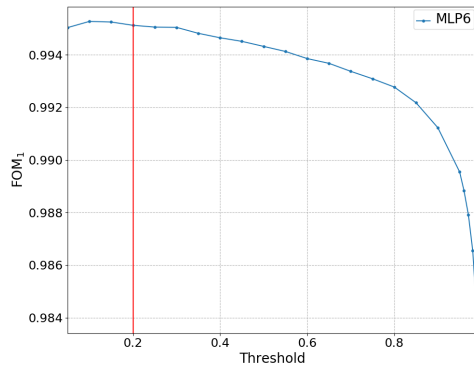
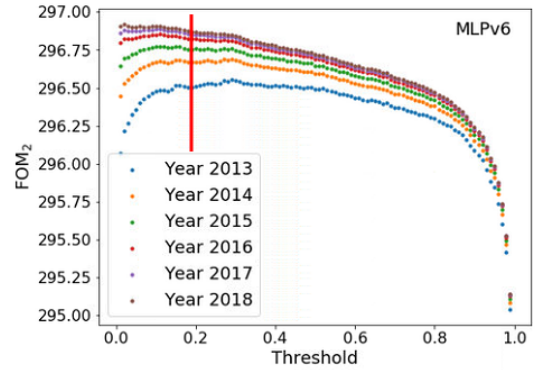


Figure 27: Energy spectrum measured with Borexino detector.

Figure of Merit for MLPv6



(a) FOM_1 calculated with equation 46

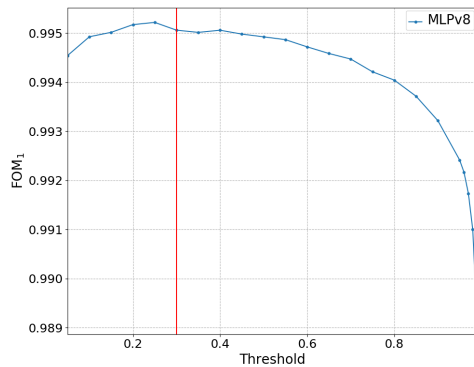


(b) FOM_2 calculated with equation 47, where different colors indicate different years between 2013 - 2018

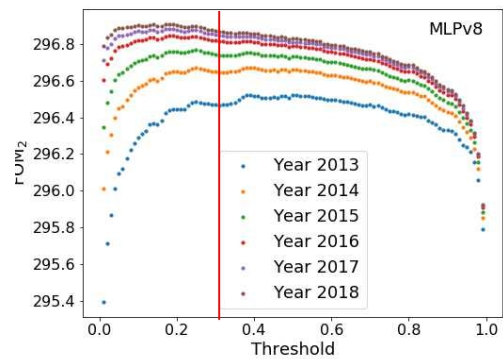
Figure 28: Figure of merit calculated with MLPv6 discriminator. The plot shows the figure of merit for different thresholds between 0 - 1.

Both figure of merit calculations in Figures 28a and 28b are being considered to find the best threshold for MLPv6, which is 0.2.

Figure of Merit for MLPv8



(a) FOM_1 calculated with equation 46

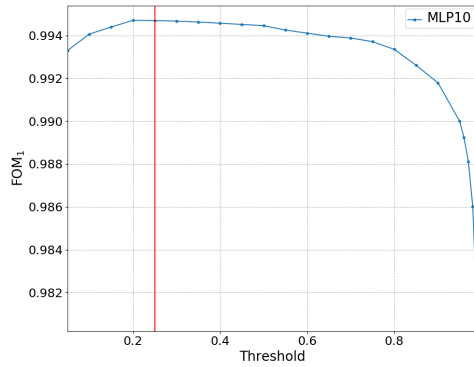


(b) FOM_2 calculated with equation 47, where different colors indicate different years between 2013 - 2018

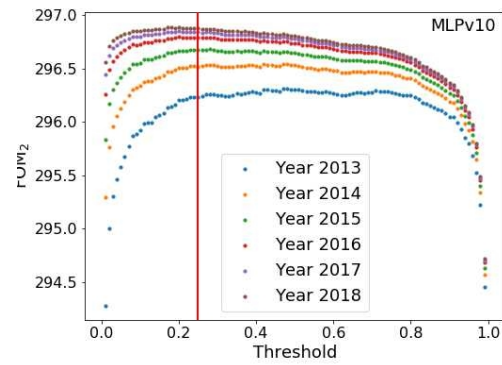
Figure 29: Figure of merit calculated with MLPv8 discriminator. The plot shows the figure of merit for different thresholds between 0 - 1.

Both figure of merit calculations in Figures 29a and 29b are being considered to find the best threshold for MLPv8, which is 0.3.

Figure of Merit for MLPv10



(a) FOM_1 calculated with equation 46

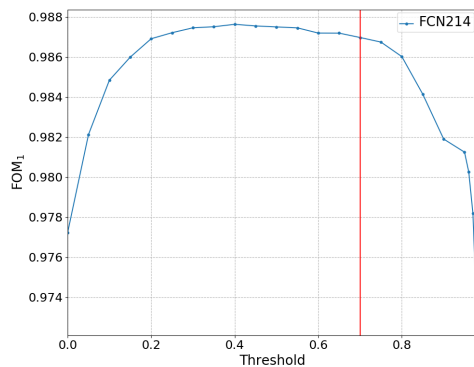


(b) FOM_2 calculated with equation 47, where different colors indicate different years between 2013 - 2018

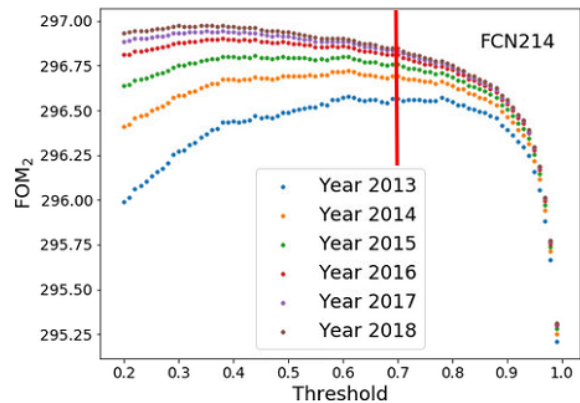
Figure 30: Figure of merit calculated with MLPv10 discriminator. The plot shows the figure of merit for different thresholds between 0 - 1.

Both figure of merit calculations in Figures 30a and 30b are being considered to find the best threshold for MLPv10, which is 0.25.

Figure of Merit for FCN214



(a) FOM_1 calculated with equation 46



(b) FOM_2 calculated with equation 47, where different colors indicate different years between 2013 - 2018

Figure 31: Figure of merit calculated for FCN discriminator, calculated with FCN214. The plot shows the figure of merit for different thresholds between 0.05 - 1.

Both figure of merit calculations in Figures 31a and 31b are being considered to find the best threshold for FCN214, which is 0.7.

Figure of Merit for FCN210

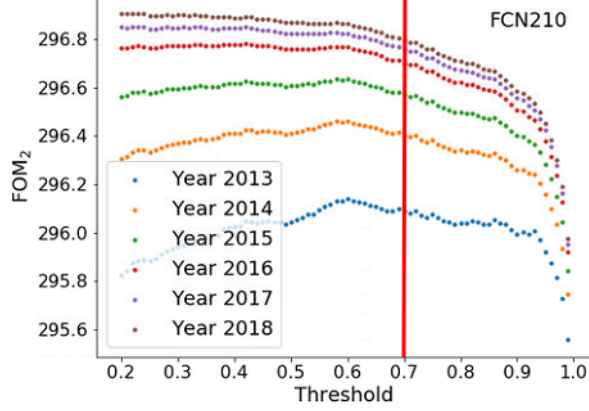


Figure 32: FOM_2 calculated with equation 47, where different colors indicate different years between 2013 - 2018. Figure of merit calculated for FCN210 discriminator, calculated with FCN210. The plot shows the figure of merit for different thresholds between 0 - 1.

FOM_2 calculations are shown in Figure 32 to find the best threshold for FCN210, which is 0.7.

5.2.2 Optimized thresholds

The optimized threshold values were calculated for each discriminator considering both figure of merits calculated with:

- FOM_1 calculated with equation 46
- FOM_2 calculated with equation 47

Optimized cut with corresponding β -efficiency ε_β and α -leakage L_α for each discriminator can be found in the Table 5.

Variable	Threshold cut	ε_β	L_α
MLPv6	> 0.2	$(99.6385 \pm 0.3355)\%$	$(0.0633 \pm 0.0085)\%$
MLPv8	> 0.3	$(99.6475 \pm 0.3355)\%$	$(0.0712 \pm 0.0090)\%$
MLPv10	> 0.25	$(99.6972 \pm 0.3356)\%$	$(0.1141 \pm 0.0114)\%$
FCN214	> 0.7	$(99.6882 \pm 0.3356)\%$	$(0.0746 \pm 0.0092)\%$
FCN210	> 0.7	$(99.6874 \pm 0.3356)\%$	$(0.0789 \pm 0.0091)\%$

Table 5: Optimized threshold cut value for each discriminator calculated with ^{214}Bi data events with corresponding β -efficiency and α -leakage values.

In conclusion the efficiency is high with all 5 variables. The α -leakage is lowest with MLPv6, MLPv8, FCN214, and FCN210 discriminators.

The calculations were also done for Gatti discriminator, but since it did not give better results, they are not represented here.

5.3 ^{214}Bi and ^{214}Po data and MC

The main goal of this work is to study ^{210}Bi homogeneity in the whole *pep* FV in time span of several years, because Borexino has lost about 10% of all PMTs until now. The performance of α/β discriminators is expected to be time and position dependent and based only on ^{214}Bi and ^{214}Po WE data, it is thus not possible to study it. Therefore, first step is to compare the ^{214}Bi and ^{214}Po MC ability to simulate α/β discriminators, in case when we have the data of pure samples of ^{214}Bi and ^{214}Po data, then the next step is studying the performance of ^{210}Bi and ^{210}Po MC samples only, produced good agreement between data and MC. In addition, an attempt to tune the discriminators on homogenous ^{210}Bi and ^{210}Po MC has been done (FCN210). Ideally one should study the performance of the discriminators on events different from those on which the tuning has been done.

5.3.1 Efficiency and leakage

Figure 33 shows the distribution of ^{214}Bi MC events, as a blue line and normalized ^{214}Bi data events as a red line with different discriminators (same distributions for ^{214}Po data and MC events can be found in Appendix A).

To attain further conclusions of different discriminators the efficiencies and leakages (introduced in Chapter 5.2) are going to be calculated in the whole detector and separately for northern and southern parts of the detector to check the uniformity.

The total efficiency and leakage calculations are presented in the Tables 6 and 7, respectively. First important point to notice in both of the tables is that the efficiency and leakage improved with optimized threshold cut for all discriminators except Gatti parameter calculated with data and MC. Second point to look at is the uniformity in the detector, when comparing the efficiency of WE data and looking at α -efficiency ε_α it can be seen, that the difference between north and south is $< 0.5\%$ (biggest difference with FCN210 discriminator is 0.4%), and looking at β -efficiency ε_β the difference between north and south is $\sim 1\%$, being the lowest with FCN210 discriminator (0.86%). Comparing the efficiency differences of WE MC, it can be seen that the differences for ε_α and ε_β between north and south is $< 1\%$ (except for FCN210, when ε_α has a $\sim 2\%$ difference between north and south). When comparing the leakage of WE data and looking at α -leakage L_α is $\sim 1\%$ with all the discriminators and β -leakage L_β is even smaller. In case of WE MC events the difference between north and south with all three discriminators for L_α and $L_\beta < 1\%$. Third point to look is the uniformity between WE data and MC results, ε_α and ε_β are giving both very similar results with $< 1\%$ difference (with an exception for FCN210 for ε_α , where the difference is 4.2% and FCN214 for ε_β , where the difference is $\sim 2\%$), best results with MLPv8 discriminator. When looking at leakage, data and MC also differs only $< 1\%$, except for L_α with FCN214 discriminator, where the difference is almost 2% and L_β with FCN210 discriminator when the difference is more than 4% .

In conclusion, when looking at ^{214}Bi - ^{214}Po events the two best discriminators are MLPv8 and FCN214, with optimized threshold cut brought out in Table 5.

DATA			MC		
Total					
Variable	ε_α (%)		ε_β (%)		ε_β (%)
	Old	Optimized	Old	Optimized	
MLPv6	(99.90±0.02)	(99.94±0.02)	(99.00±0.07)	(99.64±0.04)	
MLPv8	(99.86±0.03)	(99.93±0.02)	(99.31±0.06)	(99.65±0.04)	(99.00±0.01)
MLPv10	(99.78±0.03)	(99.89±0.02)	(99.10±0.06)	(99.70±0.04)	
FCN214	(99.69±0.04)	(99.93±0.02)	(99.54±0.05)	(99.69±0.04)	(96.43±0.03)
FCN210	(86.79±0.21)	(97.36±0.11)	(99.14±0.09)	(99.37±0.07)	(93.16±0.03)
Gatti	(99.73±0.03)	(99.82±0.03)	(99.75±0.03)	(99.71±0.04)	
North					
Variable	ε_α (%)		ε_β (%)		ε_β (%)
	Old	Optimized	Old	Optimized	
MLPv6	(99.89±0.03)	(99.93±0.02)	(99.23±0.08)	(99.73±0.05)	
MLPv8	(99.85±0.03)	(99.92±0.02)	(99.50±0.06)	(99.74±0.05)	(99.22±0.02)
MLPv10	(99.77±0.04)	(99.87±0.03)	(99.35±0.07)	(99.80±0.04)	
FCN214	(99.63±0.05)	(99.91±0.03)	(99.70±0.05)	(99.81±0.04)	(96.60±0.03)
FCN210	(85.84±0.29)	(97.13±0.15)	(99.20±0.11)	(99.42±0.08)	(71.69±0.09)
Gatti	(99.70±0.05)	(99.81±0.04)	(99.83±0.04)	(99.81±0.04)	
South					
Variable	ε_α (%)		ε_β (%)		ε_β (%)
	Old	Optimized	Old	Optimized	
MLPv6	(99.91±0.06)	(99.93±0.05)	(96.94±0.34)	(98.64±0.23)	
MLPv8	(99.88±0.07)	(99.91±0.06)	(97.64±0.30)	(98.65±0.23)	(97.19±0.07)
MLPv10	(99.70±0.11)	(99.85±0.08)	(96.87±0.34)	(98.73±0.22)	
FCN214	(99.74±0.10)	(99.92±0.06)	(98.49±0.24)	(98.85±0.21)	(94.75±0.09)
FCN210	(87.84±0.61)	(97.53±0.31)	(98.24±0.35)	(98.56±0.27)	(76.92±0.10)
Gatti	(99.70±0.11)	(99.82±0.08)	(99.03±0.19)	(98.93±0.20)	

Table 6: Efficiency calculations with ^{214}Bi - ^{214}Po data and MC under corresponding column, as shown in the first row. α and β efficiencies (ε_α and ε_β respectively) with old and optimized threshold cuts are presented in different columns.

DATA				MC				
Total								
Variable	L_α (%)		L_β (%)		L_α (%)		L_β (%)	
	Old	Optimized	Old	Optimized	Old	Optimized	Old	Optimized
MLPv6	(1.00 ± 0.03)	(0.36 ± 0.02)	(0.10 ± 0.01)	(0.06 ± 0.01)				
MLPv8	(0.69 ± 0.03)	(0.35 ± 0.02)	(0.14 ± 0.01)	(0.07 ± 0.01)	(1.00 ± 0.01)	(0.32 ± 0.01)	(1.15 ± 0.01)	(0.61 ± 0.01)
MLPv10	(0.90 ± 0.03)	(0.30 ± 0.02)	(0.22 ± 0.02)	(0.11 ± 0.01)				
FCN214	(0.46 ± 0.02)	(0.31 ± 0.02)	(0.31 ± 0.02)	(0.07 ± 0.01)	(3.57 ± 0.01)	(2.27 ± 0.01)	(2.98 ± 0.01)	(0.64 ± 0.01)
FCN210	(0.86 ± 0.03)	(0.64 ± 0.03)	(13.21 ± 0.03)	(2.64 ± 0.01)	(1.86 ± 0.03)	(1.27 ± 0.01)	(25.31 ± 0.04)	(6.84 ± 0.02)
Gatti	(0.25 ± 0.02)	(0.29 ± 0.02)	(0.27 ± 0.02)	(0.17 ± 0.01)				
North								
Variable	L_α (%)		L_β (%)		L_α (%)		L_β (%)	
	Old	Optimized	Old	Optimized	Old	Optimized	Old	Optimized
MLPv6	(0.77 ± 0.04)	(0.27 ± 0.02)	(0.11 ± 0.02)	(0.07 ± 0.01)				
MLPv8	(0.51 ± 0.03)	(0.26 ± 0.02)	(0.15 ± 0.02)	(0.08 ± 0.01)	(0.79 ± 0.01)	(0.25 ± 0.01)	(1.36 ± 0.01)	(0.71 ± 0.01)
MLPv10	(0.65 ± 0.04)	(0.20 ± 0.02)	(0.23 ± 0.02)	(0.13 ± 0.02)				
FCN214	(0.31 ± 0.03)	(0.20 ± 0.02)	(0.37 ± 0.03)	(0.09 ± 0.01)	(3.40 ± 0.02)	(2.24 ± 0.01)	(3.51 ± 0.02)	(0.77 ± 0.01)
FCN210	(0.80 ± 0.04)	(0.58 ± 0.03)	(14.16 ± 0.05)	(2.87 ± 0.02)	(1.90 ± 0.03)	(1.30 ± 0.01)	(28.31 ± 0.07)	(8.05 ± 0.04)
Gatti	(0.17 ± 0.02)	(0.20 ± 0.02)	(0.30 ± 0.02)	(0.19 ± 0.02)				
South								
Variable	L_α (%)		L_β (%)		L_α (%)		L_β (%)	
	Old	Optimized	Old	Optimized	Old	Optimized	Old	Optimized
MLPv6	(3.06 ± 0.18)	(1.36 ± 0.12)	(0.09 ± 0.03)	(0.07 ± 0.03)				
MLPv8	(2.36 ± 0.15)	(1.35 ± 0.12)	(0.12 ± 0.03)	(0.09 ± 0.03)	(2.81 ± 0.04)	(0.88 ± 0.04)	(0.95 ± 0.01)	(0.50 ± 0.01)
MLPv10	(3.13 ± 0.18)	(1.27 ± 0.11)	(0.31 ± 0.06)	(0.15 ± 0.04)				
FCN214	(1.51 ± 0.12)	(1.15 ± 0.11)	(0.26 ± 0.05)	(0.08 ± 0.03)	(5.25 ± 0.05)	(3.05 ± 0.04)	(2.70 ± 0.02)	(0.58 ± 0.01)
FCN210	(1.77 ± 0.13)	(1.44 ± 0.12)	(12.16 ± 0.10)	(2.48 ± 0.05)	(2.39 ± 0.03)	(1.66 ± 0.03)	(23.09 ± 0.07)	(5.99 ± 0.03)
Gatti	(0.97 ± 0.10)	(1.08 ± 0.10)	(0.30 ± 0.05)	(0.18 ± 0.04)				

Table 7: Leakage calculations with ^{214}Bi - ^{214}Po data and MC under corresponding column, as shown in the first row. α and β leakages (L_α and L_β respectively) with old and optimized threshold cuts are presented in different columns.

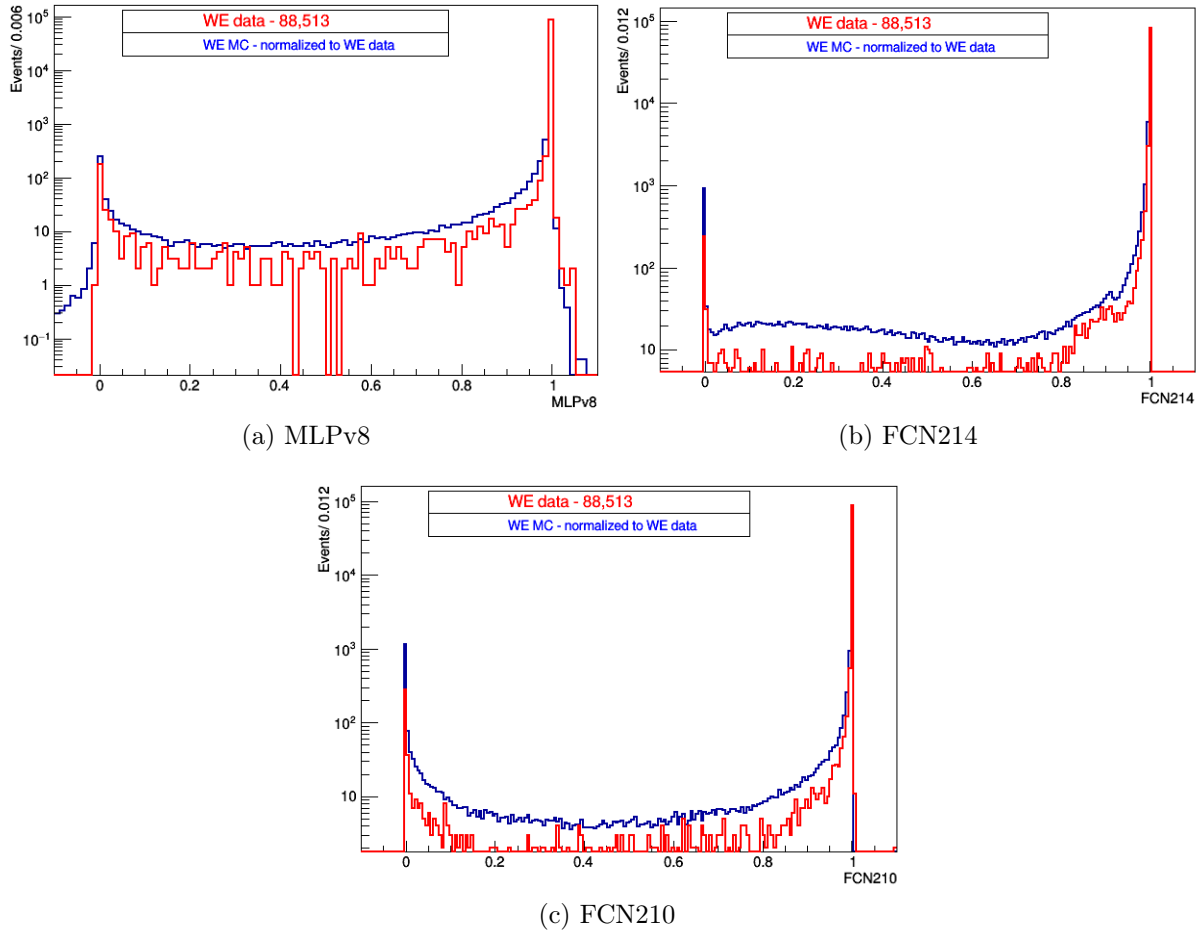
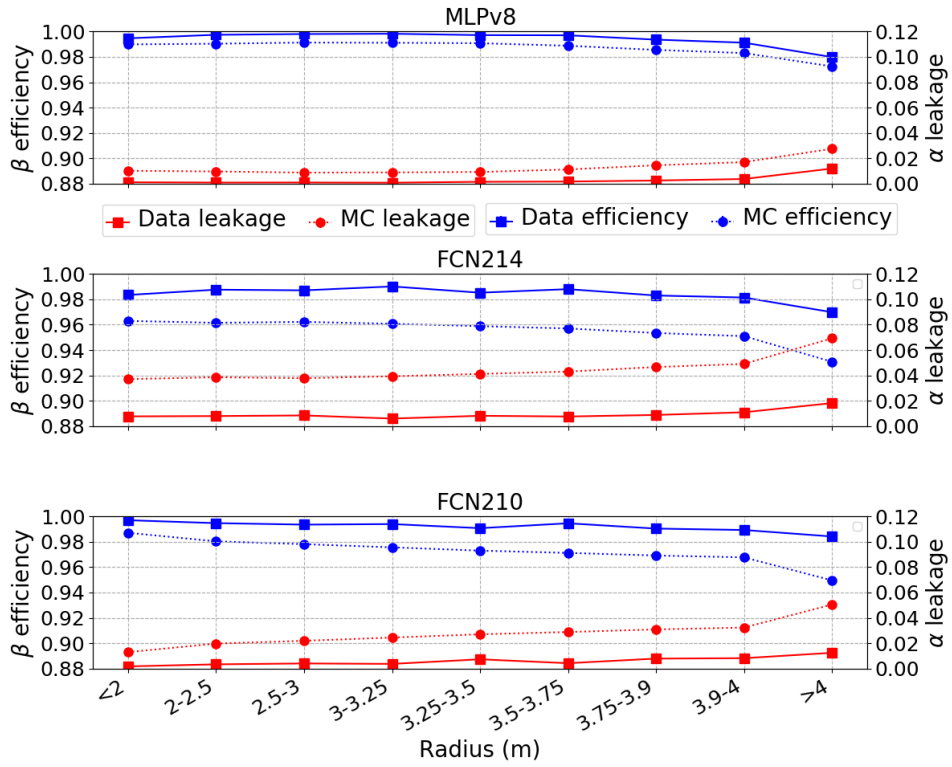


Figure 33: Distribution of ^{214}Bi with data (red line) and MC (blue line) with different pulse-shape discriminators.

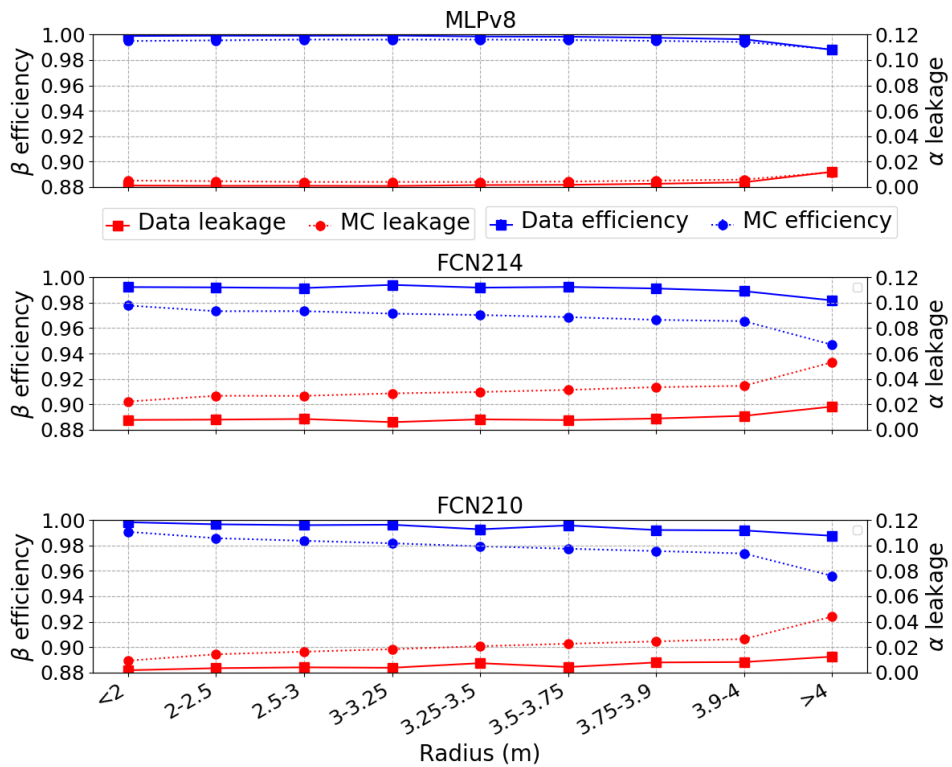
5.3.2 Radial dependency

Next the efficiency ε_β and leakage L_α dependency on the position in the detector is estimated.

In the Figures 34a and 34b the efficiency ε_β and leakage L_α dependance on radius is shown, calculated with old and optimized threshold cut respectively. The efficiency ε_β is much higher and more stable with optimized threshold cut with all discriminators, but α -leakage L_α is decreasing with FCN214 and FCN210 especially with MC events.



(a) Old threshold cut



(b) Optimized threshold cut

Figure 34: Efficiency ε_β and leakage L_α vs radius for ^{214}Bi calculated with data (solid lines) and MC (dashed lines) events. Blue line represents the β -efficiency and red line the α -leakage.

In radial dependancy plots one can see how the efficiencies ε_β are much higher and stable with optimized threshold cuts, introduced in Section 5.2. When looking at the MLPv8 discriminator, it has the best results, it can be seen that even if the results with old threshold cut are good, they are much better and more stable with optimized threshold cut. Especially in the outer region of the detector with old cut, the efficiency ε_β started dropping and leakage L_α increasing around 3.75 m, then with optimized cut it can be only seen with radius > 4 m.

Also the efficiency ε_β is in agreement and similar for data and MC. For example looking at MLPv8 results, it can be seen that MC efficiency ε_β is always lower and leakage higher, but it behaves very similarly (efficiency starts to drop and leakage L_α starts to increase at same radius as for data). It was tried to use smaller threshold cut for all variables with MC to increase the efficiency, but the efficiency did not rise no matter how low the threshold cut.

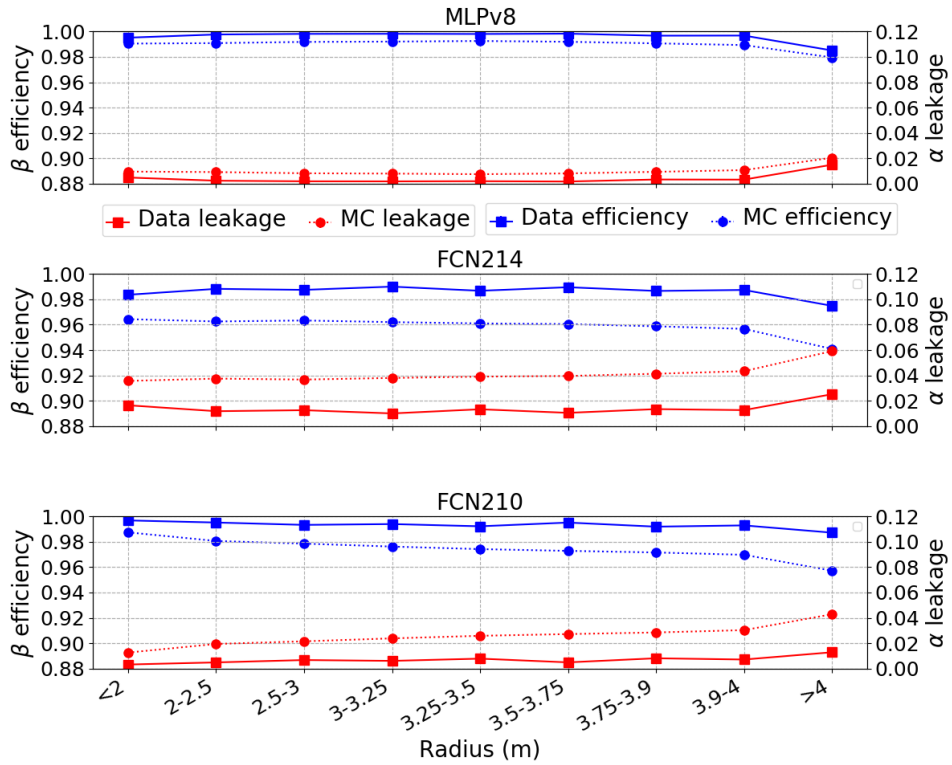
Now we discuss the same radial dependency plots but separately for the north ($z > 0$) and south ($z < 0$) regions of the detector.

North and south with data and MC

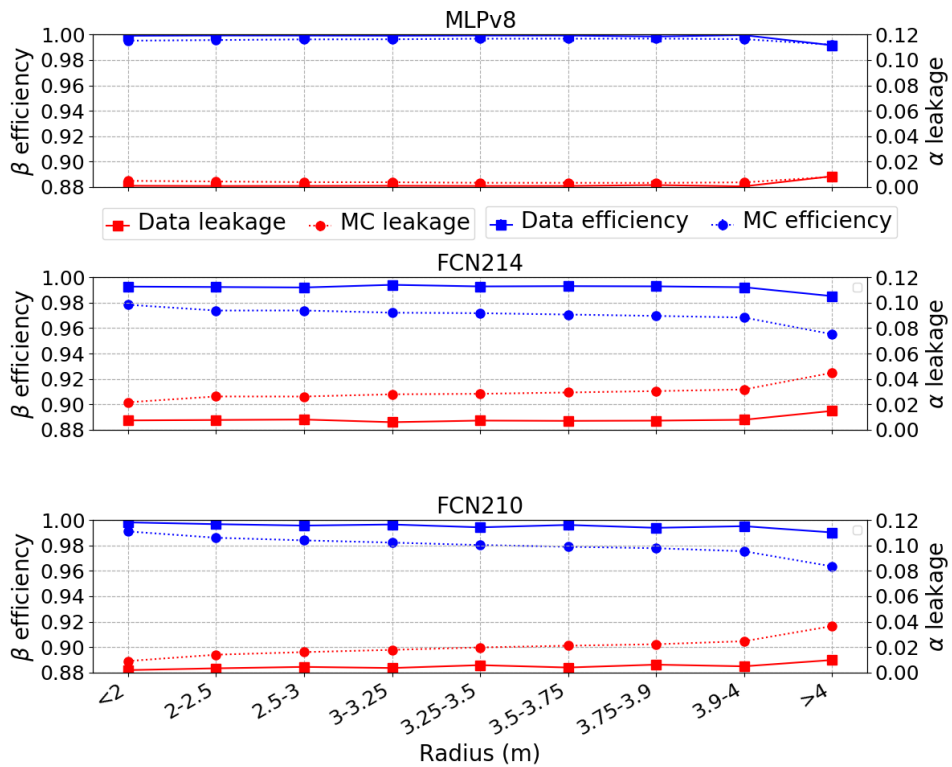
In Figures 35a and 35b the efficiency ε_β and leakage L_α dependency on radius for MLPv8, FCN214, and FCN210, with old cut and with optimized cuts respectively are shown. The efficiency ε_β is much more stable and increasing with optimized threshold cut and leakage L_α is staying almost the same for all discriminators.

When looking at the south area of the detector, it can be seen that the efficiency ε_β and leakage L_α versus radius with MLPv8, FCN214, and FCN210 discriminators are much more stable with optimized threshold cuts, as shown in Figures 36a and 36b.

Comparing the difference between north and south, one can see that the efficiency ε_β is always higher and leakage lower in the northern part of the detector especially with old threshold cut, but small difference (no more than 2%) can also be seen with optimized threshold cuts. Definetely the best results are with MLPv8 discriminator, efficiency ε_β is the highest and leakage L_α lowest, and the difference between north and south is the smallest.

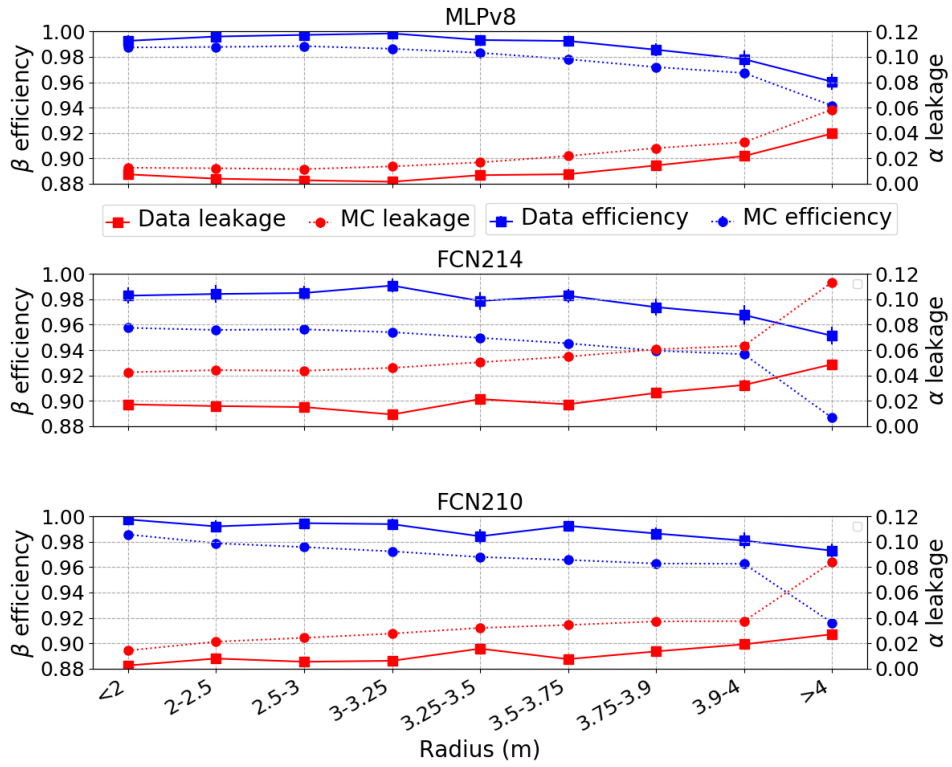


(a) Old threshold cut

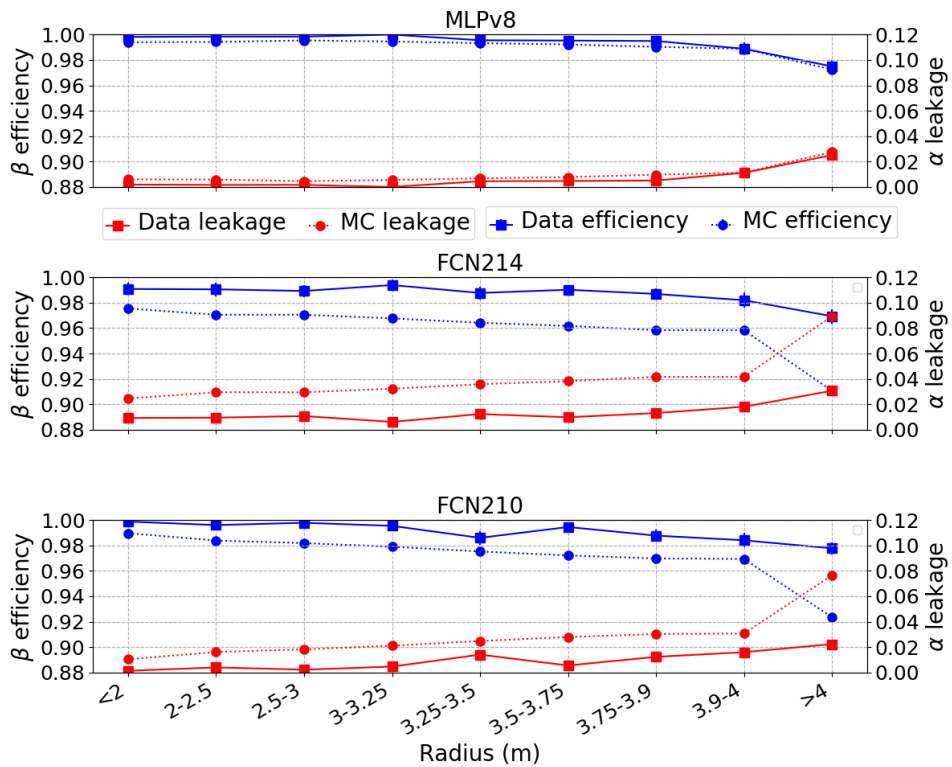


(b) Optimized threshold cut

Figure 35: Efficiency ε_β and leakage L_α vs radius for ^{214}Bi calculated with data (solid lines) and MC (dashed lines) events in the northern ($z > 0$) part of the detector. Blue lines represents the β -efficiency and red lines the α -leakage.



(a) With old cut



(b) With new cut

Figure 36: Efficiency ε_β and leakage L_α vs radius for ^{214}Bi calculated with data (solid lines) and MC (dashed lines) events in the southern ($z < 0$) part of the detector. Blue line represents the β -efficiency and red line the α -leakage.

5.4 ^{210}Bi and ^{210}Po MC

5.4.1 Total efficiency and leakage

The total efficiency ε_β and leakage L_α calculations were made for MLPv8, FCN214, and FCN210 with ^{210}Bi and ^{210}Po MC events separately and the distributions of these discriminators can be found in Figure 37 (^{210}Po MC events distributions with different discriminators can be found in Appendix B).

Conditions used:

- energy cut: 130 – 300 NPMTs_dt1
- *pep* Fiducial Volume (FV): $r < 2.8\text{ m}$, $-1.8\text{ m} < z < 2.2\text{ m}$

In Table 8 the efficiency and leakage for ^{210}Bi and ^{210}Po MC events are calculated. The efficiency increases and leakage decreases with new threshold cut with every discriminator. The difference between north and south for efficiency and leakage is $< 5\%$. When looking at the ^{210}Po MC events, the best variable would be FCN214 with highest efficiency ε_α and lowest L_β and looking at the ^{210}Bi MC events the best variable would be FCN210 with highest efficiency ε_β (at least 4% higher than other variables) and L_α lowest leakage (at least 4% lower than other variables).

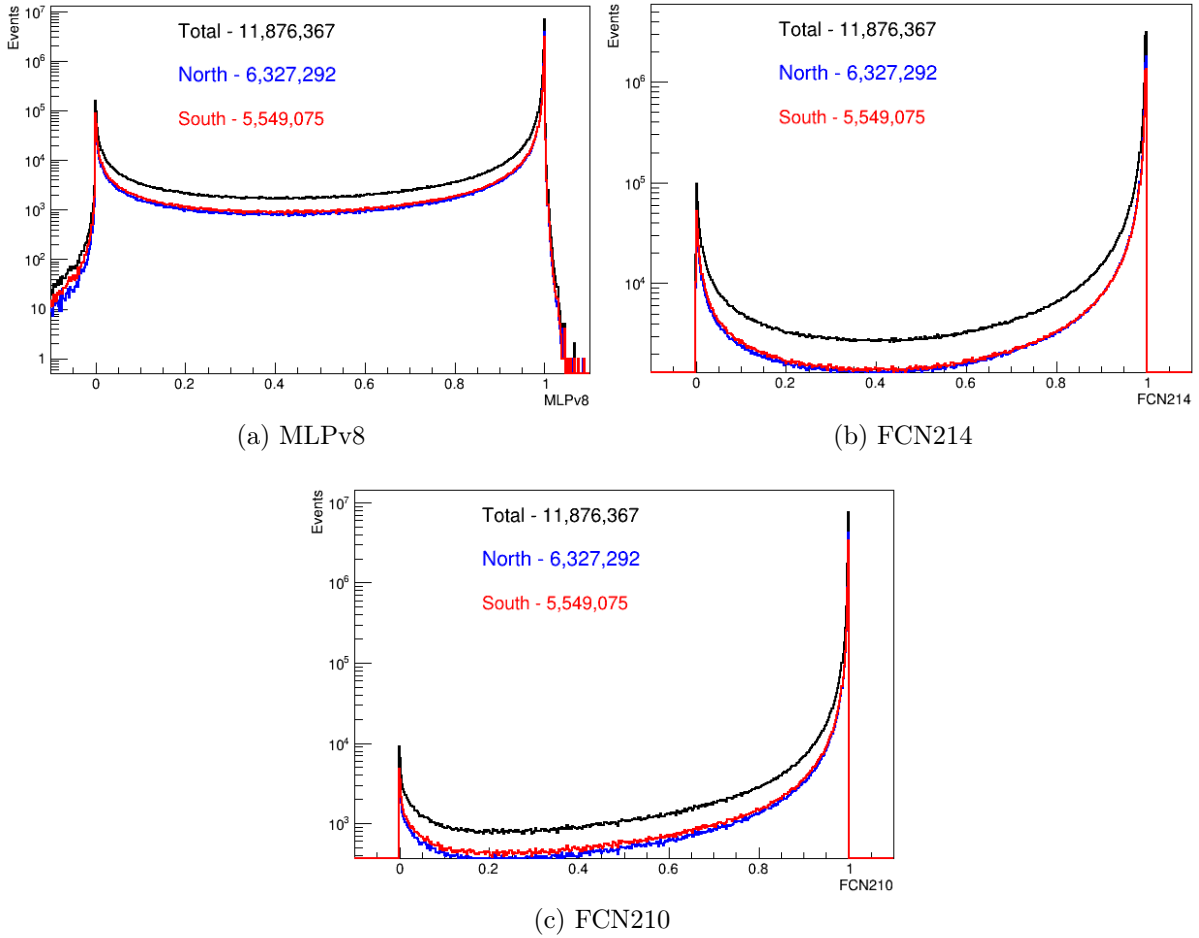


Figure 37: Distribution of ^{210}Bi MC events with different discriminators. Black line shows the total events within selected energy region and *pep* FV, blue and red lines show the events in northern ($z > 0$) and southern ($z < 0$) part of the detector respectively.

		Efficiency				Leakage				
		Total								
Variable	ε_α (%)	Optimized	Old	ε_β (%)	Optimized	Old	L_α (%)	Optimized	Old	L_β (%)
MLPv8	(97.04±0.01)	(98.15±0.01)	(86.50±0.02)	(93.59±0.01)	(93.59±0.01)	(13.51±0.01)	(6.42 ± 0.01)	(2.96 ± 0.01)	(1.85 ± 0.01)	
FCN214	(65.34±0.02)	(99.09±0.01)	(80.06±0.02)	(88.86±0.02)	(19.94±0.01)	(11.14±0.01)	(34.67±0.02)	(0.91 ± 0.01)		
FCN210	(78.16±0.02)	(93.80±0.01)	(93.59±0.02)	(97.40±0.02)	(6.41 ± 0.01)	(2.61 ± 0.01)	(21.75±0.01)	(1.24 ± 0.01)		
North										
Variable	ε_α (%)	Optimized	Old	ε_β (%)	Optimized	Old	L_α (%)	Optimized	Old	L_β (%)
MLPv8	(96.62±0.02)	(97.87±0.01)	(89.43±0.03)	(95.16±0.02)	(10.57±0.02)	(4.84 ± 0.01)	(3.38 ± 0.01)	(2.13 ± 0.01)		
FCN214	(65.82±0.04)	(98.99±0.01)	(83.86±0.03)	(91.36±0.03)	(16.14±0.02)	(8.64 ± 0.02)	(34.18±0.03)	(1.01 ± 0.01)		
FCN210	(75.59±0.04)	(92.75±0.03)	(95.18±0.03)	(98.08±0.03)	(4.82 ± 0.01)	(1.92 ± 0.01)	(24.21±0.03)	(1.50 ± 0.01)		
South										
Variable	ε_α (%)	Optimized	Old	ε_β (%)	Optimized	Old	L_α (%)	Optimized	Old	L_β (%)
MLPv8	(97.39±0.02)	(98.38±0.01)	(83.19±0.04)	(91.75±0.03)	(16.81±0.03)	(8.25 ± 0.02)	(2.61 ± 0.01)	(1.62 ± 0.01)		
FCN214	(64.40±0.04)	(99.08±0.01)	(77.20±0.04)	(86.93±0.04)	(22.80±0.03)	(13.07±0.02)	(35.60±0.04)	(0.92 ± 0.01)		
FCN210	(79.63±0.04)	(94.35±0.03)	(92.34±0.04)	(96.81±0.04)	(7.66 ± 0.02)	(3.19 ± 0.01)	(20.28±0.03)	(1.11 ± 0.01)		

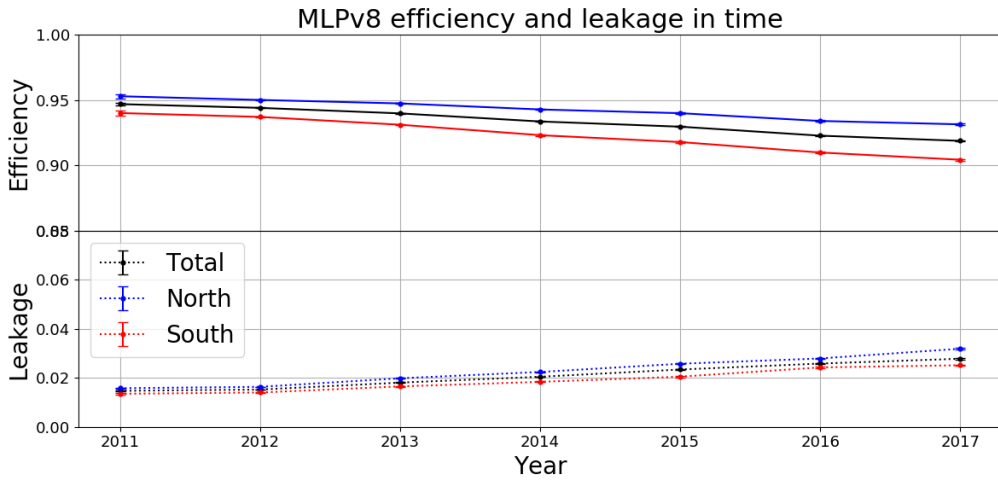
Table 8: Efficiency and leakage calculations for ^{210}Bi and ^{210}Po MC events.

5.4.2 Time dependency

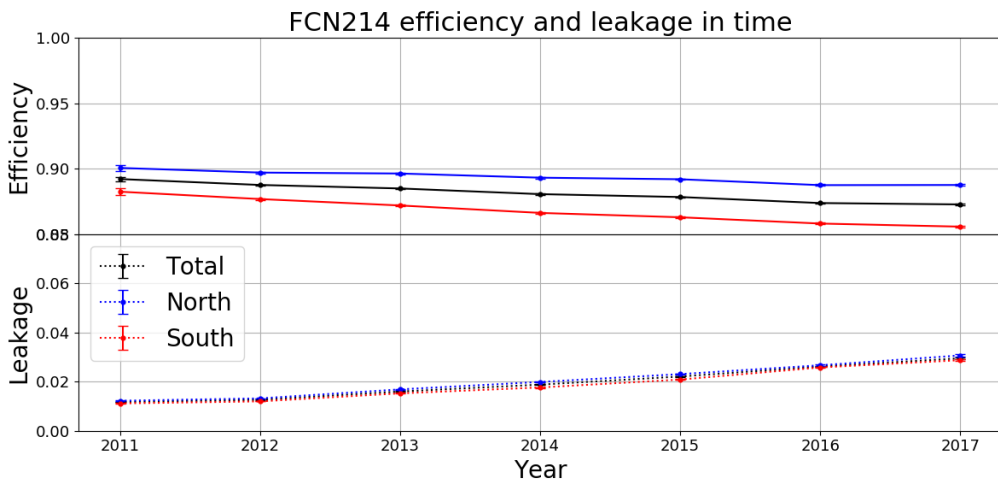
In Figure 38 efficiency ε_β and leakage L_α are distributed for ^{210}Bi MC events year by year (for ^{210}Po MC events the distributions can be found in Appendix C), starting from 2011 and ending with 2017. The number of events each year can be found in Table 9. From the figures it can be seen that efficiency ε_β is dropping and leakage L_α is increasing by every year with all discriminators.

Year	Total	North	South
2012	2,380,796	1,266,622	1,114,172
2013	1,843,277	981,319	861,958
2014	2,263,323	1,206,010	1,057,313
2015	2,194,452	1,168,620	1,025,632
2016	1,870,579	998,072	872,507
2017	1,323,940	706,449	617,491

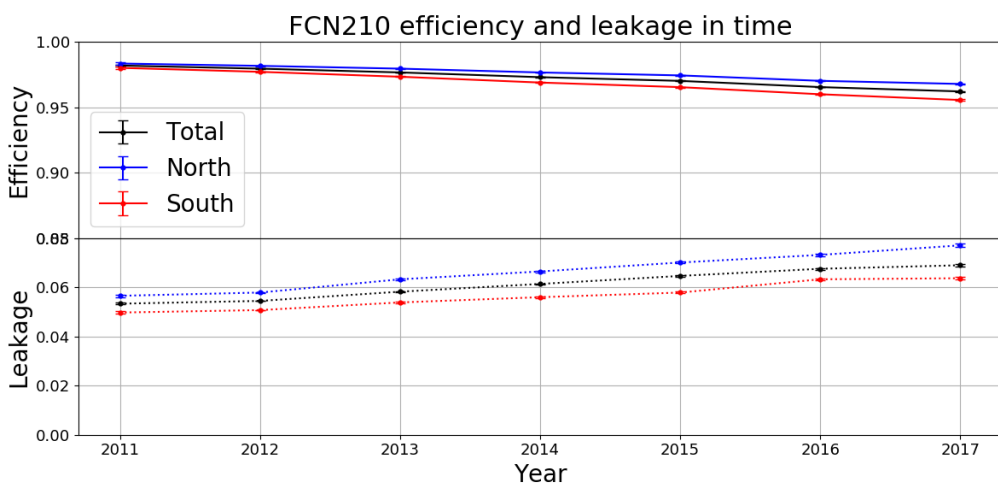
Table 9: ^{210}Bi MC values year by year in the whole *pep* FV and separately in the northern part ($z > 0$) and southern part ($z < 0$) of the detector.



(a) MLPv8



(b) FCN214



(c) FCN210

Figure 38: Time dependency of ^{210}Bi MC events with all discriminators. Different colors represent position in detector, black line represents the whole detector, blue and red the northern ($z > 0$) and southern ($z < 0$) parts of the detector respectively.

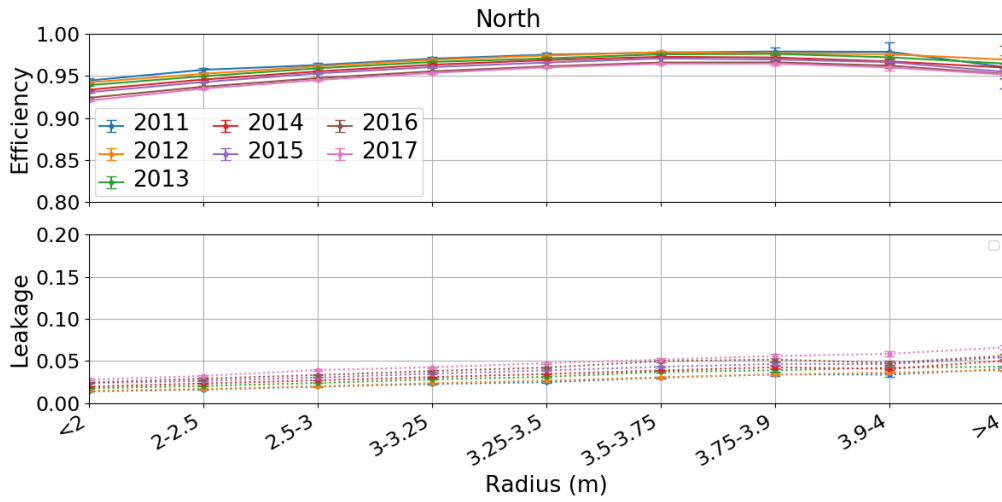
5.4.3 Radial dependency

In Figures 39 - 41 the efficiency ε_β and leakage L_α dependency on radius are plotted year by year in different parts of the detector with ^{210}Bi MC events (same plots for ^{210}Po MC events can be found in Appendix D) with MLPv8, FCN214 and FCN210 discriminators.

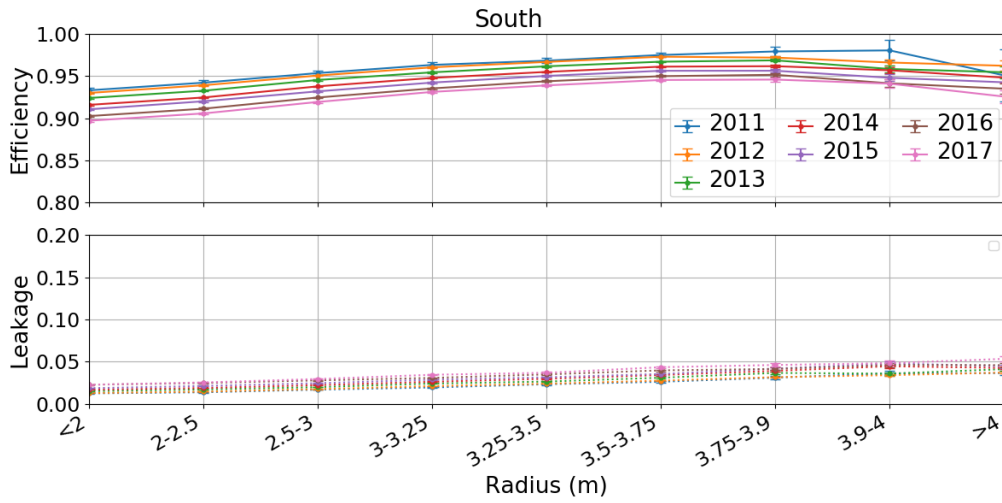
The highest and most stable β -efficiency ε_β values are with FCN210 discriminator (as shown in Figure 41), but also α -leakage is high and increasing with radius with this discriminator. When for other discriminators (MLPv8 in Figure 39 and FCN214 in Figure 40) the efficiency ε_β has quite low values in the smaller radius and then starts to increase with radius, getting its highest peak at 3.9 m and then starts to drop, then the FCN210 discriminator only has a slightly smaller efficiency ε_β values in the middle of the detector, but other than that, the efficiency ε_β is very high, almost near 1. For the leakage L_α on the other hand the FCN210 discriminator has the highest values, but MLPv8 and FCN214 have both quite low α -leakage L_α throughout the whole IV.

It can be seen how the efficiency ε_β is quite in agreement between northern ($z > 0$) and southern ($z < 0$) parts of the detector. The efficiency ε_β has a little smaller values with every discriminator, but the difference is not high. The leakage L_α on the other hand has always lower values in the southern part of the detector, but also here, the difference is almost negligible.

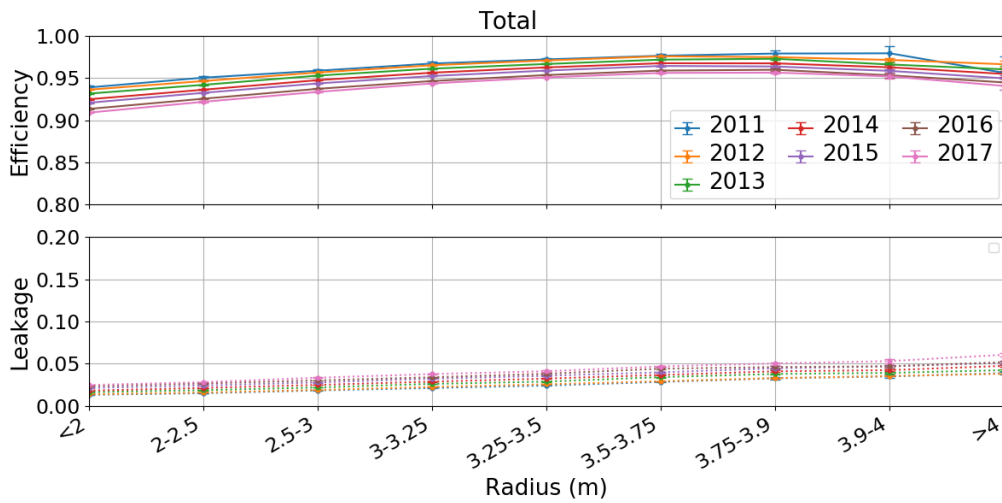
The efficiency ε_β and leakage L_α calculations are done separately for every year from 2011 until 2017. In early years the efficiency values are highest and leakage L_α values lowest then efficiency ε_β starts to drop with every year and leakage starts to increase with every year with every discriminator.



(a) North

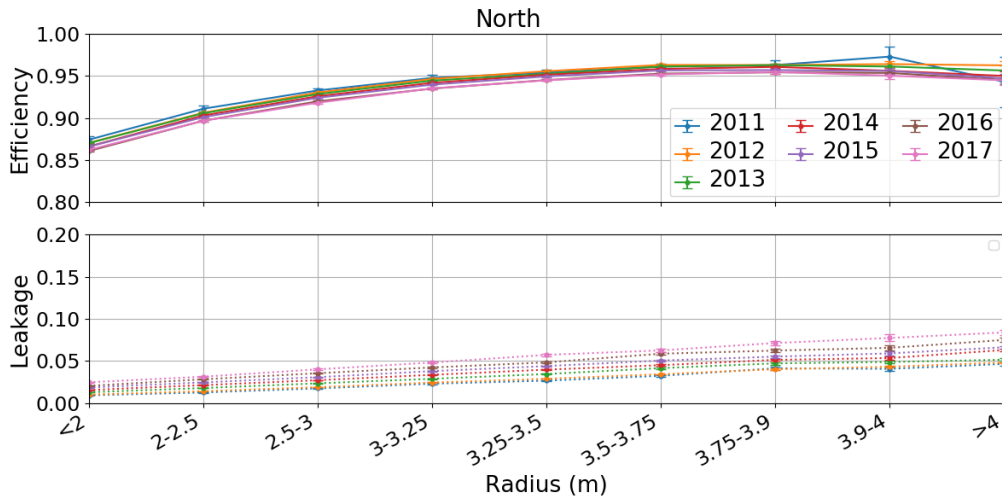


(b) South

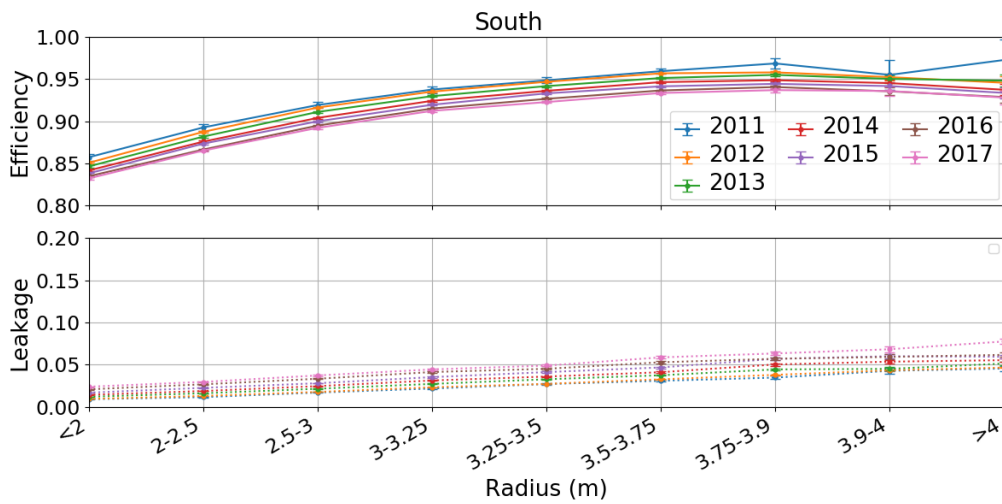


(c) Total

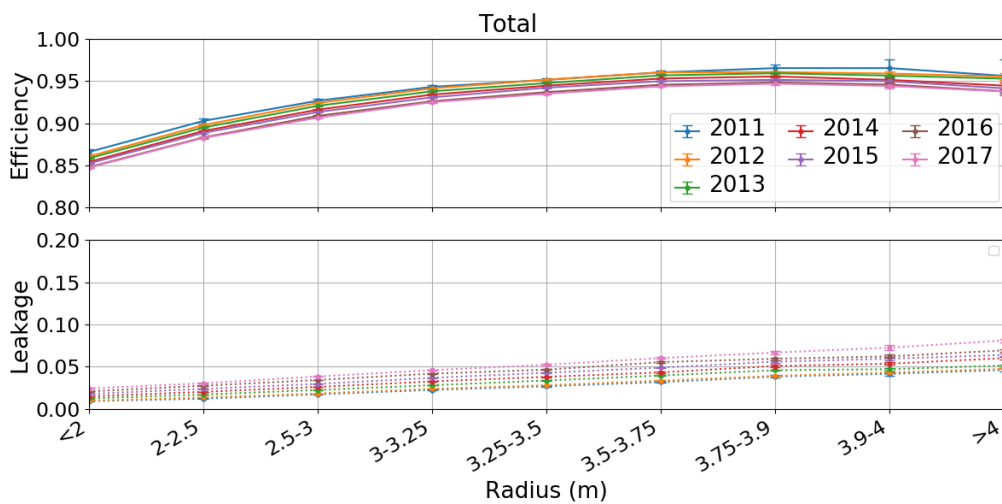
Figure 39: ^{210}Bi MC events efficiency ε_β and leakage L_α radial dependency year by year calculated with MLPv8 discriminator in different parts of the detector. Colors represent different years.



(a) North

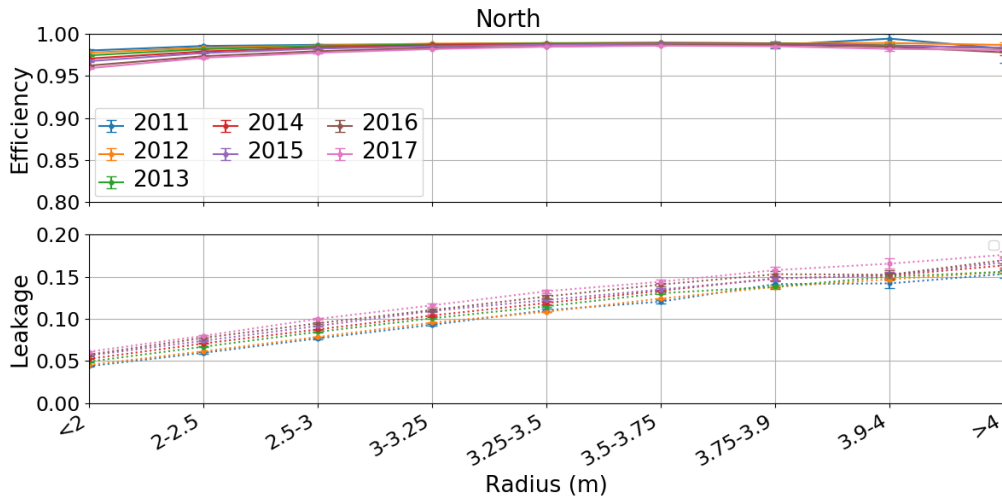


(b) South

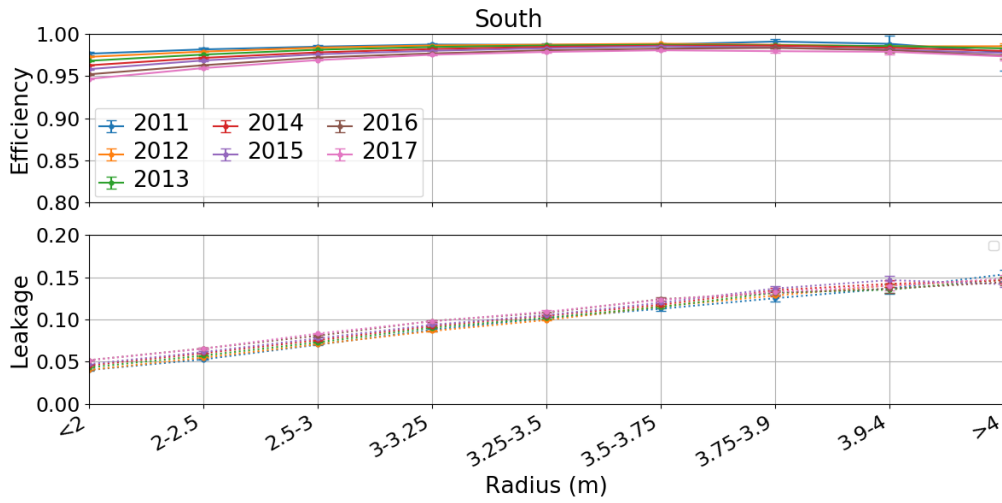


(c) Total

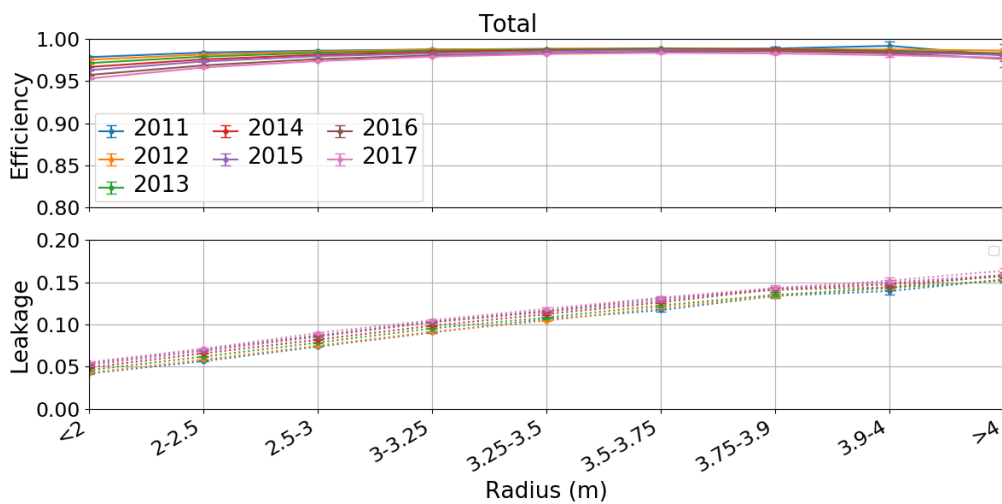
Figure 40: ^{210}Bi MC events efficiency ε_β and leakage L_α radial dependency year by year calculated with FCN214 discriminator in different parts of the detector. Colors represent different years.



(a) North



(b) South



(c) Total

Figure 41: ^{210}Bi MC events efficiency ε_β and leakage L_α radial dependency year by year calculated with FCN210 discriminator in different parts of the detector. Colors represent different years.

6 ^{210}Bi homogeneity and stability

As introduced in Chapter 4.2, in order to measure CNO it is important to confirm the homogeneity and stability of the major CNO ν background, ^{210}Bi in Borexino LS. In order to do so, the β rate is going to be studied in different energy regions, which are going to be introduced in Chapter 6.1 and then for more further studies the β -rate is going to be studied in different regions of the FV in Chapter 6.3 to prove the stability of β -rate.

6.1 Energy interval definitions

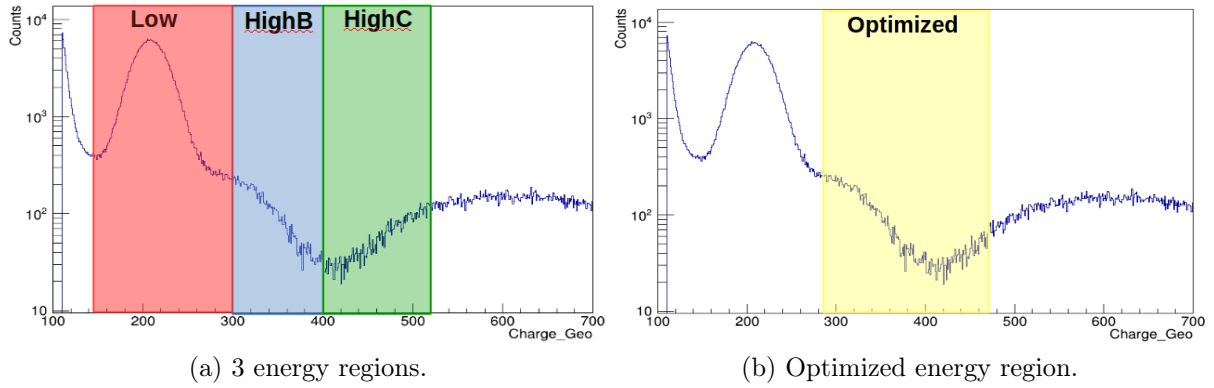


Figure 42: Different energy regions with geonormalized charge.

Energy region	Expected β rates (cpd/100t)								
	^{210}Bi	^7Be	^{85}Kr	CNO	<i>pep</i>	^{11}C	^6He	Pileup	Total β
Low	3.79	18.27	2.29	1.02	0.6	~ 0	0.13	0.81	26.91
HighB	1.18	5.06	0.14	0.42	0.39	0.01	0.13	0.04	7.37
HighC	0.46	0.01	0	0.25	0.48	3.64	0.2	0.02	5.06

Table 10: Expected rates (cpd/100t) for all species in different energy regions.

As shown in Figure 42, this part of the analysis is done in four different energy regions:

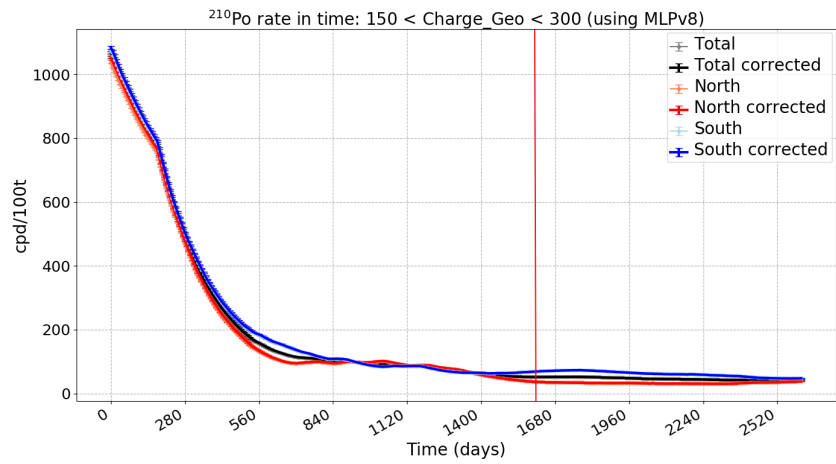
- **Low energy region** - is defined between 150 and 300 geonormalized charge. In this region most of the events are ^{210}Po , but also ^7Be and ^{210}Bi , so if one is interested in looking ^{210}Bi events, it is important to use different pulse-shape discriminations.
- **HighB energy region** - is defined between 300 and 400 geonormalized charge. Mostly ^{210}Bi events with some ^7Be events, but no α -events, which means there is no need to use pulse-shape discriminations.
- **HighC energy region** - is defined between 400 and 520 geonormalized charge. This is a control region, mostly populated with ^{11}C events.

- **Optimized energy region** - is defined between 284 and 471 geonormalized charge. This region is calculated, where the ^{210}Bi signal to background ratio (calculated with equation 47) is the highest. Mainly populated with ^{210}Bi (1.81 cpd/100t) and ^7Be events, but no α events, which means there is no need to use pulse-shape discriminations.

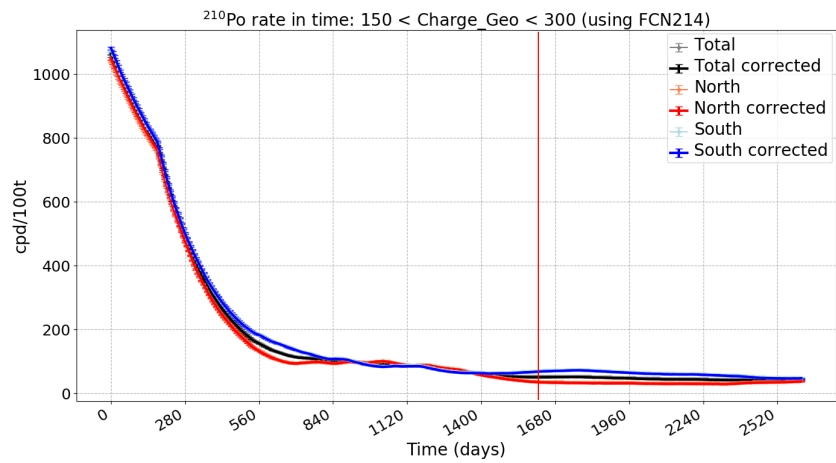
As shown above under the description of energy regions, they consist of different species (solar neutrinos and background events), as shown in Table 10. When talking about solar neutrinos it is important to notice that they have a seasonal variation of $\pm 3\%$, which means the rate of solars differs depending of the time of the year. In order to get clearer view, we study the stability in one year bins, using a moving average method in time. The variations of β rate after seasonal corrections should be due to ^{210}Bi .

6.2 In fiducial volume

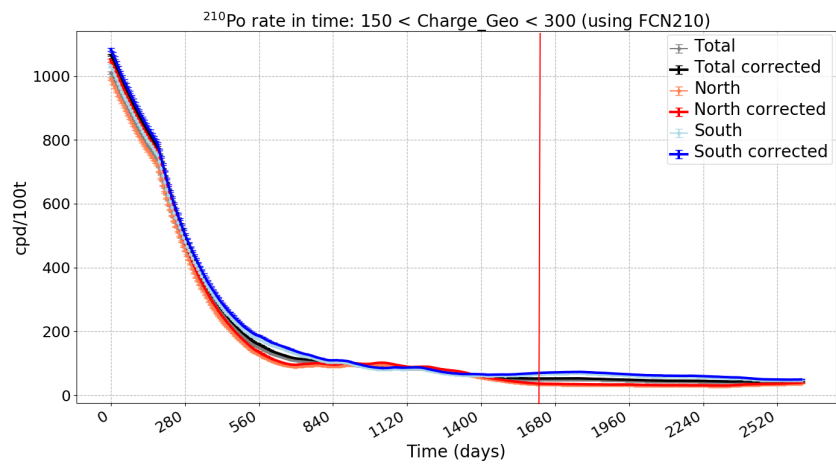
6.2.1 α events in time



(a) MLPv8



(b) FCN214



(c) FCN210

Figure 43: ^{210}Po events with different pulse-shape discriminators in low energy region. The x-axis represents the time from the end of 2011 (as 0) until June 2019 (as 2520). The vertical red line represents the start of Phase-III (May 2016).

In previously defined Low energy region if one wants to look at the β events, it is necessary, to look at ^{210}Po events before, because of the α leakage L_α (calculated in Chapter 5.4.2) into β events.

In Figures 43a, 43b, and 43c one can see the ^{210}Po rate in time in the whole FV and only in the north ($z > 0$) of the detector and in the south ($z < 0$) of the detector, the lighter colors represent the initial ^{210}Po rate without any corrections and the darker colors are with efficiency and leakage corrections. From this rate one can later subtract the α leakage L_α from β rate.

6.2.2 β rate in different energy regions

β rate in Low energy region with corrections:

In Figure 44, one can see the initial rate of β events in time, this means events without any corrections. The β rate is quite high especially in the end of 2011 and in 2012, which could indicate a high α leakage into β events. So in order to look only at β events in low energy region, one needs to subtract the α -leakage first, as can be seen in Figure 45, where blue line is the initial β rate in the whole detector, obtained with MLPv8 discriminator and the red line is the events after subtracting α -leakage L_α . Then it can be seen how the distribution of β -like events is quite flat in time, as was expected to achieve by subtracting the α -leakage L_α . As showed in Chapter 5, the β -efficiency ε_β was never 100% with any discriminator and is time dependent, this means it is necessary to add the β -efficiency ε_β and the final β rate can be seen with the green line as the corrected value for events in low energy region. All calculations were made with three discriminators, but since MLPv8 showed the most stable results only calculations with this discriminator are showed here, others (FCN214 and FCN210) can be found in Appendix E.

To compensate the seasonal variation of solars all plots include a moving average, which means calculating the β rate in specific time also the rate six months before and after this time are being considered, however, this also introduces correlation between the points. Later when estimating the uncertainty as the RMS of these projections, these correlations are not being considered. But if the correlations would be considered, the uncertainty would decrease.

Figure 46 shows the initial and corrected β rate with all three discriminators in low energy region. The time scale starts from the end of 2011 and continues until June 2019. It can be seen that in the early years the α -leakage is quite high especially with FCN210, but after corrections all discriminators show stable results in low energy region, especially MLPv8, which showed the smallest residual α contamination in 2011-2012.

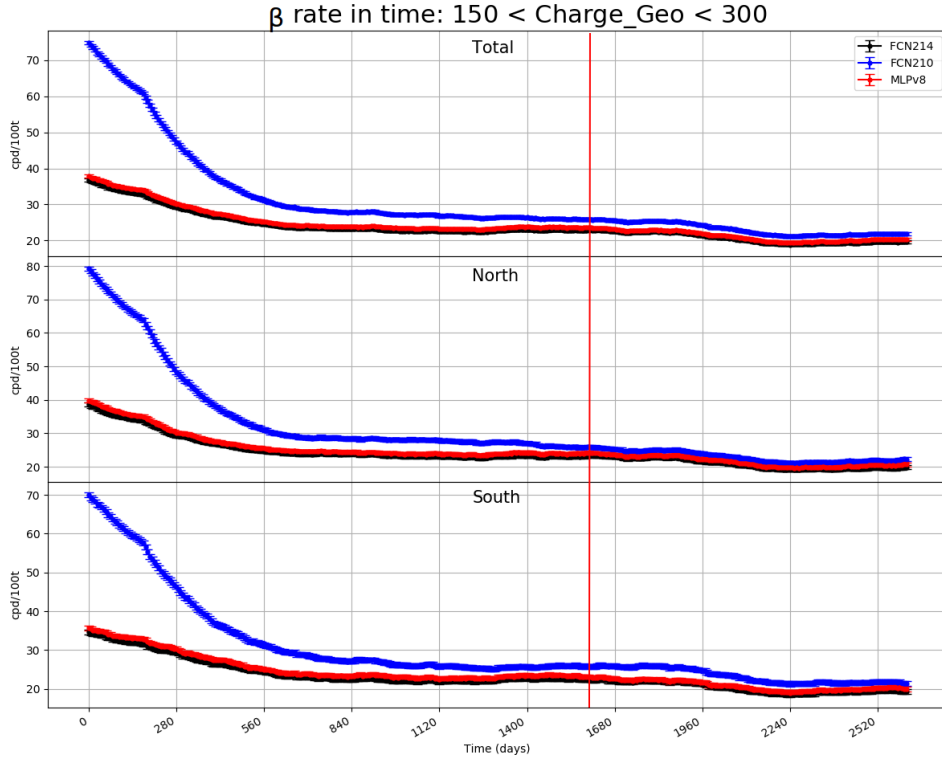


Figure 44: Initial β rate in the whole detector and separately for north ($z > 0$) and south ($z < 0$) parts of the detector. Different colors belong to discriminators, red - MLPv8, black - FCN214, blue - FCN210. The x-axis represents the time from the end of 2011 (as 0) until June 2019 (as 2520). The vertical red line represents the start of Phase-III (May 2016).

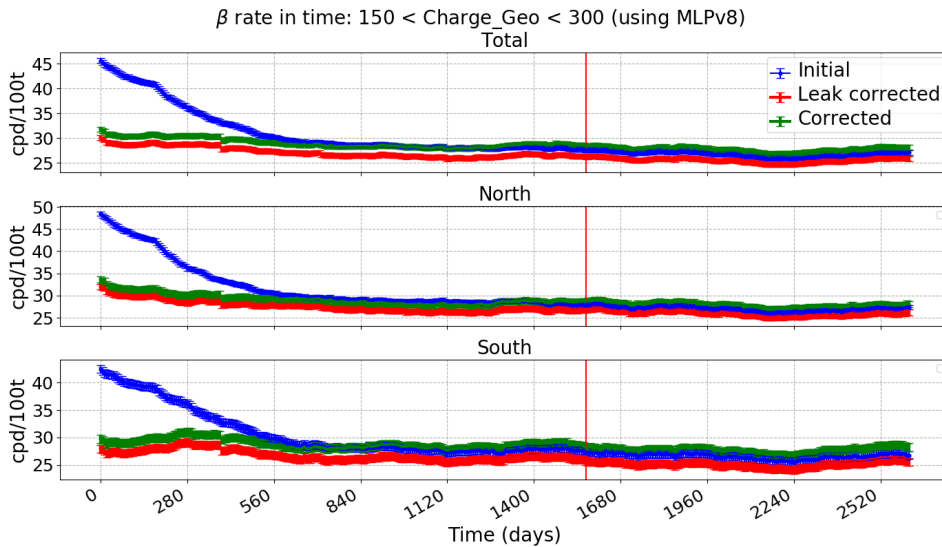
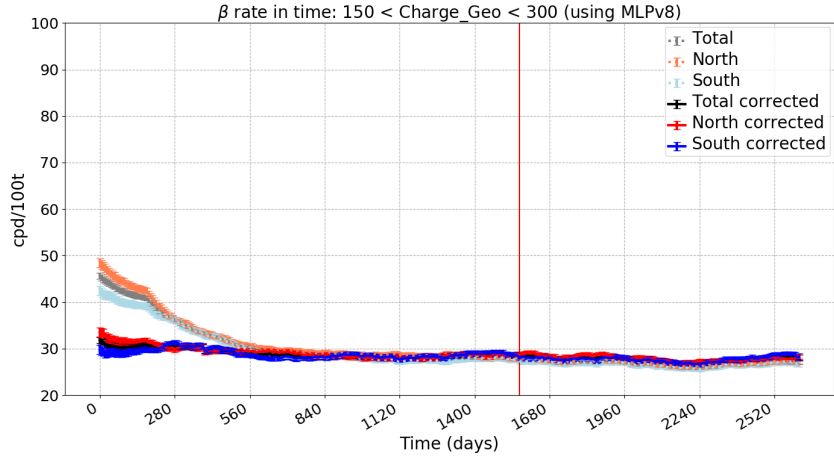
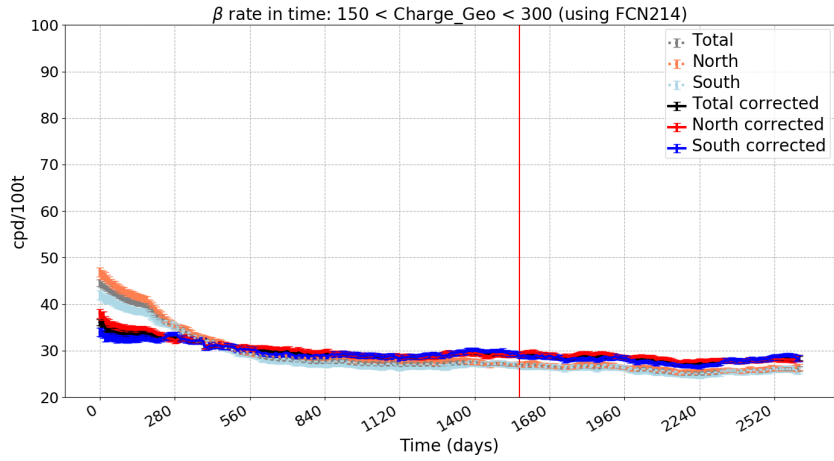


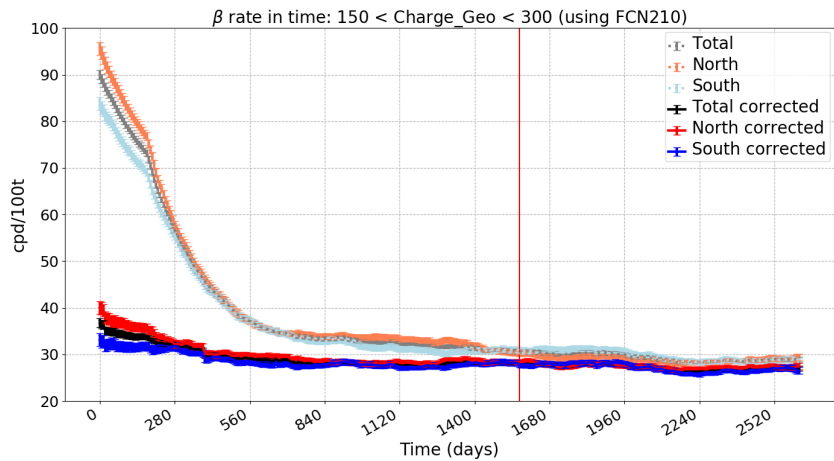
Figure 45: Efficiency ε_β and leakage L_α corrections for MLPv8 discriminator. Blue line is the initial β -rate obtained with discriminator, red line represent only leakage corrections and green line is the final corrected β -rate in low energy region. The x-axis represents the time from the end of 2011 (as 0) until June 2019 (as 2520). The vertical red line is the start of so called Phase-III (May 2016).



(a) MLPv8



(b) FCN214



(c) FCN210

Figure 46: Initial and corrected β rate events with different pulse-shape discriminators in low energy region. The light colors represent the initial rate in the whole detector and separately for north and south, the bright colors represent the corrected values. The x-axis represents the time from the end of 2011 (as 0) until June 2019 (as 2520). The vertical red line is the start of so called Phase-III (May 2016).

β rate in higher energy regions:

The β rate in higher energy regions was calculated from the end of 2011 until June 2019 as shown in figures below.

In HighB energy region there are only β events, hence no need for pulse-shape discriminators. As shown in Figure 47, the β rate is decreasing until February 2016, after the thermal insulation in 2015 the β rate reached the lowest level and after that slow increase can be seen.

In the control energy region, mainly populated with ^{11}C events, to see if there are any irregularities happening in the detector. As shown in Figure 48 the β rate is quite stable until the latest period starting from 2240 days which represents the end of May in 2018, where it shows some discrepancy.

The Optimized energy region is similar to HighB energy region, only β events in time, shown in Figure 42b, the β rate is decreasing until February 2016 and after that quite stable results except a small increase in the later period.

In conclusion to β rate in optimized energy region, the rate is calculated in Table 11 time dependently and in different parts of the detector.

β rate in higher energy regions showed a decreasing trend until year 2016, this can be because of high ^{210}Bi rate in the early years, was probably caused by convection currents that brought batches of LS with higher intrinsic ^{210}Bi contamination in the FV. After that, ^{210}Bi is expected to homogenize through diffusion. After adding the thermal stabilization to the detector in 2015, it can be seen how the β rate is quite low and stable. Only in the later period it can be seen, that the β rate has started to increase slowly, more precise values in Optimized energy region year by year can be seen in Table 5.

	Total (cpd/100t)	North (cpd/100t)	South (cpd/100t)
2012	13.186 ± 0.267	13.508 ± 0.374	12.823 ± 0.382
2013	11.940 ± 0.272	11.840 ± 0.371	12.053 ± 0.399
2014	11.395 ± 0.251	10.996 ± 0.343	11.845 ± 0.370
2015	10.894 ± 0.232	11.016 ± 0.322	10.757 ± 0.334
2016	10.686 ± 0.259	10.821 ± 0.365	10.534 ± 0.367
2017	10.967 ± 0.233	10.792 ± 0.316	11.164 ± 0.343
2018	11.158 ± 0.223	11.245 ± 0.308	11.060 ± 0.322
2019	11.192 ± 0.344	11.134 ± 0.473	11.258 ± 0.501

Table 11: The average β rate in optimized energy region in different years starting from 2012 until 2019. Columns represent the whole detector as total and the rate in north and south parts of the detector.

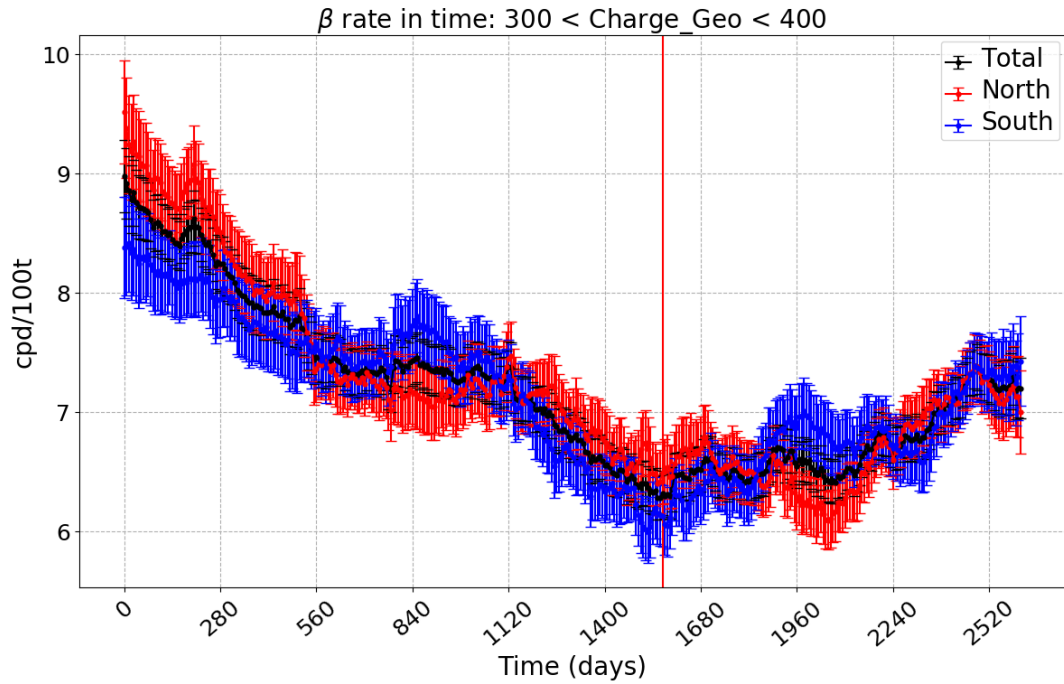


Figure 47: β rate in time in HighB energy region. Different colors represent the position in detector. The x-axis represents the time from the end of 2011 (as 0) until June 2019 (as 2520). The vertical red line is the start of so called Phase-III (May 2016).

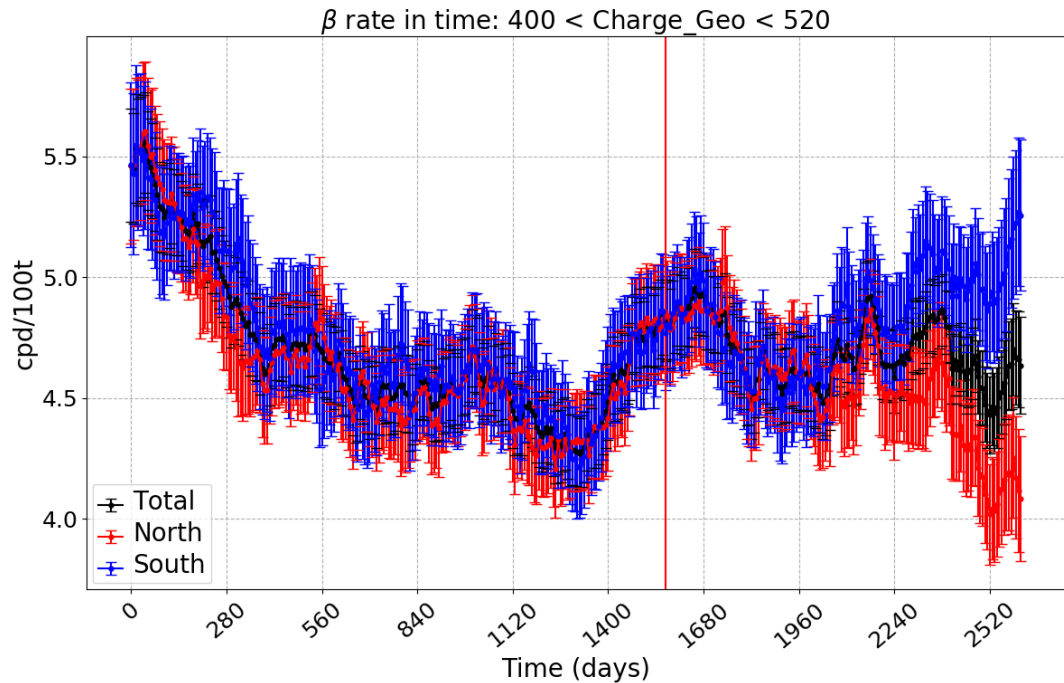


Figure 48: β rate in time in HighC energy region. Different colors represent the position in detector. The x-axis represents the time from the end of 2011 (as 0) until June 2019 (as 2520). The vertical red line is the start of so called Phase-III (May 2016).

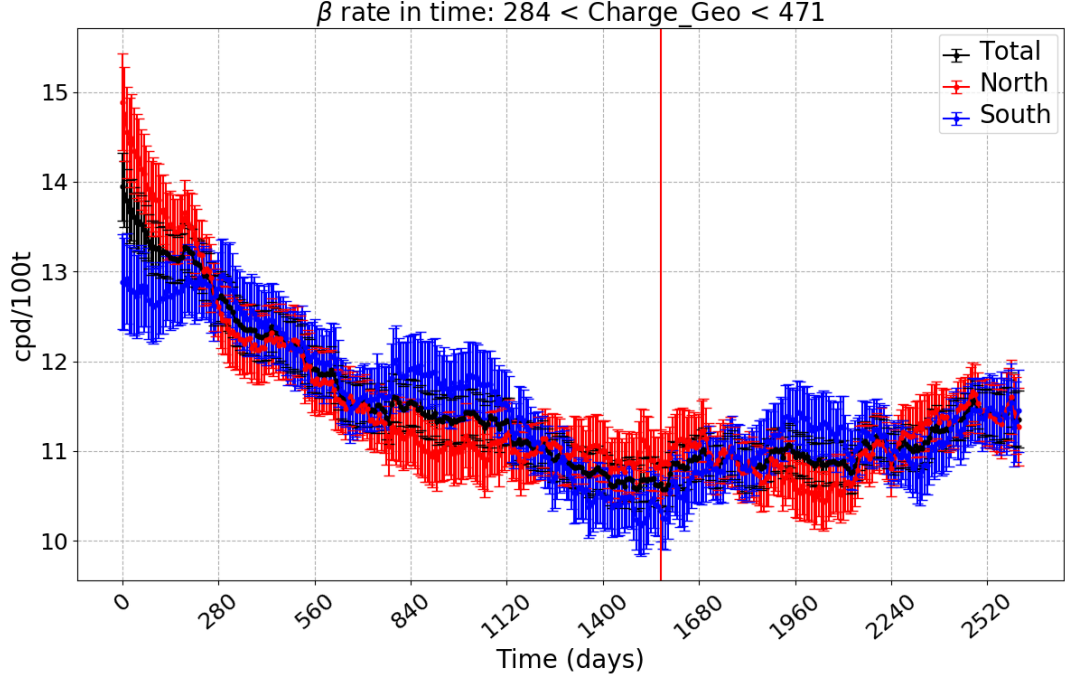


Figure 49: β rate in time in optimized energy region. Different colors represent the position in detector. The x-axis represents the time from the end of 2011 (as 0) until June 2019 (as 2520). The vertical red line is the start of so called Phase-III (May 2016).

In Figures 50, 51, 52, and 53, the distribution of β events is shown in different energy regions with their respective RMS values for Phase-III. In Low energy region with the most stable discriminator (MLPv8) the rate is 27.796 with a RMS value of ± 0.476 , being the lowest RMS value in this energy region, in HighB energy region it is 6.728 with a RMS value of ± 0.299 , in HighC region is 4.688 with a RMS value of ± 0.129 , and in Optimized energy region it is 11.039 with a RMS value ± 0.266 .

The average β rate in Phase-III data (from May 2016 - until June 2019) is calculated and represented in Table 12 with corresponding uncertainty, calculated with RMS values considering the ^{210}Bi fraction in every energy region (shown in Table 10). In Low energy region the most stable results with lowest α leakage were with MLPv8 discriminator and in Table 12 can be seen how the mean β rate has the lowest RMS with this discriminator, being 27.796 ± 1.506 . In higher energy regions the mean β rate is 6.728 ± 3.051 , 4.688 ± 3.395 , and 11.039 ± 1.497 in HighB, HighC, and Optimized energy region respectively. It can be seen how the uncertainty is the lowest based on Low and Optimized energy regions, the reason for higher uncertainty values in HighB and HighC regions is small fraction of ^{210}Bi , which increases the statistical error.

Energy region	Mean	RMS	Uncertainty
Low (MLPv8)	27.796	0.476	1.506
Low (FCN214)	28.220	0.572	1.810
Low (FCN210)	27.293	0.570	1.804
HighB	6.728	0.299	3.051
HighC	4.688	0.129	3.395
Optimized	11.039	0.226	1.497

Table 12: The mean β rate in every energy region in Phase-III (July 2016 - June 2019).

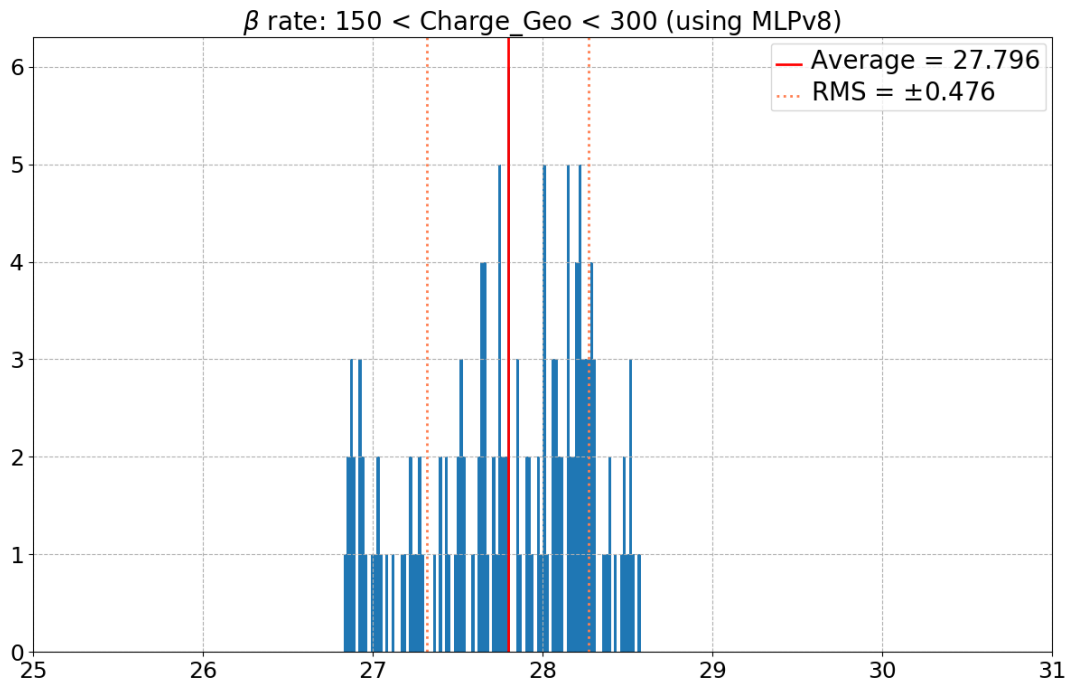


Figure 50: Distribution of β -like events in Low energy region in Phase-III. The vertical red line is the average and the two vertical orange lines are the RMS values.

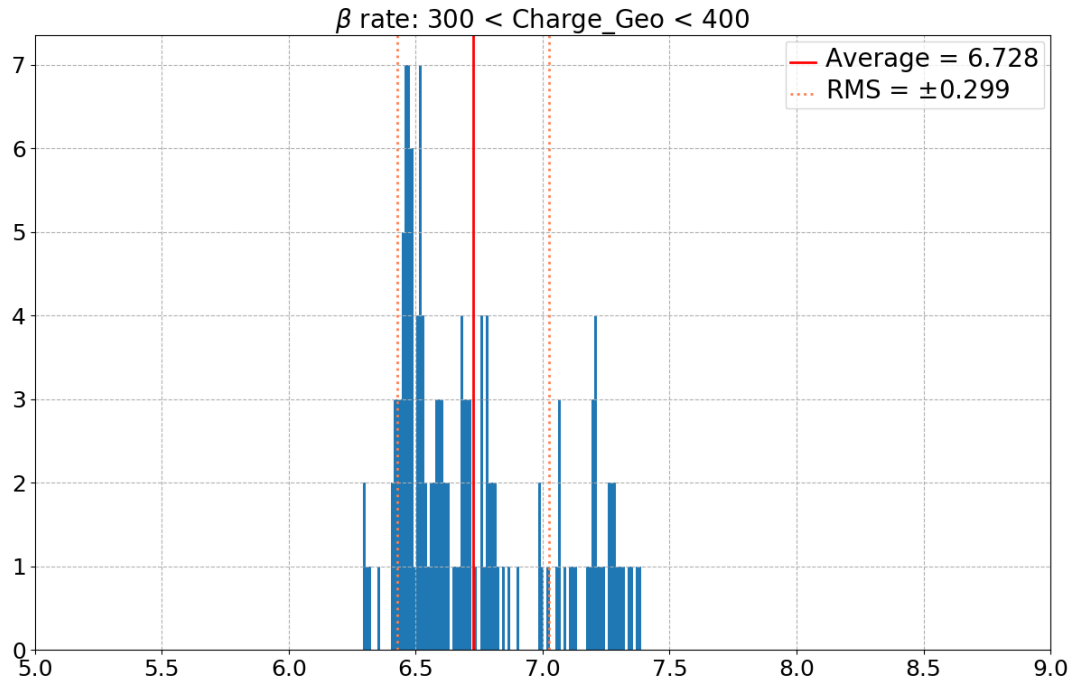


Figure 51: Distribution of β -like events in HighB energy region in Phase-III. The vertical red line is the average and the two vertical orange lines are the RMS values.

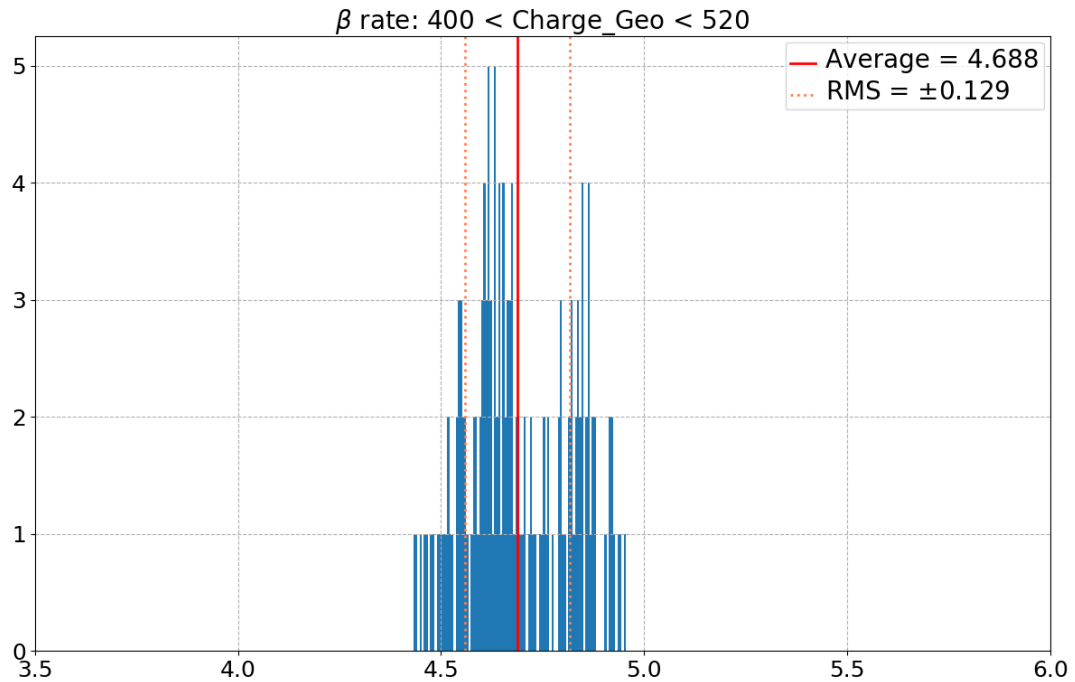


Figure 52: Distribution of β -like events in HighC energy region in Phase-III. The vertical red line is the average and the two vertical orange lines are the RMS values.

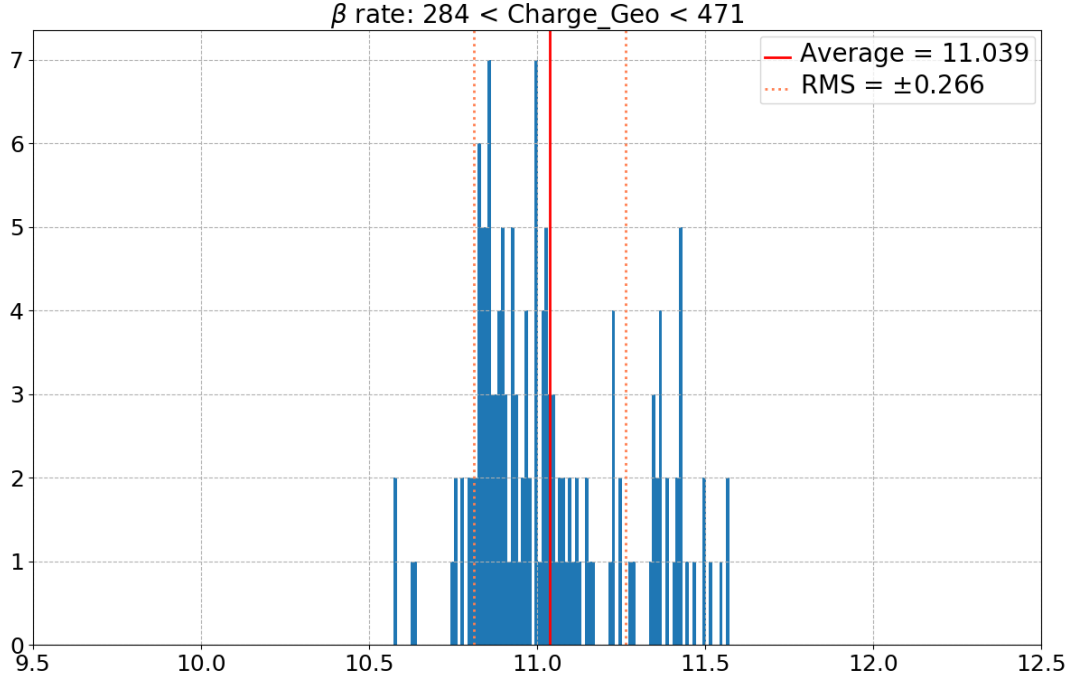


Figure 53: Distribution of β -like events in Optimized energy region in Phase-III. The vertical red line is the average and the two vertical orange lines are the RMS values.

6.3 Top-bottom dependency

In this chapter the *pep* FV ($r < 2.8$ m, -1.8 m $< z < 2.2$ m) is divided into 6 slices, as shown in Figure 54.

Slices with similar volume, starting from the bottom of the detector:

- **slice 0:** -1.80 m $< z < -1.05$ m
- **slice 1:** -1.05 m $< z < -0.46$ m
- **slice 2:** -0.46 m $< z < 0.10$ m
- **slice 3:** 0.10 m $< z < 0.66$ m
- **slice 4:** 0.66 m $< z < 1.28$ m
- **slice 5:** 1.28 m $< z < 2.20$ m

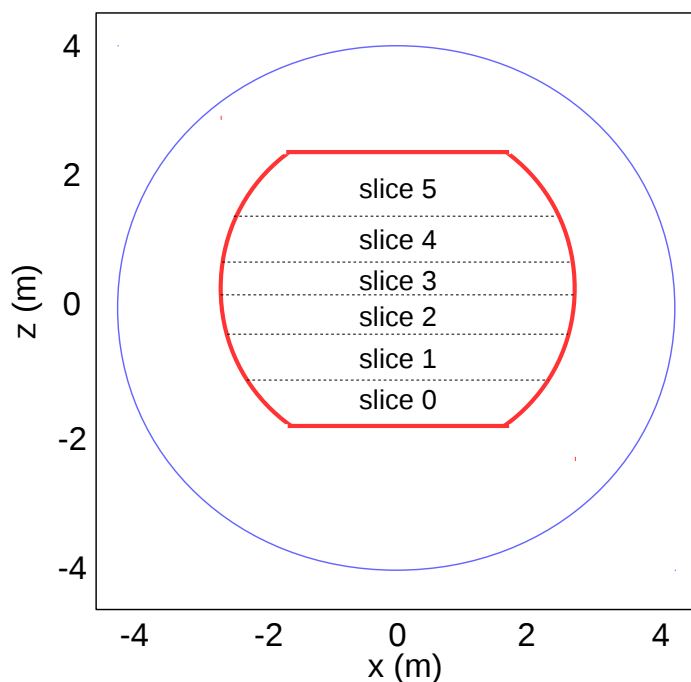


Figure 54: *pep* FV with 5 horizontal cuts in z -axis. The blue line represents the approximate IV and the red line is the *pep* FV.

6.3.1 The time dependency of each slice

In Low energy region:

In Figures 55 the β rate in every slice is brought out separately with MLPv8 discriminator, which showed the most stable results the results compared to the other discriminators. Starting from the bottom of the detector with slice 0 until slice 5 representing the top of the detector the best stable regions are in the middle of the FV as can be seen in slices 1 and 2.

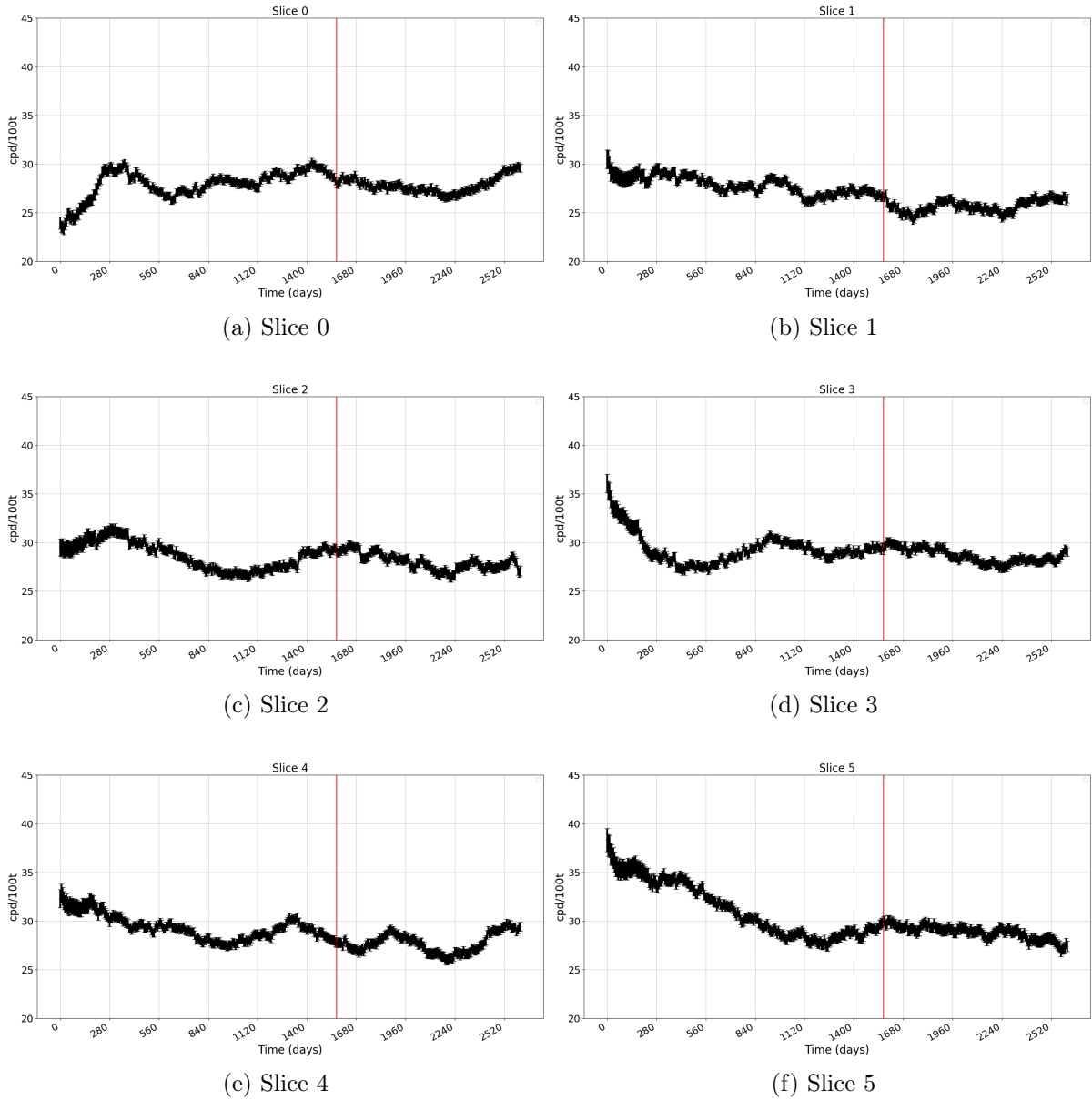


Figure 55: β rate in time separately for every slice in Low energy region with MLPv8.

In HighB energy region:

Looking at the events in highB energy region in Figure 56, it can be seen how the most stable results are in the bottom of the detector as shown in slices 0 (Figure 56a) and 1 (Figure 56b). In Phase III, starting from 1568 days, the results are mostly stable with only small fluctuations especially in top and bottom of the detector.

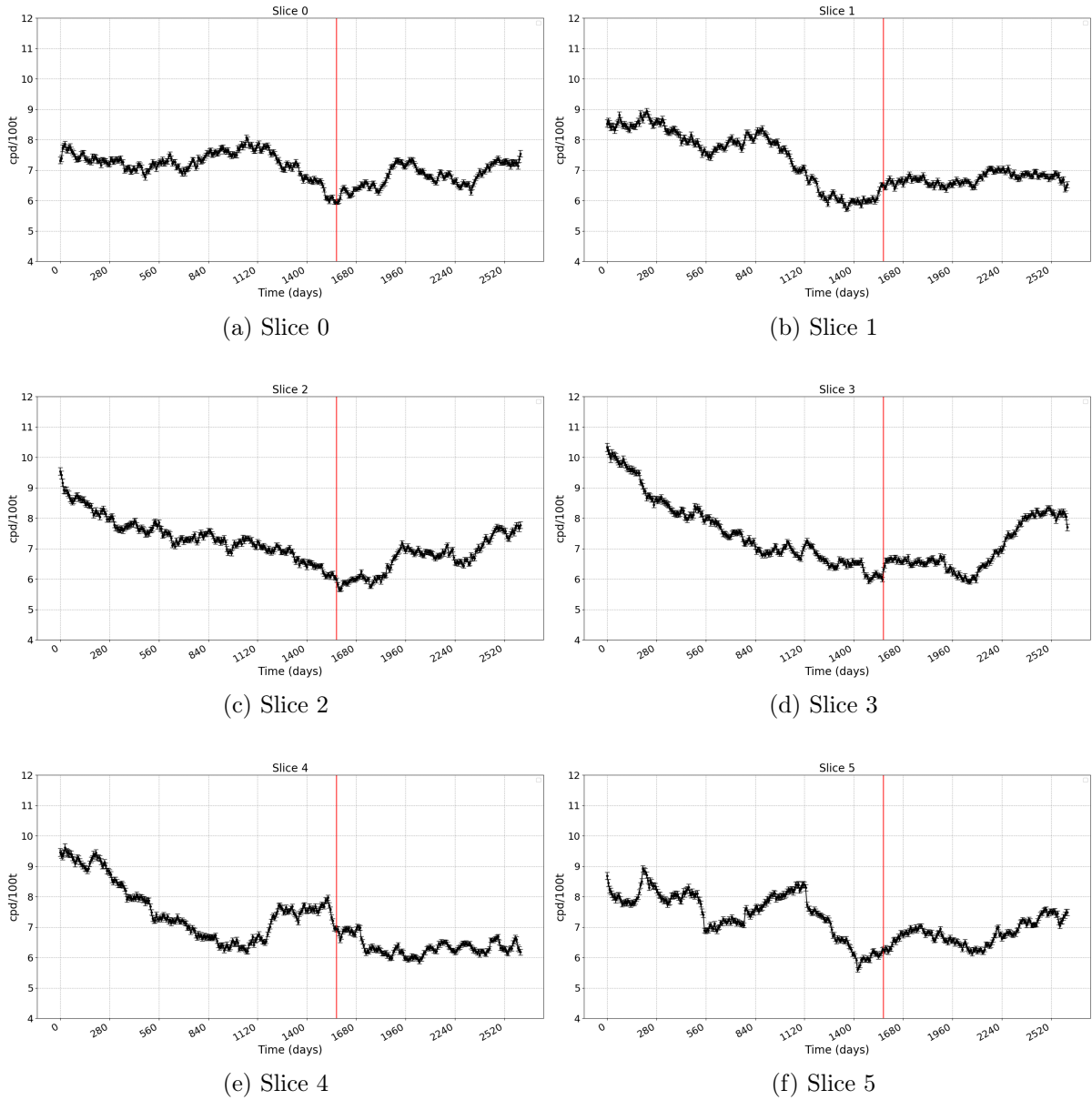


Figure 56: β rate in time separately for every slice in HighB energy region.

In HighC energy region:

Looking at the events in control energy region in Figure 57, it can be seen that all slices are stable with low β rate.

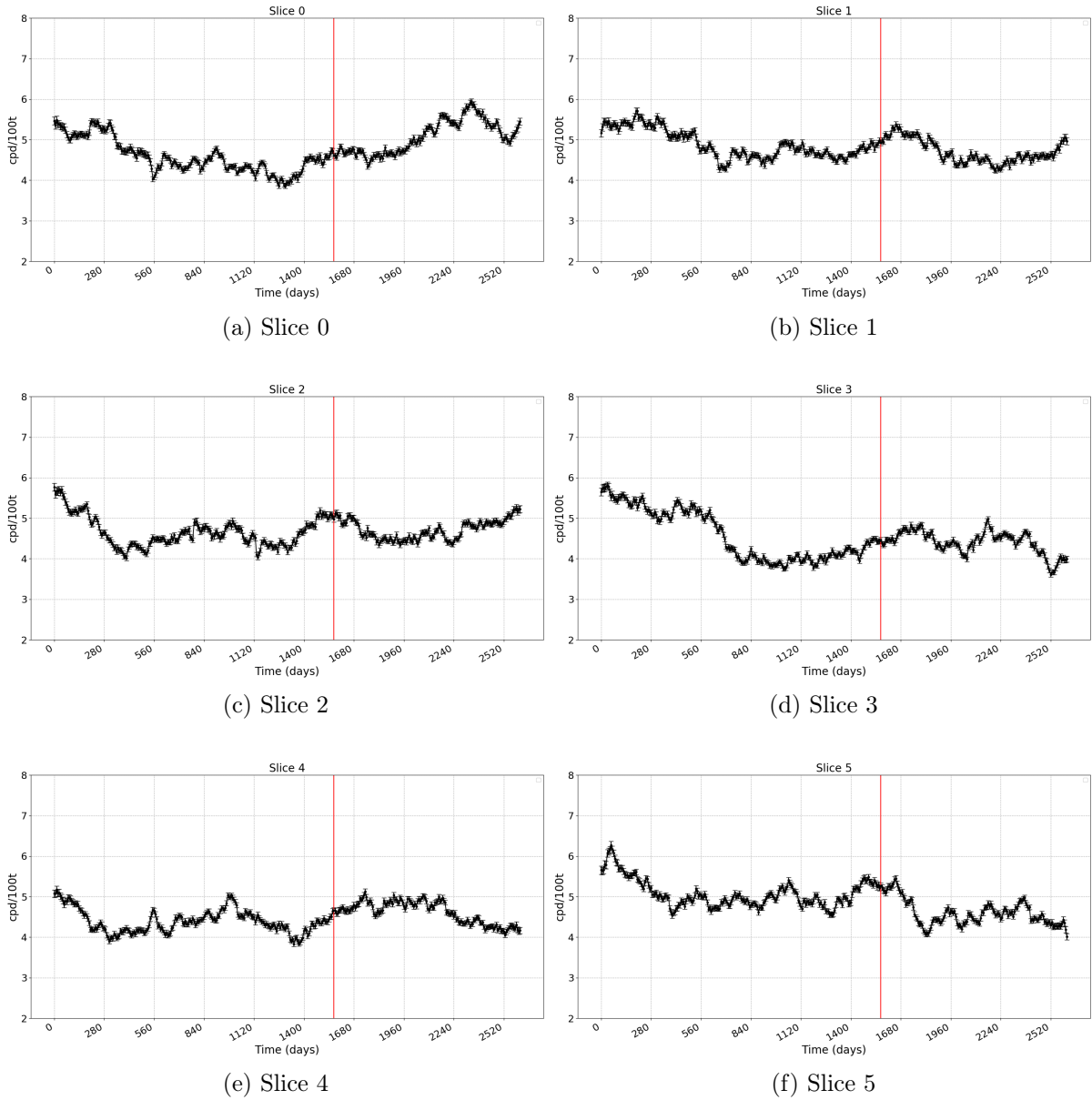


Figure 57: β rate in time separately for every slice in HighC energy region.

In Optimized energy region:

Looking at the events in optimized energy region in Figure 58, most stable results are in the bottom of the detector in slices 0 (Figure 58a) - 2 (Figure 58c). Same as in highB energy region, when looking the β events in Phase III, starting from 1568 days, the most stable results are in top and bottom of the detector.

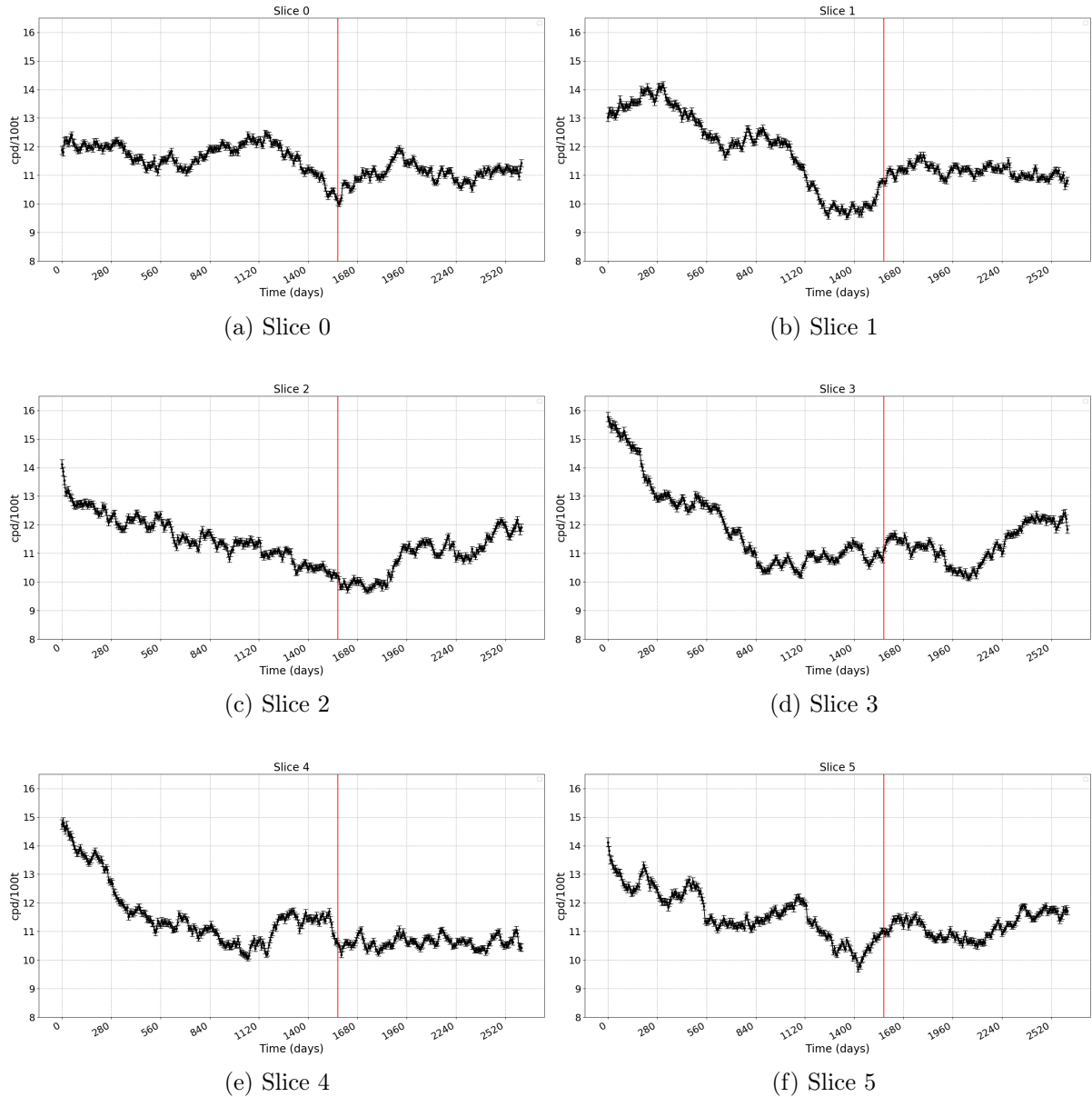


Figure 58: β rate in time separately for every slice in Optimized energy region.

6.3.2 Slice dependency of every year

In Figure 59 and in Table 13 the β rate slice dependently is showed for Phase-III data. In Low energy region, in Figure 59a, it can be seen how the β rate is stable and around ~ 28 cpd/100t, similar as it was calculated in Chapter 6.2.2. Only different slice from the average is Slice 1, being the second bottom slice in the detector. In HighB energy region, in Figure 59b, the average β rate is between 6.5 and 7 cpd/100t, with the only difference in Slice 4, being the second top most slice. In the control region, in Figure 59c, decreasing rate of β -like events can be seen from the bottom to the top of the detector. But the average rate in HighC region is between 4.4 and 5.2 cpd/100t, which does not make the decrease high. The most stable results can be seen in Optimized energy region, in Figure 59d, where the β rate is between 10.5 and 11.5 cpd/100t. All calculations are in an agreement with the mean β rate calculations in Table 12.

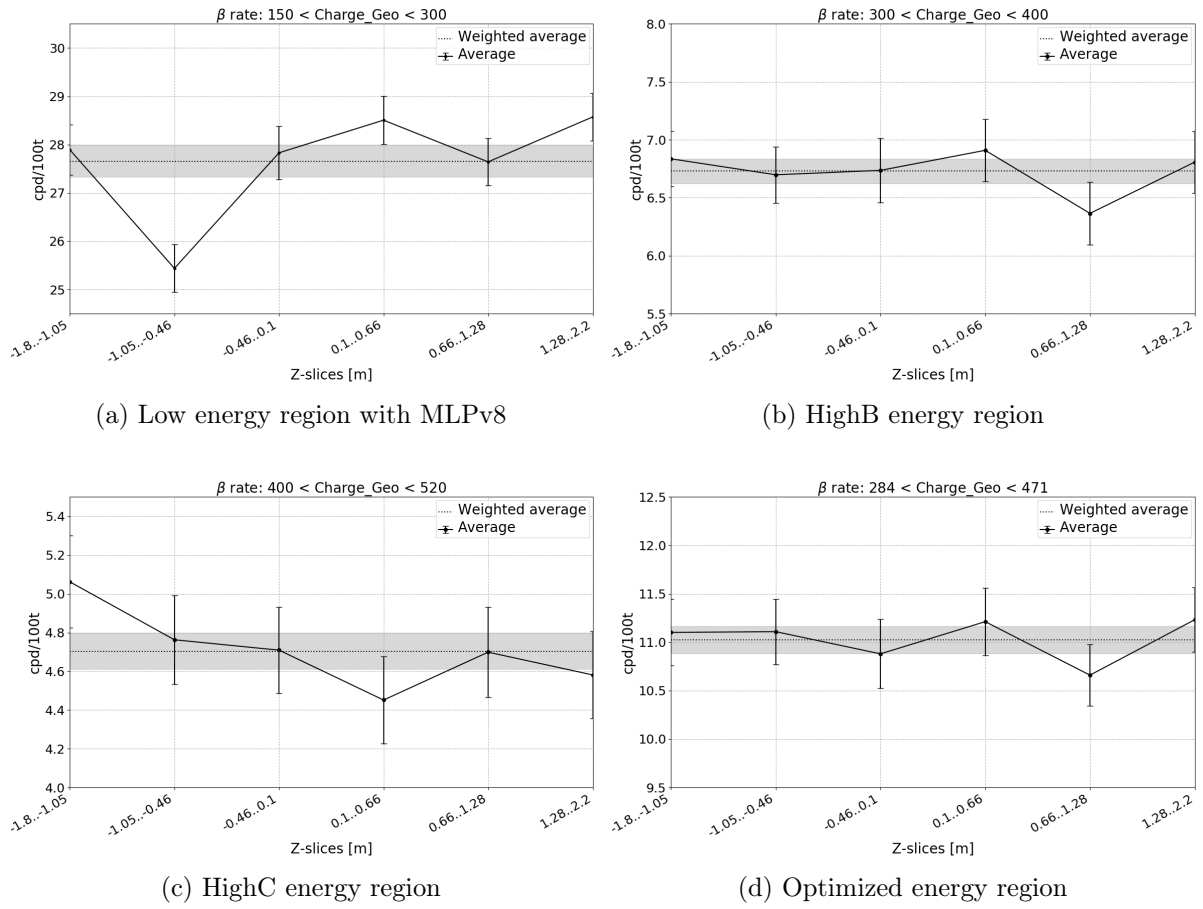


Figure 59: β rate in different slices separately in Phase-III.

Energy region	Weighted average	RMS	Uncertainty
Low (MLPv8)	27.654	0.328	1.038
HighB	6.731	0.106	1.082
HighC	4.704	0.093	2.447
Optimized	11.025	0.138	0.914

Table 13: The weighted average β rate in every energy region in Phase-III (July 2016 - June 2019).

Conclusions

The β -rate dependency on the top-bottom position in the detector shows quite stable results. When looking at β -events in time the results are stable in Phase III especially in the most bottom slices. And looking at β -rate slice dependently the results in Phase III are very stable particularly in Optimized energy region.

7 Conclusions and outlook

One of the main goals of Borexino detector is to measure the CNO neutrinos, therefore to give a direct proof of CNO burning in the Sun. For Sun the CNO cycle is predicted to be responsible for $\sim 1\%$ of the total energy production, nevertheless for stars more massive than our Sun, the CNO cycle is the dominant energy production mechanism.

It is complicated to measure the CNO ν s in the Borexino detector for two main reasons, first the flux of CNO ν s is quite slow and the energy is also rather low, as shown in Figure 3 (represented as yellow dashed lines). Secondly CNO ν s have a very similar spectral shape to *pep* solar ν fluxes and to ^{210}Bi β -decay into ^{210}Po , these events cannot be easily disentangled from the CNO ν s in fits, therefore it is highly important to constrain these values independently. In order to have a precise value of the ^{210}Bi events in the liquid scintillator, it is important to prove the homogeneity and stability of ^{210}Bi decay rate in the Borexino detector.

For that, the α/β discriminators were studied to find the best threshold cut for each discriminator, to get the most β -events with the lowest leakage of α -events.

After optimizing they were studied on ^{214}Bi and ^{214}Po WE data and then the performance of discriminators was compared to ^{214}Bi and ^{214}Po MC events. The conclusions were made in Tables 6 and 7, where it was concluded that data and MC events are compatible and when one is interested in high values for β -efficiency ε_β and low α -leakage L_α values, the best discriminators for that are MLPv8, FCN214, and FCN210. Later the performance of named discriminators was studied on ^{210}Bi and ^{210}Po MC events, where we have a larger data set following the realistic detector performance in time and non-homogenous ^{210}Po distribution to analyse the results on time dependent. And these results, represented in Figure 38, were used later to correct β values in Low energy region in Chapter 6. Since ε_β was never 100% with any discriminator and is time dependent then before looking at β -like events in Low energy region it was important to subtract the α -leakage L_α and add the β -efficiency ε_β to get pure β -like events.

To prove the ^{210}Bi homogeneity and stability in the liquid scintillator, the β rate was studied in different energy regions, see Chapter 6.1, in the whole *pep* FV (see Chapter 6.2.2) and top-bottom dependently (see Chapter 6.3), with Phase-III data.

As shown in Figure 60 (preliminary plot made by Borexino Collaboration) the measurement of CNO is critically dependent on the absolute uncertainty on ^{210}Bi constrain. To potentially measure CNO at $\sim 4\sigma$ the estimated uncertainty on ^{210}Bi should not exceed 2cpd/100t.

For that we looked at the β events in the whole *pep* FV and more precisely in different z-slices top-bottom dependently, in different energy regions. It was concluded that the β rate is compatible with both approaches and the uncertainty on ^{210}Bi is brought out in Table 12. Comparing different energy regions, the best regions to estimate the homogeneity of ^{210}Bi are Low and Optimized energy regions, because in HighB and HighC the ^{210}Bi fraction is very small, hence the big statistical error. It can be concluded that ^{210}Bi is sufficiently homogeneous for the requirements of CNO measurement in Low and Optimized energy regions.

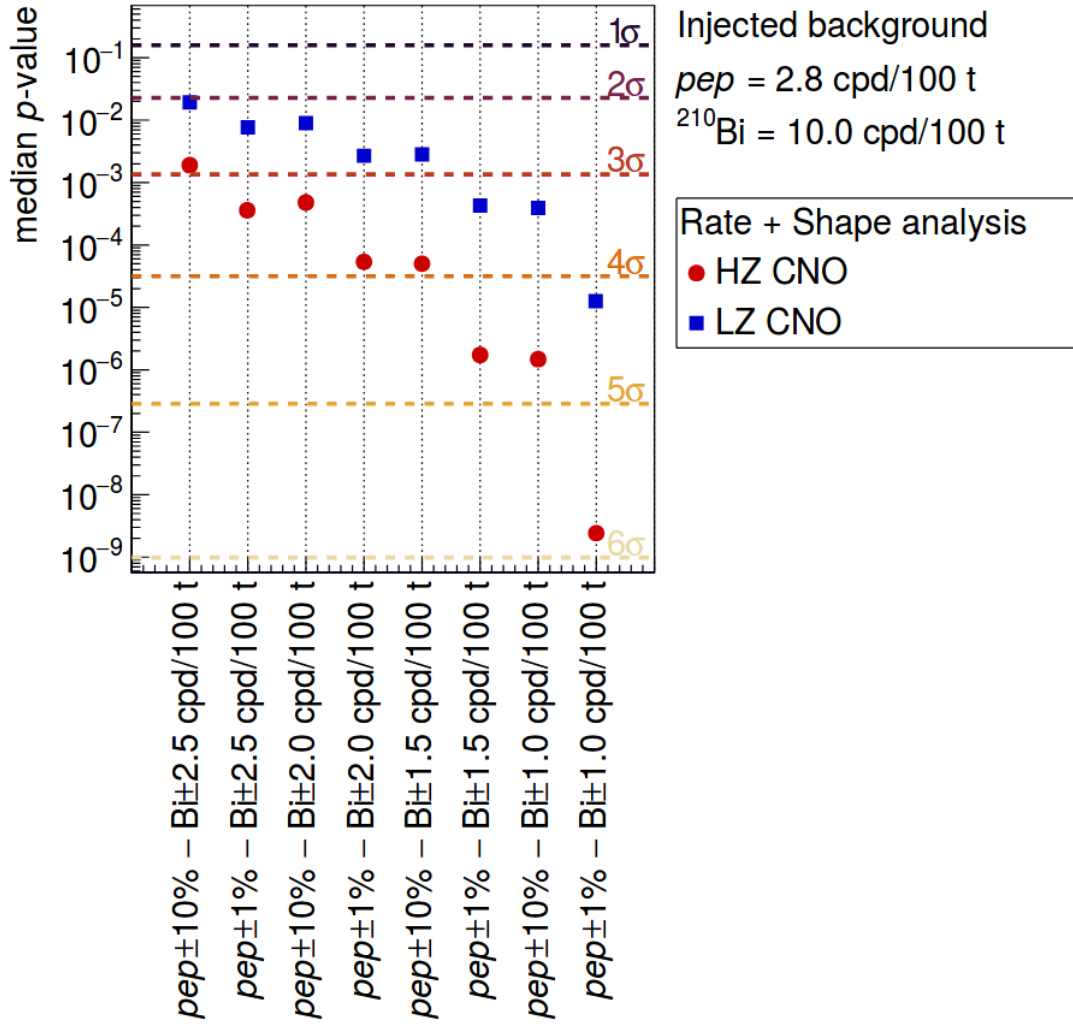


Figure 60: Discovery potential of CNO neutrino, obtained considering ~ 3 years of data taking. On x-axis the hypothetical constrains are applied to ^{210}Bi and $pep \nu$. The corresponding significance in σ is indicated by the colored horizontal lines.

Appendices

Appendix A

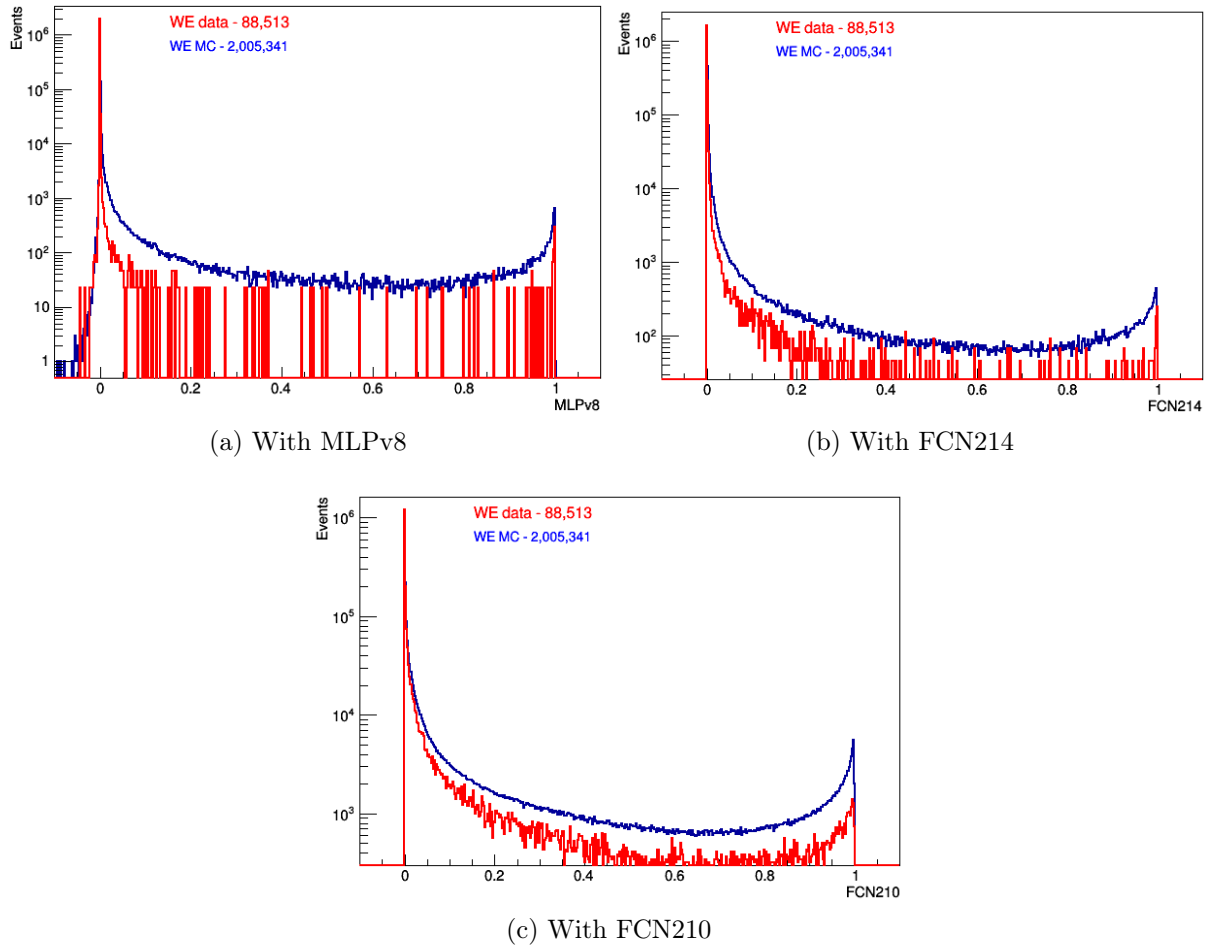


Figure 61: Distribution of ^{214}Po with data (red line) and MC (blue line) with different pulse-shape discriminators.

Appendix B

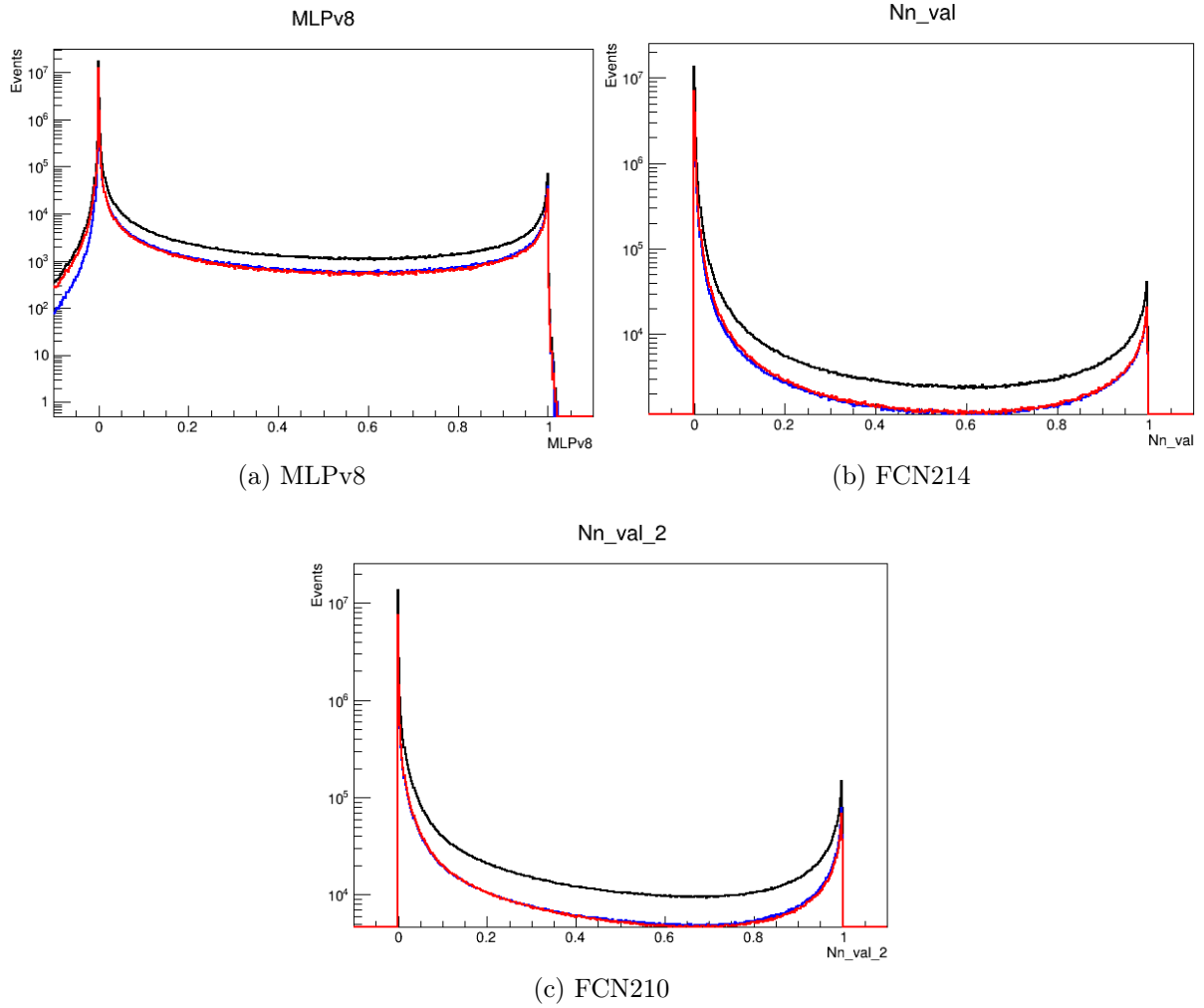
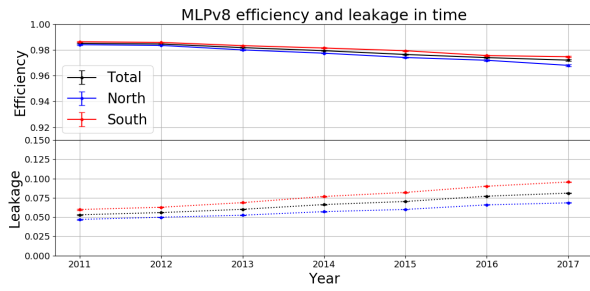
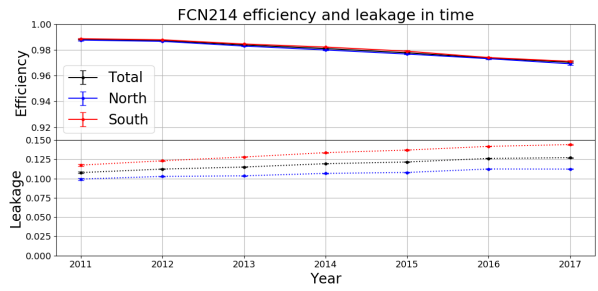


Figure 62: Distribution of ^{210}Po MC events with different discriminators. Black line shows the total events within selected energy region and *pep* FV, blue and red lines show the events in northern ($z > 0$) and southern ($z < 0$) part of the detector respectively.

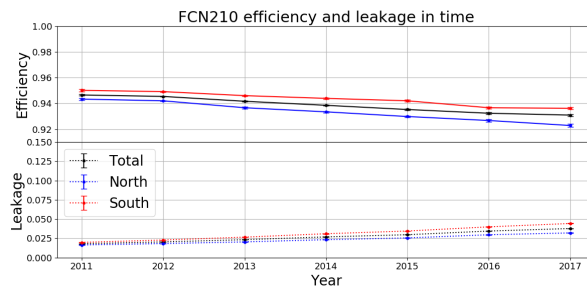
Appendix C



(a) MLPv8



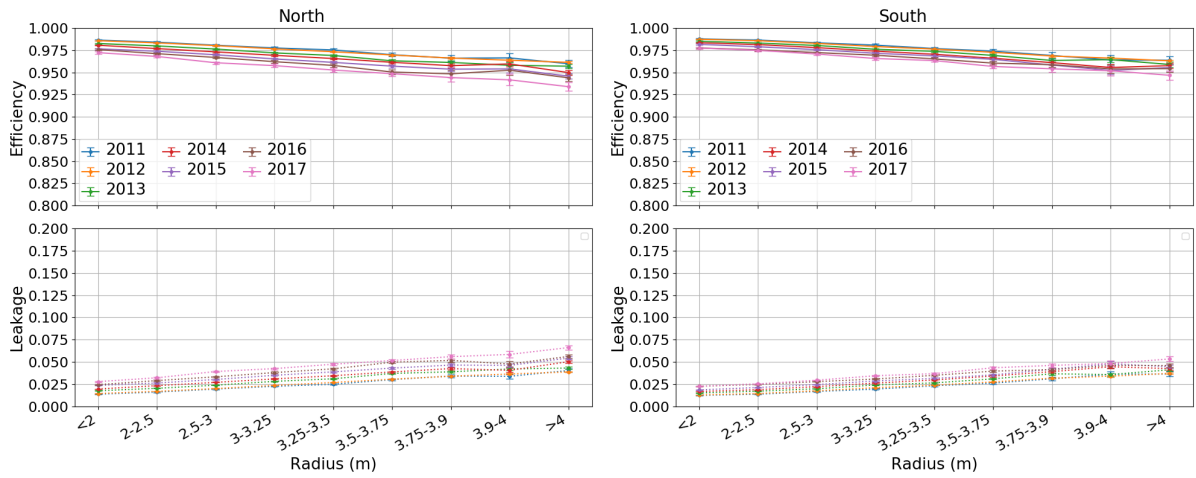
(b) FCN214



(c) FCN210

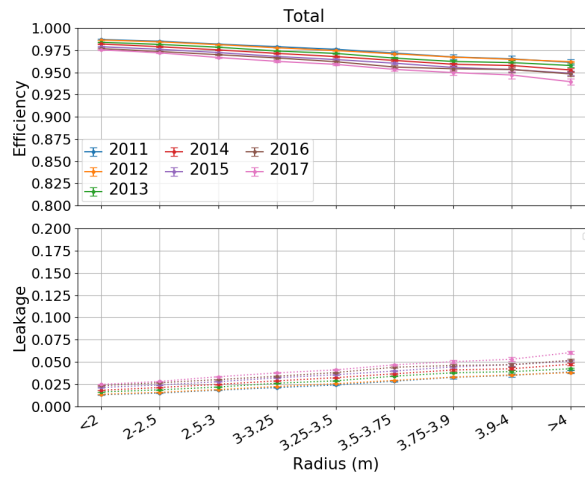
Figure 63: Time dependency of ^{210}Po MC events with all discriminators. Different colors represent position in detector, black line represents the whole detector, blue and red the northern ($z > 0$) and southern ($z < 0$) parts of the detector.

Appendix D



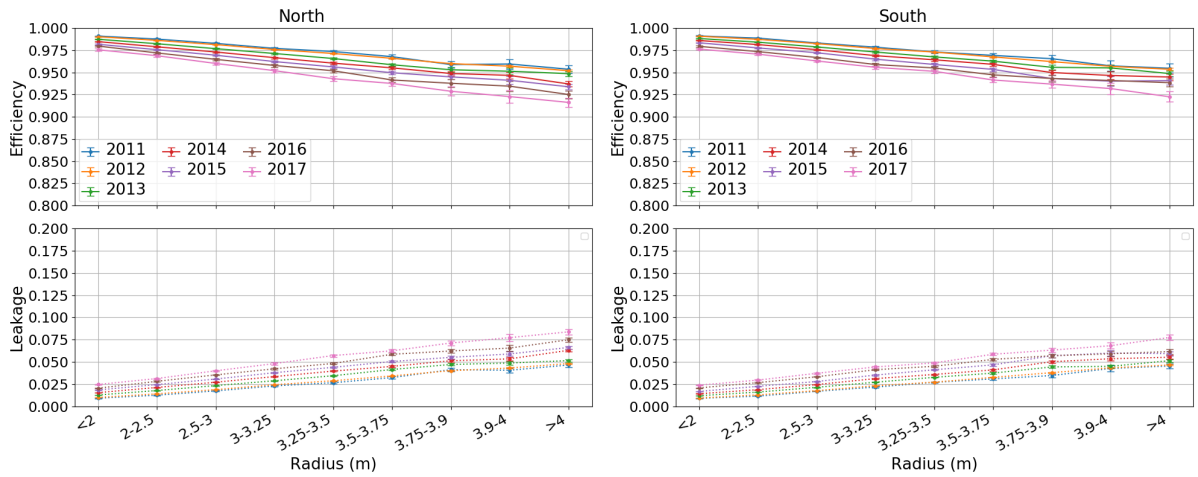
(a) North

(b) South



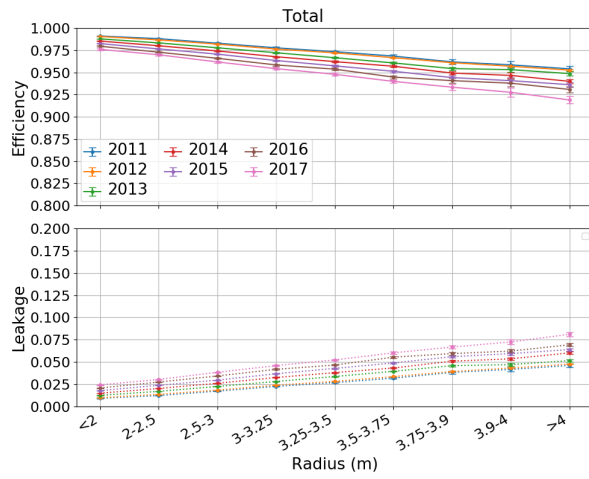
(c) Total

Figure 64: ^{210}Po MC events efficiency ε_α and leakage L_β radial dependency year by year calculated with MLPv8 discriminator in different parts of the detector. Colors represent different years.



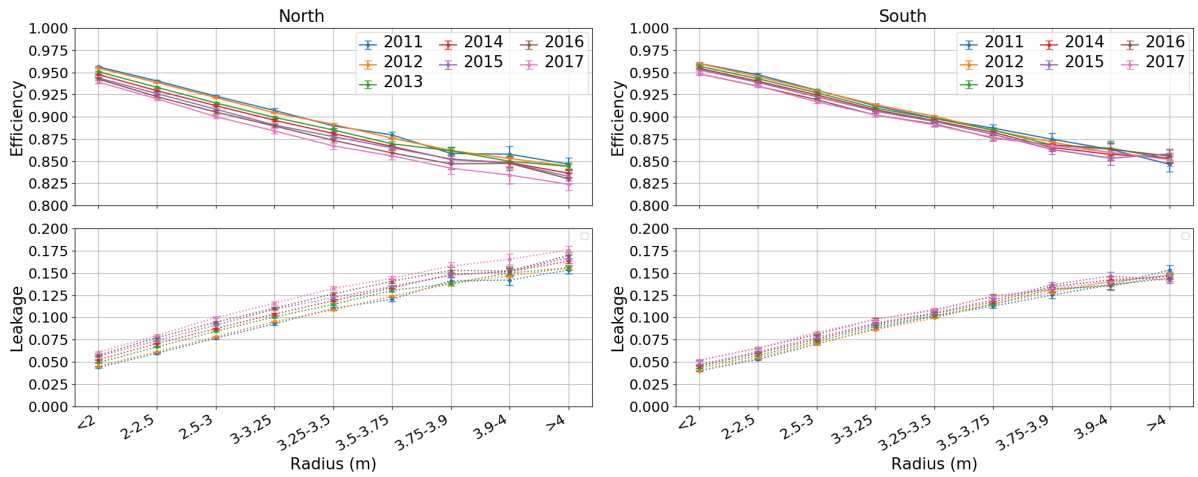
(a) North

(b) South



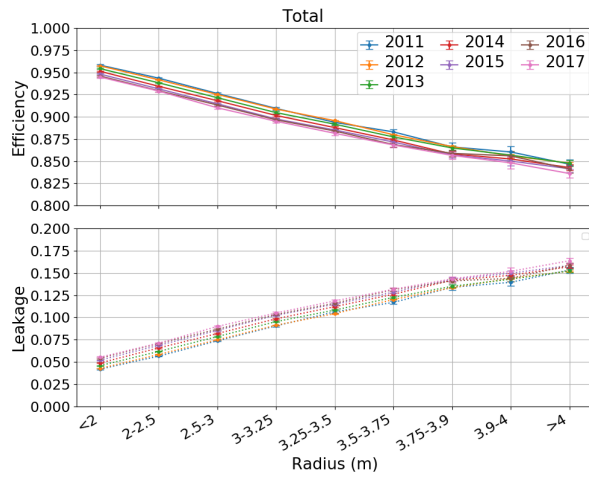
(c) Total

Figure 65: ^{210}Po MC events efficiency ε_α and leakage L_β radial dependency year by year calculated with FCN214 discriminator in different parts of the detector. Colors represent different years.



(a) North

(b) South



(c) Total

Figure 66: ^{210}Po MC events efficiency ε_α and leakage L_β radial dependency year by year calculated with FCN210 discriminator in different parts of the detector. Colors represent different years.

Appendix E

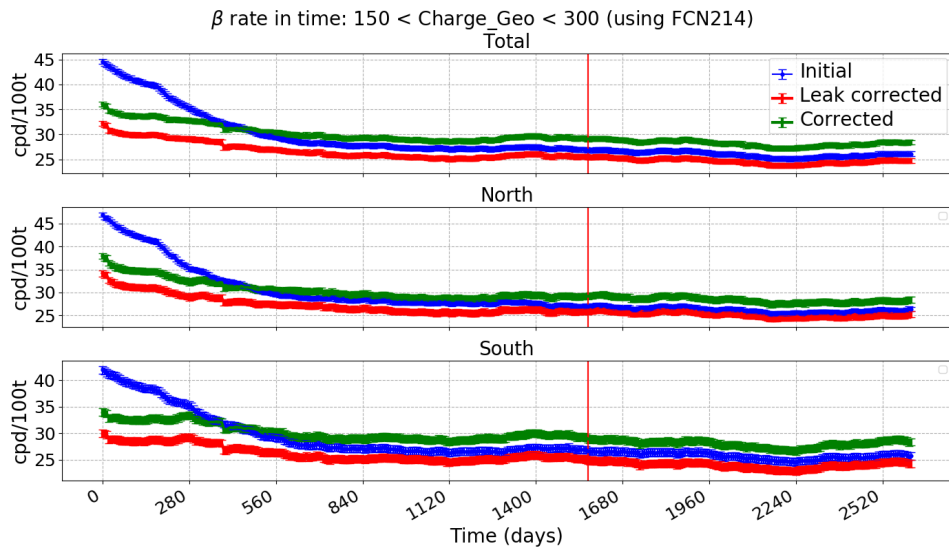


Figure 67: Efficiency ε_β and leakage L_α corrections for FCN214 discriminator. Blue line is the initial β -rate obtained with discriminator, red line represent only leakage corrections and green line is the final corrected β -rate in low energy region. The x-axis represents the time from the end of 2011 (as 0) until June 2019 (as 2520). The vertical red line is the start of so called Phase-III (May 2016).

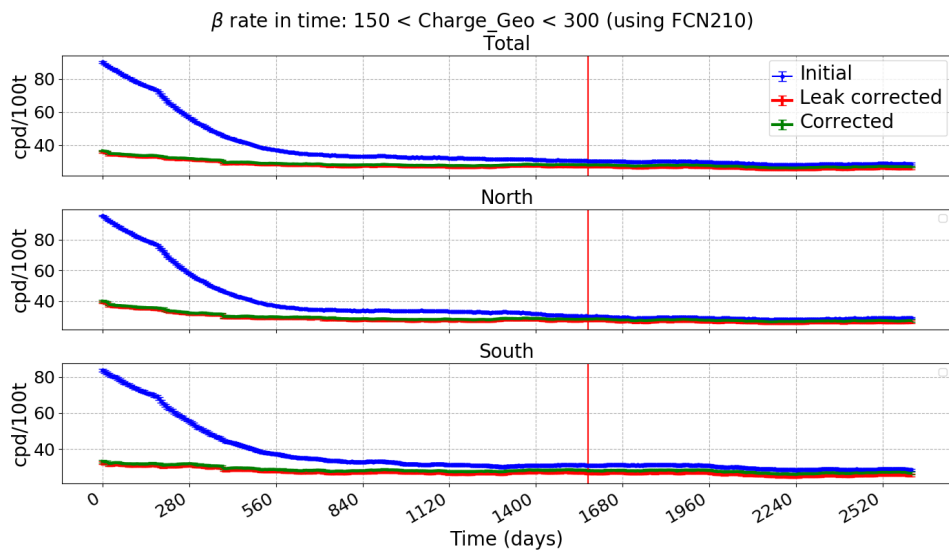


Figure 68: Efficiency ε_β and leakage L_α corrections for FCN210 discriminator. Blue line is the initial β -rate obtained with discriminator, red line represent only leakage corrections and green line is the final corrected β -rate in low energy region. The x-axis represents the time from the end of 2011 (as 0) until June 2019 (as 2520). The vertical red line is the start of so called Phase-III (May 2016).

References

- [1] <http://pdg.lbl.gov/>.
- [2] <http://borex.lngs.infn.it/>.
- [3] Carlo Giunti, Chung W. Kim. *Fundamentals of Neutrino Physics and Astrophysics*, 2007.
- [4] D.H. Perkins. *Particle Astrophysics Second Edition*, Oxford University, 2009.
- [5] Maurizio Salaris, Santi Cassisi. *Evolution of Stars and Stellar Populations*. England, 2005.
- [6] S Turck-Chièze. *The Standard Solar Model and beyond*. 2016 J. Phys.: Conf. Ser. 665 012078.
- [7] John N. Bahcall. *The luminosity constraint on solar neutrino fluxes*. arXiv:hep-ph/0108148v3, 2001.
- [8] Núria Vinyoles, Aldo M. Serenelli, Francesco L. Villante, Sarbani Basu, Johannes Bergström, M.C. Gonzalez-Garcia, Michele Maltoni, Carlos Peña-Garay, Ningqiang Song. *A new Generation of Standard Solar Models*. arXiv:1611.09867v4 [astro-ph.SR], 2017.
- [9] Borexino collaboration. *Comprehensive measurement of pp-chain solar neutrinos*. Nature, 496(2018)505, October 2018.
- [10] Pablo Mosteiro. *First measurement of pp neutrinos in real time in the Borexino detector*. Princeton University, September 2014.
- [11] David Bravo Berguno. *Precision Background Stability and Response Calibration in Borexino: Prospects for Wideband, Precision Solar ν Spectroscopy and BSM ν Oscillometry Through a Deeper Detector Understanding*. Virginia Polytechnic Institute and State University, November 2016.
- [12] Borexino collaboration. *Borexino calibrations: Hardware, Methods and Results* arXiv:1207.4816v2, November 2012.
- [13] Borexino collaboration. *The Monte Carlo simulation of the Borexino detector* arXiv:1704.02291v1, April 2017.
- [14] Borexino collaboration. *Final results of Borexino Phase-I on low-energy solar-neutrino spectroscopy*, 2014.
- [15] Simone Marcocci. *Precision measurement of solar ν fluxes with Borexino and prospects for $0\nu\beta\beta$ search with ^{136}Xe -loaded liquid scintillators.*, Gran Sasso Science Institute, Italy, 2016.
- [16] C. Arpesella et al. (Borexino Collaboration). *Direct Measurement of the ^7Be Solar Neutrino Flux with 192 Days of Borexino Data*. Phys. Rev. Lett. 101, 091302 – Published 29 August 2008.

- [17] Borexino Collaboration. *First evidence of pep solar neutrinos by direct detection in Borexino*. arXiv:1110.3230v1 [hep-ex] 14 Oct 2011.
- [18] G. Bellini et al. (Borexino Collaboration). *Measurement of the solar ^8B neutrino rate with a liquid scintillator target and 3 MeV energy threshold in the Borexino detector*. Phys. Rev. D 82, 033006 – Published 5 August 2010.
- [19] Borexino Collaboration. *Neutrinos from the primary proton–proton fusion process in the Sun*. Nature volume 512, pages 383–386 (28 August 2014).
- [20] Alessandra Carlotta Re. *The Borexino impact in the Global Analysis of Neutrino Data*. Italy, 2010-2011.
- [21] Silvia Caprioli. *Analysis of the solar neutrino spectrum with Borexino Phase-II data: towards an improved sensitivity to CNO neutrinos*. Italy, 2015.
- [22] Borexino Collaboration. *Muon and Cosmogenic Neutron Detection in Borexino*. arXiv:1101.3101, 2011
- [23] L. Wolfenstein. *Neutrino oscillations in matter*. Phys. Rev. D, 17 (1978), DOI: 10.1103/PhysRevD.17.2369.
- [24] C. Kim and A. Pevsner. *Neutrinos in Physics and Astrophysics* Contemporary Concepts in Physics 8 (1993).
- [25] F. Vissani and A. Strumia. *Neutrino masses and mixings*. arXiv:0606054v3[hep-ph], 2010.
- [26] A. Yu. Smirnov. *The MSW effect and Solar Neutrinos.*, 2003.
- [27] Borexino collaboration. *First Simultaneous Precision Spectroscopy of pp, ^7Be , and pep Solar Neutrinos with Borexino Phase-II.*
- [28] Borexino collaboration. *Improved measurement of ^8B solar neutrinos with 1.5 kt·y of Borexino exposure*. arXiv:1709.00756v1 [hep-ex], Sep 2017.